

Microphysiological Systems for Improved Modeling of Diseases Involving Tubular Organs

By
Mouhita Humayun

A dissertation submitted in partial fulfillment of
the requirements for the degree of

Doctor of Philosophy
(Biomedical Engineering)

at the
UNIVERSITY OF WISCONSIN-MADISON
2021

Date of final oral examination: 11/19/2021

The dissertation is approved by the following members of the Final Oral Committee:

David J. Beebe, Professor, Biomedical Engineering

Laura J. Knoll, Professor, Medical Microbiology & Immunology

Melissa C. Skala, Professor, Biomedical Engineering

Suzanne M. Ponik, Assistant Professor, Cell and Regenerative Biology

Andreas Friedl, Professor, Pathology and Laboratory Medicine

© Copyright by Mouhita Humayun 2021

All Rights Reserved

To mom, dad, and my sister.

Acknowledgements

My graduate experience (and my stay in Madison) have been extremely memorable and enlightening, and many people need to be thanked for their part in making this experience unforgettable. First, I would like to express my sincerest appreciation for my advisor, Dr. David Beebe. Thank you, Dave, for taking a chance on and helping me grow as a scientist and as a person. I'm incredibly grateful for all your support, for the freedom to pursue my own ideas and for the lab environment with such diverse expertise that you've cultivated. I have learned invaluable lessons from you, academic and otherwise, and I feel privileged to have been a part of your group.

Thank you to my committee, Drs. Laura Knoll, Suzanne Ponik, Melissa Skala and Andreas Friedl for your insightful suggestions on my research over the years and for your encouragement on my scientific endeavors.

I'm incredibly grateful for my mentors in the MMB lab. To Sheena Kerr, thank you for always finding time to support me academically and emotionally, and for always helping me see the positive side of failures. Chao Li, thank you so much for generously sharing your boundless knowledge on chemistry, material science and physics and the countless hours of discussions on life and science. I've learned so much about how to conduct scientific research and ask important science questions from you, I will be forever thankful for this. To Jose Ayuso, thank you for your helpful insight on experiment planning and framing science questions. Thank you also to Maria Virumbrales for discussions on navigating through graduate school and academia.

I wish to give special thanks to Pete Geiger, who is an amazing lab manager and an incredibly patient person, and an absolute joy to be around. Also, thanks to Alice Golubiewski for all the help with administrative tasks. I thank all my labmates, past and present. I would not have survived graduate school without your camaraderie and support. I especially thank Teddy de Groot and Karina M. Lugo-Cintrón for their trust and friendship, and for lending an ear during tough times. Thank you to Duane Juang and Terry Juang for being the microfabrication gurus in our lab and for wonderful discussions on science. Megan Livingston, Ravi Yada, Kehinde Adebayo Babatunde and Christina Sanchez De Diago, I thank them for their support and for being awesome. Thank you to my wonderful collaborators Tiffany Heaster and Yang Hu for being a pleasure to work with.

Finally, I thank my family and friends. Thank you to my parents, Ereen Akter and Humayun Sharif for their unwavering support and faith in me. Thank you for teaching me the values of hard work and caring for others. I'm grateful to you for believing in me and always encouraging me to persevere, rise above, and shoot for the moon. I thank my sister Pryata Humayun, who despite circumstances, always makes room and time for me in her life. And last but not least, I thank my best friends Rahanuma Wafa and Priya Patel for never failing to support me, from more than 500 miles away, even when life is busiest. Thank you for teaching me to stand-up for myself. I cannot fully express my gratitude for all you have done, and I cannot thank you enough for being in my life.

Abstract

Drug development cost over the years has increased while the number of approved drugs annually has declined, mainly due to high attrition rates in clinical trials. To lower the burden of cost of drug development, there is an urgent need for more predictive human tissue models to determine drug efficacy and safety as early as possible. Although animal models have contributed immensely, both to the development of new drugs and our understanding of physiology or disease, frequent discordances between animal and human studies have been found. Despite significant development in computational and *in vitro* biology, standard culture platforms (e.g., cell lines grown in 2D culture in a dish) offer limited control over the culture environment and often fail to recapitulate the complexity of *in vivo* biology. Biomimetic modeling of human tissues aims to bridge the gap between 2D *in vitro* culture and animal models by approximating the complex molecular, structural, and functional phenotypes of native tissues. In this context, microphysiological systems or organotypic models have attracted substantial interest in recent times owing to their potential in providing key insights into physiological and pathological processes. These innovative devices could serve as powerful platforms at multiple stages of the drug discovery and development processes to accelerate pre-clinical testing.

Tubular structures *in vivo* are ubiquitous, being present in mammary ducts, blood vessels, and the intestine among other organs. In this dissertation, a set of microphysiological systems developed to study and improve the modeling of disease processes in tubular organs, including cancer progression, metastasis, and

gastrointestinal infections, are presented. A method established to generate arrays of tubular tissues enabling robust and complex multi-tissue interactions for increased throughput studies is described. Also presented is an organotypic model used to mimic cancer-vascular interactions involved in extravasation, a process in cancer metastasis that involves cancer cells exiting the vascular system. Finally, a more complex microphysiological system developed to elucidate human immune cell response during parasitic infection of the intestinal tract is described. Together, these microphysiological systems extend our ability to study and develop new therapies that target microenvironmental factors contributing to the progression of diseases involving tubular organs.

Contents

Acknowledgements	ii
Abstract	iv
Contents	vi
List of Figures	x
List of Tables	xiii
Chapter 1	1
1.1 Cancer Metastasis	2
1.1.1 Tumor Cell Extravasation	3
1.1.2 Targeting Cancer-Stroma Interactions	5
1.1.3 Current Approaches to Study Cancer Metastasis	6
1.2 Infection	7
1.2.1 Parasitic Infections	8
1.2.2 <i>Toxoplasma gondii</i>	8
1.2.3 Acute Immunity Against Parasitic Infections	9
1.2.4 Current Approaches to Study Parasitic Infections	10
1.3 Thesis Aims	12
Chapter 2	15
Generation of tubular structures in array with a reconfigurable barrier for modeling multi-tissue interactions	15
2.1 Introduction	17
2.2 Results and Discussion	20
2.2.1 Microfluidic Platform Design and Assembly	20
2.2.2 Integration with Laboratory Automation	24
2.2.3 Liquid Barrier Enabled Compartmentalization for Parallel Tissue Formation	28
2.2.4 Liquid Barrier Enabled On-Demand Co-Culture	32
2.2.5 Liquid Barrier Reconfiguration	35
2.3 Materials and Methods	39
2.3.1 Device Fabrication	39
2.3.2 Polystyrene Device Fabrication	40

2.3.3 Stage Design and Fabrication	40
2.3.4 PDMS Device Bonding to Glass Slide	41
2.3.5 Nylon Threading	42
2.3.6 Collagen Gel Preparation	43
2.3.7 Gilson Pipetmax Robot Setup	43
2.3.8 Cell Culture	43
2.4 Acknowledgments	44
Chapter 3	45
Elucidating cancer-vascular paracrine signaling using a human organotypic breast cancer cell extravasation model	45
3.1 Introduction	47
3.2 Materials and Methods	51
3.2.1 Organotypic Vascular Device Fabrication and Assembly	51
3.2.2 ECM Gel Preparation and Loading	51
3.2.3 Cell Culture	52
3.2.4 Cell Seeding and Lumen Formation	53
3.2.5 Direct Contact and Indirect Co-Culture of BCCs	54
3.2.6 Blocking and Neutralization	54
3.2.7 Cytokine Quantification	55
3.2.8 Immunofluorescence Staining	56
3.2.9 Image Acquisition	56
3.2.10 Image Analysis (Extravasation events, ICAM-1 expression, and Col IV deposition)	57
3.2.11 Statistical Analysis	57
3.3 Results	58
3.3.1 Organotypic Breast Cancer Cell Extravasation Model	58
3.3.2 BCCs Modulate Endothelial Properties and Basement Membrane Components	60
3.3.3 Secreted Factor Analysis Reveals Distinct Profiles for Highly And Poorly Invasive BCCs	64
3.3.4 Tumor and Endothelial Derived Factors Involved In Cancer-Vascular Crosstalk	67

3.3.5 Cancer-Vascular Paracrine Signaling Leads to Impaired Vascular Barrier Function.....	69
3.3.6 Therapeutic Inhibition of IL-6, IL-8 and MMP-3 Reduces Overall Secretion of Factors Associated with Breast Cancer Metastasis	73
3.3.7 Combination of Tocilizumab, Reparixin and UK-356618 Reduces BCC-Induced Barrier Dysfunction and BCC Migration in The Extravasation Model....	76
3.4 Discussion	79
3.5 Acknowledgments.....	87
Chapter 4.....	88
Innate immune cell response to host-parasite interaction in a human intestinal tissue microphysiological system	88
4.1 Introduction	89
4.2 Results.....	93
4.2.1 Development of an Intestinal Tissue MPS for Studying Host-Pathogen Interactions.....	93
4.2.2 Generation and Characterization of Primary Small Intestinal Tubes in the Intestinal Tissue MPS.....	97
4.2.3 Modeling Protozoan Parasite Infection in Human Intestinal Epithelium...	102
4.2.4 Neutrophil Response to <i>T. gondii</i> Infection of the Intestinal Epithelium...	104
4.2.5 IFN- γ Mediated Neutrophil Response to <i>T. gondii</i> Infection.....	108
4.2.6 Innate Immune Cell Response to Parasite Invasion and Replication In The Intestinal Epithelium	113
4.3 Discussion	117
4.4 Materials and Methods.....	128
4.4.1 Intestinal Tissue MPS Fabrication and Assembly	128
4.4.2 ECM Gel Preparation and Loading	129
4.4.3 Crypt Isolation and Gut Organoid Culture	130
4.4.4 Caco-2 Epithelial Tube Formation.....	131
4.4.5 Primary Intestinal Epithelial Tube Formation	132
4.4.6 Co-Culture of Epithelial Tubes with Endothelial Tubes	133
4.4.7 Co-Culture of Epithelial and Endothelial Tubes with NK Cells	134
4.4.8 Neutrophil Isolation.....	134
4.4.9 Parasite Cell Culture and Infection.....	135

4.4.10 Immunofluorescence Staining	135
4.4.11 Image Acquisition	136
4.4.12 Optical Metabolic Imaging	136
4.4.13 Cell Retrieval from Microdevice	137
4.4.14 Reverse Transcription Quantitative Polymerase Chain Reaction	138
4.4.15 Multiplex Cytokine/Chemokine Assays and Analysis.....	139
4.4.16 Statistical Analysis.....	139
4.5 Acknowledgments.....	139
Chapter 5.....	141
Concluding Remarks and Future Directions.....	141
5.1 Multi-Organ Interactions and Dynamic Reconditioning Experiments Using Microfluidic Array Platform	142
5.2 Examine and Target Tumor-Stromal Signaling at Secondary Metastatic Sites	143
5.3 Integrating Relevant Oxygen Levels for Improved Modeling of Intestinal Tissue Microenvironment	146
Appendix	149
Appendix A: Additional Tables and Graphs from Chapter 3	149
Appendix B: Additional Tables and Graphs from Chapter 4	162
Bibliography.....	174

List of Figures

Figure 1.1 Mechanisms involved in tumor cell extravasation.....	4
Figure 1.2 The life cycle of <i>T. gondii</i>	9
Figure 1.3 Overview of thesis aims	14
Figure 2.1 Array of tubular structures: device design and assembly.	23
Figure 2.2 Device operation using liquid-handling setup.	26
Figure 2.3 Illustration of workflow to integrate automated liquid handling.	27
Figure 2.4 Characterization of fluidic interconnection within the tubular tissue structure array device.....	31
Figure 2.5 Compartmentalization and subsequent co-culture demonstration using FC oil liquid barrier.	34
Figure 2.6 Characterizing functionality of reconfigurable liquid barrier.	37
Figure 2.7 Key design features of the stage.	41
Figure 2. 8 Nylon threading configuration.	42
Figure 3.1 3D organotypic breast cancer extravasation model and setup.	58
Figure 3.2 Breast cancer cell extravasation behavior and cancer-vascular interactions.	63
Figure 3.3 Protein secretion profiles iPSC-EC vessels and breast cancer cell cultured within the proposed model.	64
Figure 3.4 Cancer-endothelial crosstalk via soluble factor signaling.	67
Figure 3.5 Impact of breast cancer cell extravasation on iPSC-EC vascular permeability.	69
Figure 3.6 Protein secretion profiles of the breast cancer extravasation model with and with treatment of independent and combined therapeutic inhibitors. ...	73
Figure 3.7 Functional responses (vessel permeability, basement membrane remodeling and extravasation events) of systems treated with therapeutic inhibitors.	76

Figure 4.1 Human intestinal tissue microphysiological system for studying innate immune responses to parasitic infection.	93
Figure 4.2 Integrating primary intestinal epithelial cells in the human intestinal tissue MPS.	97
Figure 4.3 Modeling protozoan parasite invasion and replication in the intestinal epithelium.	102
Figure 4.4 Neutrophil response to <i>T. gondii</i> infected epithelium.	104
Figure 4.5 Neutrophil effector functions and contribution to <i>T. gondii</i> dissemination beyond the intestinal epithelium.	108
Figure 4.6 Immune cell response and cytokine secretions within the intestinal tissue MPS.	116
Figure 5.1 Breast Cancer Metastasis into the Lung Microenvironment.	145
Figure 5.2 Controlling Oxygen Microenvironment of The Intestinal Tissue Model.	147
Figure A.1 3D organotypic breast cancer extravasation model design and dimensions.	149
Figure A.2 ICAM-1 expression analysis of iPSC-EC vessels in monoculture and in co-culture with MDA-MB-231 cells.	150
Figure A.3 Intensity profile analysis of COL IV distribution across iPSC-EC lumens under monoculture and direct-contact co-culture with MDA-MB-231 cells.	151
Figure A.4 Membrane transference between iPSC-EC vessel and MDA-MB-231 cells.	153
Figure A. 5 Differential ICAM-1 expression on iPSC-EC vessels in monoculture and in co-culture with MDA-MB-231 cells.	154
Figure A.6 Differential COL IV deposition by iPSC-EC vessels in monoculture and in co-culture with MDA-MB-231 cells.	155
Figure A.7 Impact of MCF-7 culture on iPSC-EC vascular permeability.	156

Figure A.8 Permeability of iPSC-EC vessel compared to a control lumen with no endothelial cells.....	157
Figure A.9 Viability assessment of iPSC-ECs incubated with different concentrations of inhibitors in a well plate for 48 h.	158
Figure A.10 Effect of MMP inhibition (UK-356618, an MMP-3 inhibitor) on COL IV expression on iPSC-EC vessels within the BCC extravasation model.	159
Figure A.11 Effect of MMP inhibition (UK-356618, an MMP-3 inhibitor) on ICAM-1 expression in iPSC-EC vessels within the BCC extravasation model.....	160
Figure B.1 Upregulated genes in primary intestinal epithelium cultured and differentiated in the human intestinal tissue MPS relative to standard culture methods.....	162
Figure B.2 Downregulated genes in primary intestinal epithelium cultured and differentiated in the human intestinal tissue MPS relative to standard culture methods.....	163
Figure B.3 Dynamic analysis of neutrophils extravasation and trafficking towards <i>T.gondii</i> infected epithelium.....	164
Figure B.4 Influence of IFN- γ stimulation and inhibition on neutrophil function at the site of <i>T. gondii</i> infected epithelium.....	165
Figure B.5 Optical redox ratio assessment in IFN- γ primed neutrophils during <i>T. gondii</i> infection.	166
Figure B.6 Effects of epithelial infection by <i>T. gondii</i> on immune cell adhesion to endothelium.....	167

List of Tables

Table A.1 Primary and secondary antibodies used for immunofluorescent staining	161
Table B.1 Top 10 most relevant GO terms (Biological Processes) associated with genes analyzed in neutrophils with their corresponding FDR-adjusted P value	169
Table B.2 Primary and secondary antibodies used for immunofluorescent staining	170
Table B.3 Primer set sources for gene expression analysis of primary intestinal epithelium culture in intestinal tissue MPS and in transwells	171
Table B.4 Primer sequences for neutrophil gene expression analysis	172

Chapter 1

Animal models are gold standard to date for preclinical evaluation of drug efficacy and toxicity in pharmaceutical development, however, high failure rates (around 40%)¹ remain in human clinical trials. In addition, low-throughput *in vivo* animal studies are often a large contributor of lengthy and costly drug development life cycles. On the other hand, *in vitro* cell culture in Petri dishes is a simple and high-throughput method for basic drug screening and testing, however, these cellular models generally lack tissue microarchitecture and physiological functionality seen *in vivo*. To address these shortcomings, alternative tissue models that mimic human physiology and disease are urgently required to accelerate development of new therapies. Microphysiological systems (MPSs) and Organ-on-chips (OoCs) have emerged as promising technologies that have the potential to foster a paradigm shift in drug development and personalized medicine by replacing animal models.

A major reason for the high failure rates of new drugs in clinical trials can be attributed to our insufficient understanding of fundamental human diseases and the underlying mechanisms. Cell-based microfluidic systems leverage simple physical principles to allow studies of cell-cell communication and improved modeling of diseased states such as cancer and infection. Over the last decade, MPSs or OoCs developed using microfluidic-based approaches have advanced significantly. With the help of microfluidic-based tools and microfabrication technologies, such as soft lithography,

these technologies can provide better control over microenvironmental parameters such as increased sensitivity to signaling events². Moreover, MPSs aim to incorporate human relevant cell sources and recapitulate key characteristics of the diseased microenvironment including three dimensional (3D) cellular architecture and functionality, 3D extracellular matrix (ECM), biochemical factors (e.g., soluble factor signaling, pH and metabolites), and biophysical cues (e.g., shear stresses and oxygen levels)^{2,3}. In contrast to tissue engineering, MPSs do not strive to reproduce whole organs or tissues at scale for clinical replacement but rather are designed from a viewpoint of reductionism. Overall, these technologies emulate *in vivo* physiological environments to reproduce key functional properties of small tissue or organ constructs at the microscale, for deciphering pathological mechanisms contributing to disease progression, and for integration into drug development pipelines.

In the following subsections, I highlight our current understanding of how cancer and infectious disease progress and how microenvironmental factors shape cellular response to better understand how we can improve modelling of diseases using MPSs. Reviews of how specific MPSs have helped overcome limitations of current macroscale methods are outlined in the respective chapters where cancer (Chapter 2 and 3) and infection (Chapter 4) models are discussed.

1.1 Cancer Metastasis

Metastasis is the spread of cancer cells from a primary tumor to distant organs via blood vessels or lymph nodes and is often considered a terminal event in malignant tumor

progression. A significant fraction of breast cancer patients develop metastasis sooner or later, and this relapse is associated with high mortality rates⁴. For patients diagnosed with metastasized breast cancer, the 5-year survival rate currently rests at only 6%, reflecting the need for improved therapies and additional insight into the metastatic process⁴. It is well understood that the interactions between tumor cells and microenvironmental components are central to the regulation of cancer progression. Recognizing the importance of the tumor microenvironment (TME) in cancer progression has shifted the tumor-centered view of cancer development to a dynamic milieu in which cellular and molecular components are as influential as cancer cells themselves for cancer evolution and metastatic dissemination⁵.

Preferences of certain tumors to metastasize to specific organs have been recognized for well over a century. Extensive body of clinical data and experimental research has confirmed Steven Paget's hypothesis that the ability of tumor cells to initiate growth largely depends on crosstalk between metastatic tumor cells ("seed") and host microenvironment ("soil")⁶. Despite acceptance of this hypothesis, a critical barrier to research progress can be attributed to the lack of relevant experimental approaches that combine the complexity of the tumor microenvironment with the ability to isolate specific roles of each microenvironmental factor.

1.1.1 Tumor Cell Extravasation

Metastasis is a highly inefficient process in that less than 0.01% of circulating tumor cells eventually succeed in forming secondary tumor growths⁷. Prior to colonization at a

distant organ, tumor cells must migrate across blood or lymph vessels through a process called extravasation. Extravasation of tumor cells are rare and transient in nature making it difficult to study how cancer cells adhere to and breach the endothelium. It has been hypothesized that adherent tumor cells may migrate across intercellular junctions between adjacent endothelial cells (paracellular route) or they may penetrate through the body of a single endothelial cell (transcellular route), however, the former has been identified as the most frequent route⁸. In addition, tumor cells may secrete factors that induce vascular remodeling which then facilitated transendothelial migration (TEM), or they may continue to divide within the vessel until extravasation occurs when the vessel ruptures by the expanding mass⁹, **Figure 1.1**. While several molecules have been implicated in the TEM process, our understanding of the precise mechanisms determining the adhesion, migration and invasive behavior of tumor cells during the extravasation process are not well understood. Furthermore, the endothelium is a key mediator of the extravasation process, and the role it plays in facilitating this process needs to be further explored to identify potential therapeutic targets⁸.

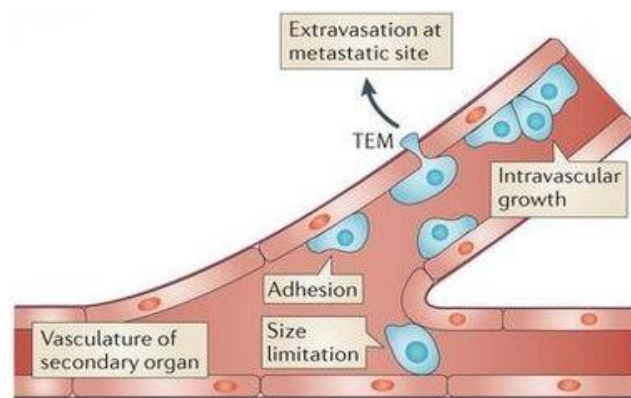


Figure 1.1 Mechanisms involved in tumor cell extravasation. Circulating tumor cells arrest on the blood vessel endothelium of secondary organ by adhesion or due to size limitation, and extravasate through transendothelial migration or undergo intravascular growth. Adapted from¹⁰.

1.1.2 Targeting Cancer-Stroma Interactions

Despite remarkable progress made in identifying prognostic biomarkers and understanding the cellular and molecular basis of tumor development, the regulatory mechanisms involved in the later stages of metastatic development, like during extravasation and colonization, remain largely unknown¹¹. While mechanical factors may influence the delivery of cancer cells to distant sites, molecular interactions between cancer cells and the host microenvironment are thought to influence the probability of invasion and growth at the secondary site⁸. Thus, most studies focus on bi-directional interactions between malignant and non-malignant cells, and the complimentary extrinsic cues from the ECM that lead to the spread of cancer¹². Seeing as molecular signaling in cancer is highly intertwined with components in the microenvironment, treatment options of metastatic cancer need to shift towards targeting multiple mechanisms and interactions to enhance treatment efficacy. Moreover, the response of targeting multiple mechanisms will need to be considered in the context of the complex biological interactions between cancer and the host microenvironment.

As cancer progresses, mutations favorable to tumor survival are selected¹³. As such, inhibiting a pathway by a single drug may be insufficient for controlling tumor progression. Combination therapy allows integration of multiple therapeutics to enhance efficacy by targeting multiple pathways including tumor-intrinsic and stroma-induced properties¹⁴. In addition, it enables reduced dosing and thus, decreased cytotoxic effects on non-cancerous cells, and it potentially reduces drug resistance as it may be

more challenging for cancer cells to develop resistance towards multiple pathways at once¹⁴. Given that metastatic spread and colonization is highly dependent on the complex interactions between tumor cells and stromal components, development of combination therapy will require models that can reliably recapitulate the complexity of the metastatic microenvironment in a cost-effective manner.

1.1.3 Current Approaches to Study Cancer Metastasis

Studying cancer invasion of the target metastasis is one of the most technically challenging aspects of cancer biology¹¹. Part of this challenge lies in the availability of models that can easily and cost effectively characterize specific host-cancer interactions while incorporating enough components to recapitulate key signaling events that occur *in vivo*. To address this need, new platforms and technologies are continually being developed¹⁵.

Currently, cancer metastasis studies are primarily done in mice¹¹. Although *in vivo* models play an essential role in replicating relevant physiological conditions, it is difficult to quantify highly specific interactions between human cancer cells, blood vessels and surrounding tissue. Moreover, it can also be challenging to perform parametric studies that require larger- scale experiments. *In vitro* approaches on the other hand, have been utilized for analyzing cell migration mechanisms and metastatic potential of cancer cells, but they often lack the three-dimensional complexity, spatial organization and relevant cell-cell and cell-stroma interactions for modelling *in vivo* response¹⁶. The increasing appreciation for disease complexity and the need to maximize throughput while

reducing time, cost and reagent consumption required for readouts has made organotypic models a viable option¹⁵. Recent advances in organotypic approaches combined with microscale cell-based technologies have enabled us to bridge this gap between *in vivo* and *in vitro* systems by recapitulating physiologically relevant biological responses and by integrating important structure / function relationships and complex 3D microenvironmental interactions (i.e., cell-cell, cell-matrix and soluble factor signaling)¹⁵. Various microfluidic-based models have been developed to study metastasis organ specificity^{17–19}. However, these models remain underutilized and there remains a need for more accessible models that can be used to investigate the role of stromal components and the vasculature in metastatic spread of cancer cells.

1.2 Infection

Infections by microorganisms or parasites require a mode of transmission, portal of entry, and a susceptible host. The course of infection involves many steps which can vary widely for different pathogens. *In vivo* animal models have long been used to study this chain of events as they provide a complex environment that includes many features important for studying pathogenesis of infections. Importantly, in some cases animals (e.g., feline for *T. gondii*) serve as a host for human pathogens during part of their lifecycle and, in such cases, animals are an appropriate model²⁰. However, as a model for human infection, the differences between animal and human immune responses is a major obstacle to understanding the pathogen-immune interactions which are critical to the progression of human infection²¹. In addition, for many pathogens, little is known

about the mechanisms that regulate pathogen entry and dissemination (i.e., trafficking) in the human host.

1.2.1 Parasitic Infections

The gastrointestinal tract is exposed to a huge variety of bacteria, viruses, protozoa parasites as well as other eukaryotic pathogens, and these exposures cause more than 2000 children to die of diarrheal diseases every day around the world²². Protozoan parasites are major causes of morbidity and mortality globally and are frequently transmitted to humans via contaminated food. While many protozoal pathogens are poorly characterized even the best-studied undergo developmental transitions in the gastrointestinal tract that cannot currently be replicated in the lab.

1.2.2 *Toxoplasma gondii*

The life cycle of *T. gondii*, a protozoan parasite, is complex and includes both sexual and asexual forms²³. The asexual life cycle of *T. gondii* occurs within any warm-blooded animal and has two developmental stages: a rapidly replicating form called a tachyzoite and a slow growing form called a bradyzoite, which causes chronic life-long infection²³. The asexual cycle begins when either tissue cyst containing bradyzoites or oocysts are ingested, and their environmentally resistant walls are digested by the pepsin and acid in the stomach. Released bradyzoites or oocyst forms (called sporozoites) then invade the intestinal epithelium and differentiate into tachyzoites that disseminate throughout the body in immune cells²⁴. Immune stress causes tachyzoites to differentiate into bradyzoites, which are virtually hidden from the immune response and establish a

chronic life-long infection, **Figure 1.2A**. *T. gondii* bradyzoites may either differentiate into a pre-sexual stage or a tachyzoite. The sexual cycle of *T. gondii* is restricted to the feline intestine, where ingested bradyzoites invade the feline intestinal epithelium and differentiate into several pre-sexual and sexual forms. The product is an oocyst that is shed in the feces and in the environment further develops to contain infectious sporozoites^{23,24}.

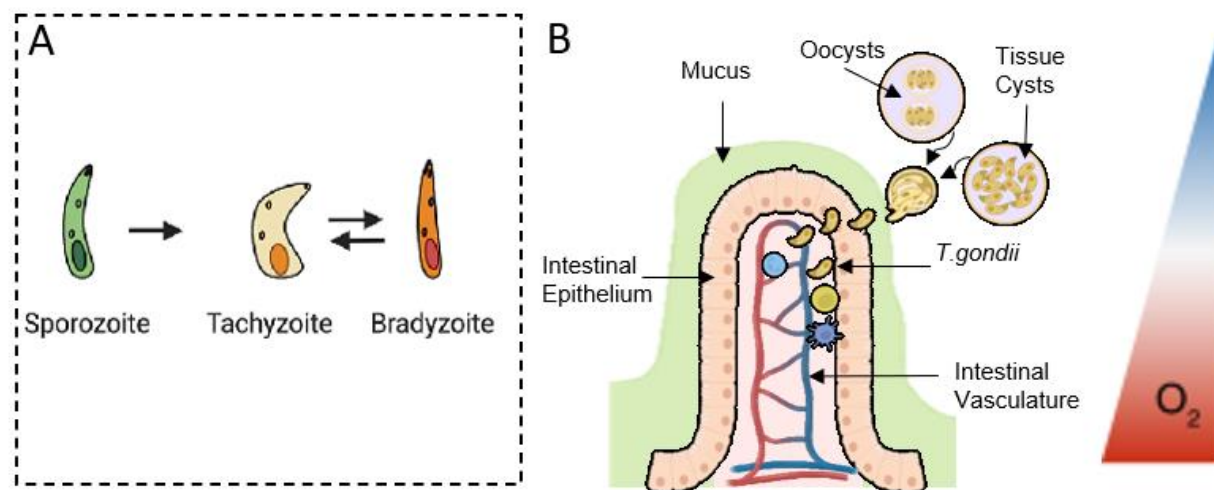


Figure 1.2 The life cycle of *T. gondii*. (A) After host cell invasion, *T. gondii* bradyzoites or Sporozoites differentiate into tachyzoite. Immune stress causes tachyzoites to differentiate into bradyzoites during chronic long-term infection. Adapted from²⁵. (B) Schematic depicting infection of the intestinal tissue by oocyst or tissue-cyst containing *T. gondii*.

1.2.3 Acute Immunity Against Parasitic Infections

The intestinal mucosa is a major first line of defense against infectious pathogens and an important niche for commensal microbiota. The intestinal epithelial cell layer separates the luminal components from the underlying tissue while the mucosal immune cells and the intestinal vasculature regulates entry from the gut parenchyma into circulation, **Figure 1B**. In response to parasite invasion, intestinal epithelial cells and tissue-resident leukocytes secrete a host of effector-enhancing cytokines and

inflammatory mediators, which in turn increase vascular permeability and facilitate immunological alterations of the endothelium²⁶. During these alterations, endothelial cells continually adjust their structure and function to coordinate immune cell adherence and extravasation. Once within the tissue, innate immune cells encounter effector signals that further amplify inflammatory response and control or neutralize invading pathogens, **Figure 1B**. Another key factor of the infection microenvironment is the increase in cellular oxygen demands leading to hypoxic stress, which affects immune cell function, host-pathogen interaction, and virulence of pathogens.

1.2.4 Current Approaches to Study Parasitic Infections

The limited ability to image pathogen trafficking and the time/expense of mechanistic study (i.e., genetic modifications) makes the study of pathogen trafficking challenging in animal models. *In vitro* models have also been used to study infectious diseases²⁷. While simple two-dimensional (2D) culture models (e.g., dynamics of viral infection) and transwells (e.g., disruption of barrier function) have provided some insights, more recently organoid- and microfluidic-based organ-on-a-chip or organotypic models are being applied to the study of infectious disease. These 3D models can better mimic human biology²⁷ and represent the way forward for *in vitro* infectious disease modeling. Current approaches to modeling infection in 3D fall into three general categories: transwells, organoids²⁸ and organ-on-a-chip models²⁹. Transwells are perhaps the most widely used “3D” model (perhaps more accurately described as “pseudo-3D”). In their simplest form, transwells coated with epithelial or endothelial cells have been used to study pathogen “entry” across both epithelial and endothelial barriers. However,

transwells lack important *in vivo* cues such as relevant 3D structures (i.e. curvature of blood vessels or various tracts and associated biological function)^{30–33}, shear stress^{34–39}, and the biochemical gradients⁴⁰ found in the tissue microenvironment that are known to influence both host cell function and pathogen virulence, survival and dissemination.

To better mimic the cellular microenvironment seen *in vivo*, patient or induced pluripotent stem cell (iPSC)-derived organoids have been used to create a more physiologically relevant architecture and environment in order to study the breach of the epithelial barrier by pathogens⁴¹. iPSC-derived organoids, specifically, are able to generate mesenchymal cells in addition to epithelial cells, enabling some multicellular crosstalk. However, the relative inaccessibility of the apical surfaces makes inoculation of pathogens into the cavity hard to perform. Also, the ability to perform live imaging of host-pathogen interactions can provide crucial information for pathogen entry and dissemination studies but the variable 3D geometry of organoids makes real-time imaging technically challenging⁴¹. Microfluidic-based organs-on-a-chip models overcome some of these limitations and have been developed for the lung^{42,43}, brain⁴⁴, intestine^{29,45,46}, and liver⁴⁷ to study host interactions with virus, fungus, bacteria and parasites. While some multicellular crosstalk is included in some of these models, such as the gut-on-a-chip^{48,49} and lung-on-a-chip models^{50,51} they often do not recapitulate the tissue architecture (i.e., blood vessel, epithelial lumen geometry) that can be critical for accurately mimicking host and pathogen responses.

To capture the complex interplay between the relevant cells in the infection microenvironment, the *in vitro* models that incorporate 3D tissue architecture,

differentiated epithelium, endothelium, and immune cells, and an appropriate oxygen environment to allow the inclusion of human-associated intestinal bacteria including diverse obligate and facultative anaerobes are needed.

1.3 Thesis Aims

As described above, understanding disease processes involved in cancer and infection requires techniques that can integrate high level of complexity, incorporating salient features such as tissue architectures, multi-cellular interactions and relevant cell-ECM interactions that would be present in tumor and infection microenvironment, but that are also simple enough to allow for dissection of the mechanisms involved. Taking advantage of microfluidic techniques and microengineering technologies, I present the following collection of work aimed at developing MPSs that improve our ability to investigate the role microenvironmental factors play in progressing diseases associated with tubular organs.

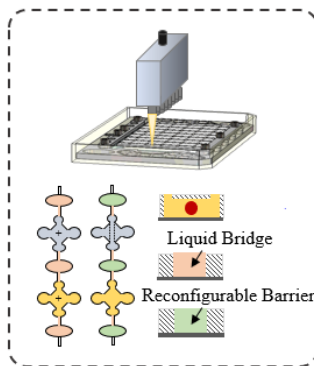
1. First, I describe a methodology developed to increase throughput of studies involving tubular organs and improve modeling of multi-tissue interactions. A novel method is presented in Chapter 2 to generate arrays of tubular structures within a 3D matrix in a single process, **Figure 1.3 (Part 1)**. The platform also uses a reconfigurable barrier that enables more complex multi-tissue interactions to be studied in a robust manner.

2. Next, I use an organotypic model to elucidate cancer-vascular signaling involved in breast cancer cell extravasation. An organotypic model of breast cancer cell extravasation is developed and characterized in Chapter 3, **Figure 1.3 (Part 2)**. The model features tubular endothelial vessels made from iPSC derived endothelial cells and breast cancer cells with varying invasive/metastatic potential. The study identifies multiple molecular targets and examines their influence on the functional behavior of cancer cells and the endothelium during extravasation using therapeutic drugs.

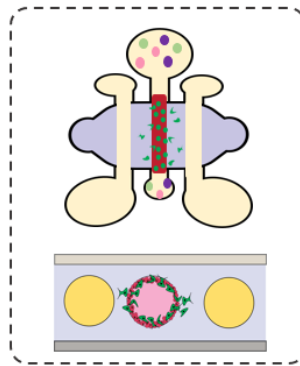
3. Finally, I present an MPS of the human intestinal tissue I developed to study host-parasite interactions and innate immune cell response to parasite infections. A human microengineered model of the gut-epithelium and vascular barrier is described and characterized in Chapter 4 that provides means for studying gastrointestinal parasitic infections and the associated interactions with innate immune cells, **Figure 1.3 (Part 3)**. The study examines questions related to human-relevant tissue response, activation of innate immunity, and the role of immune cells in parasite dissemination.

Although the platforms developed here are designed to target different biological questions, the primary goal here is to provide accessible tools to better explore and measure the complex parameter space in human diseases, towards improving predictive power of these tools and potential for their utility in drug development.

Part 1: Tubular tissue array with reconfigurable barriers



Part 2: Cancer-vascular signaling in breast cancer cell extravasation



Part 3: Innate immune cell response to parasitic infection in the intestine

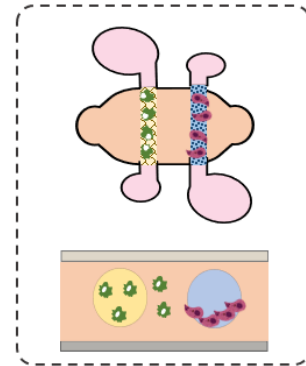


Figure 1.3 Overview of thesis aims

Chapter 2

Generation of tubular structures in array with a reconfigurable barrier for modeling multi-tissue interactions

Lumens are ubiquitous in biology *where* tubular geometries form critical defining features of normal and diseased organs. Tubular structures are also a critical component in modeling numerous physiological processes including morphogenesis, organogenesis and drug delivery. However, tube formation *in vitro* has not found widespread use in research labs or in high-throughput screening applications in large part due to the relatively cumbersome processes involved in generating tubular structures. To recapitulate physiologically relevant structure-function relationships for improved modeling of physiological and pathological processes, there is a practical need for tools to allow generation of tubular structures that can easily be integrated into existing approaches. Here, we present a platform that extends a micromolding-based technique for three-dimensional tube formation within an extracellular matrix to facilitate rapid generation of tubular structures in array and uses a reconfigurable barrier for improved modeling of multi-tissue interactions. The platform improves upon prototyping time, fabrication complexity, and robustness of existing tube-formation methods, and features high flexibility in arrangement and interconnections of multi-tissue interactions. Multiple tubular structures and tissue configuration of different cell types are formed and discretely compartmentalized by using an immiscible liquid barrier to conduct parallel

experiments on the same chip. The liquid-barrier can then be reconfigured to study multi-tissue interactions in physiological order. The possibility to perform microtissue cultures involving complex tissue geometries in parallel on the same device that can subsequently be used for more complex multi-tissue experiments renders this platform a promising technology for applications in multi-organ modeling-related research.

This chapter has been adapted from a manuscript in preparation titled "Generation of tubular structures in array with a reconfigurable barrier for modeling multi-tissue interactions" The manuscript includes authors Mouhita Humayun, José A. Jiménez-Torres, Chao Li, Jose Ayuso, Hunter O. Hefti, Karina Lugo Cintron, Joseph Ulbrich, Benjamin Meyer, and Dave J. Beebe

2.1 Introduction

One major advantage of *in vitro* cell-based models as test systems is that they allow us to acquire large data sets upon exposure to a broad variety of controlled stimuli and environmental changes. In recent years, microscale technologies have become a potential alternative for high-throughput experimentation⁵²⁻⁵⁵. Arrays such as multiwell plates and microdevices have been designed to address extensive screening protocols. Multiwell plate systems are very useful as they provide an open-well system that can be adapted to manual use on the bench as well as on automated laboratory technologies. The versatility of multiwell plates makes them a very attractive system to perform high-throughput experimentation including dose response, viability and cell culture microenvironmental factor screening. However, multiwell plate systems are limited to experiments where cells are cultured in 2D and 3D in ECM matrices⁵⁶. Even though it is possible to precisely control the culture conditions in such systems, these systems often lack relevant tissue architectures which can result in the loss of functional characteristics.

Understanding the molecular and functional basis of living systems rely on the availability of carefully engineered *in vitro* model systems. Technical advancements in microscale methods introduced microfabricated devices that allow precise manipulation of cells and liquid volumes at micro and nano scale, enabling us to generate highly controlled tissue microenvironments⁵⁷⁻⁵⁹. This led to the rise in bioengineered tissue models, which hold great potential for offsetting the need for *in vivo* models for drug development, efficacy, and toxicity assays⁶⁰. Major attributes of these systems include

multi-tissue culture, tissue structure mimicry, biochemical gradient formation, and controlled fluid transport³. Incorporating bioengineered tissue models into high-throughput workflow has been challenging due to the inherent complexity in the design and operation of these systems. Often, incorporating additional attributes such as complex tissue architectures can prevent integration of such systems to automation, leading to low throughput assays. Thus, there is a need to improve on existing technologies to provide simpler systems that are compatible with high-throughput technologies and capable of providing physiological relevant tissue characteristics including tissue architectures, cellular and ECM components.

Tubular structures exist in many organs in the body and are involved in many important physiological and disease processes. Microfluidic-based biomimetic models that incorporate relevant tissue structure, also referred to as organotypic models, have been developed to model tubular tissue constructs in the breast, gut, lung, liver and vascular systems, and diseases that affect these organs including cancer, inflammation, and infections^{49–51,61–64}. Such models include the vascular system (blood vessels to study angiogenesis to tumor cell intravasation and extravasation to modeling lymphatic vessels), mammary duct, prostate ducts, lung epithelial tubes and intestinal epithelial tubes surrounded by an ECM. One of early methods to pattern tubular structures within ECM involved the viscous patterning method, which used fluid flow (e.g., less viscous fluid flows through a more viscous fluid) to create circular hollow ECM structure⁶⁵. Due to the simplicity of using fluid flow to create tubular structures, this system was rapidly adapted to a liquid handler to achieve high-throughput lumen fabrication. Although

viscous patterning has simplified the process of creating tubular structures, the shapes and dimensions created by viscous patterning can be inconsistent. Other micromolding-based methods allow patterning of tubular structures in ECM gels using a cylindrical mold, where the material, size, structure, distance, and configuration can be controlled⁶⁶. By using micromolding-based methods, we can make organotypic models consisting of tubular structures in a variety of ECM gels in a robust and reproducible manner, making it amenable to high-throughput techniques.

As the human body consists of highly interconnected systems, fluidic interconnection between organotypic models, potentially derived from different cell types, are required for more complex multi-tissue studies. Combining multiple 3D culture systems may present challenges as the temporal and spatial gradients of communication interacting tissues vary depending on context. Thus, robust approaches that allow spatial and temporal control over multi-tissue interactions would be required. For all approaches, reproducibility is crucial to yield comparable results. Other attributes including simple tissue production, easy loading of samples as well as simple operation of the device for tissue maintenance are essential for obtaining a user-friendly system and to enable highly parallel studies. Compatibility with microscopy based-methods is also required for continuous monitoring and end-point analysis.

Towards addressing these needs, we describe a highly versatile high content assay platform for forming arrays of tubular tissue structures within compartmentalized 3D hydrogels and conducting experiments with them. Our approach advances a previously

established micromolding -based method for 3D tube formation within an ECM towards interconnected and robust multi-tissue interaction studies. The concept of interconnecting tubular tissue structures in an array format and the ability to reconfigure these connections offer the following unique features: (i) easy integration into existing laboratory automation, (ii) formation of tubular tissue structures from different cell types in parallel on the same platform, (iii) compartmentalization for individualized culture experimentation, (iv) generation of continuous gradient between interacting tissue compartments, (v) parallel culture and subsequent functional liquid interconnection through the use of liquid barriers and liquid bridges, and (vi) reconfigurability of fluidic communication between tissue compartments to enable complex multi-tissue or multi-organ experimentation.

2.2 Results and Discussion

2.2.1 Microfluidic Platform Design and Assembly

We present a design concept of an assembled unit that enables us to generate multiple tubular structures (~40-80), each within individually addressable ECM gel compartments, in a single continuous process. The design consists of a microfluidic device made from a polydimethylsiloxane (PDMS) or polystyrene (PS) substrate with a series of chambers, connected by channels, which are used to compartmentalize individual tissue units containing tubular structures, **Figure 2.1A**. We integrate design features from a previously established technique for patterning lumen structures within ECM hydrogels^{66,67}, and extend them to allow *in vitro* modeling of tubular structures in a high-throughput manner. The device contains an array of large gel chambers, that are

used to compartmentalize scaffolding matrices including synthetic (e.g., polyethylene glycol-based gels) or natural (e.g., collagen type I) ECM gels, and auxiliary chamber used to contain liquid barriers (fluorinated oil) or bridges (culture medium) to compartmentalized or connect gel chambers in series. Chambers and ports are linked by constriction channels that guide a Nylon string (cylinder rod, $\sim 230 \mu\text{m}$ in diameter) used to mold hollow tubular structures within the scaffolding gel following polymerization, **Figure 2.1B**. Nylon string acts as a flexible mold with sufficient tensile strength to withstand the pulling force required to remove the mold from the assembled unit. Once the device is assembled, scaffolding matrices can be loaded onto the device through the individually accessible gel compartments and polymerized, **Figure 2.1C**. As the choice of material for microfluidic devices in cell biology research varies based on application⁶⁸, we have chosen to apply our design concept in a range of materials. PDMS and PS are two widely used materials, each having unique strengths and limitations in microfluidics for cell-based studies. As such, we have demonstrated fabrication of the device on both PDMS or PS using soft lithography or micromachining, respectively, to accommodate various applications and user preferences.

The fully integrated unit includes three major components: bonded PDMS or PS device, a Nylon string, and the stage. The stage and its accompanying components were designed for rapid assembly, and to fit into a standard polystyrene Omni-tray. The devices were bonded to secondary substrates which are optically clear, making the device compatible with visual, absorbance, fluorescence, luminescence, and microscopy-based readouts. PDMS devices were permanently bonded to cover glasses

(190 μm thickness) via oxygen plasma activation, and PS devices were bonded to PS-thin films (~ 190 μm thickness) using solvent-assisted thermal bonding⁶⁹. To generate lumen structures, a Nylon string is threaded through the interconnecting constriction channels of the device and wrapped around the string stabilizer, which are then secured onto the stage with string immobilizers, **Figure 2.1D**. The stage is composed of an aluminum block, which was micromachined to pattern features that allow integration of the bonded device and easy handling during cell culture experiments (**See Stage Design and Fabrication in Methods and Materials**). Through-cut features on the top-left corner and bottom-right act as handles allowing users to easily move the assembled unit. An assortment of wells (top-right and bottom-left) are also patterned onto the stage to contain water for humidification during cell culture experiments. Posts along the top and bottom of the stage are used to anchor and guide the Nylon string along the stage. The bonded device with the Nylon string is secured onto the stage using immobilizers and the string stabilizer which screw onto the stage. To generate tubular structures, the Nylon string is cut along the designated Nylon string cut extrusion, located just above the upper immobilizer, and pulled out of the devices along with the string stabilizer. This allows us to generate multiple hollow lumen structures within a matrix gel that can be lined with cells for modeling relevant 3D tissue architectures of tubular organs in a high-throughput manner.

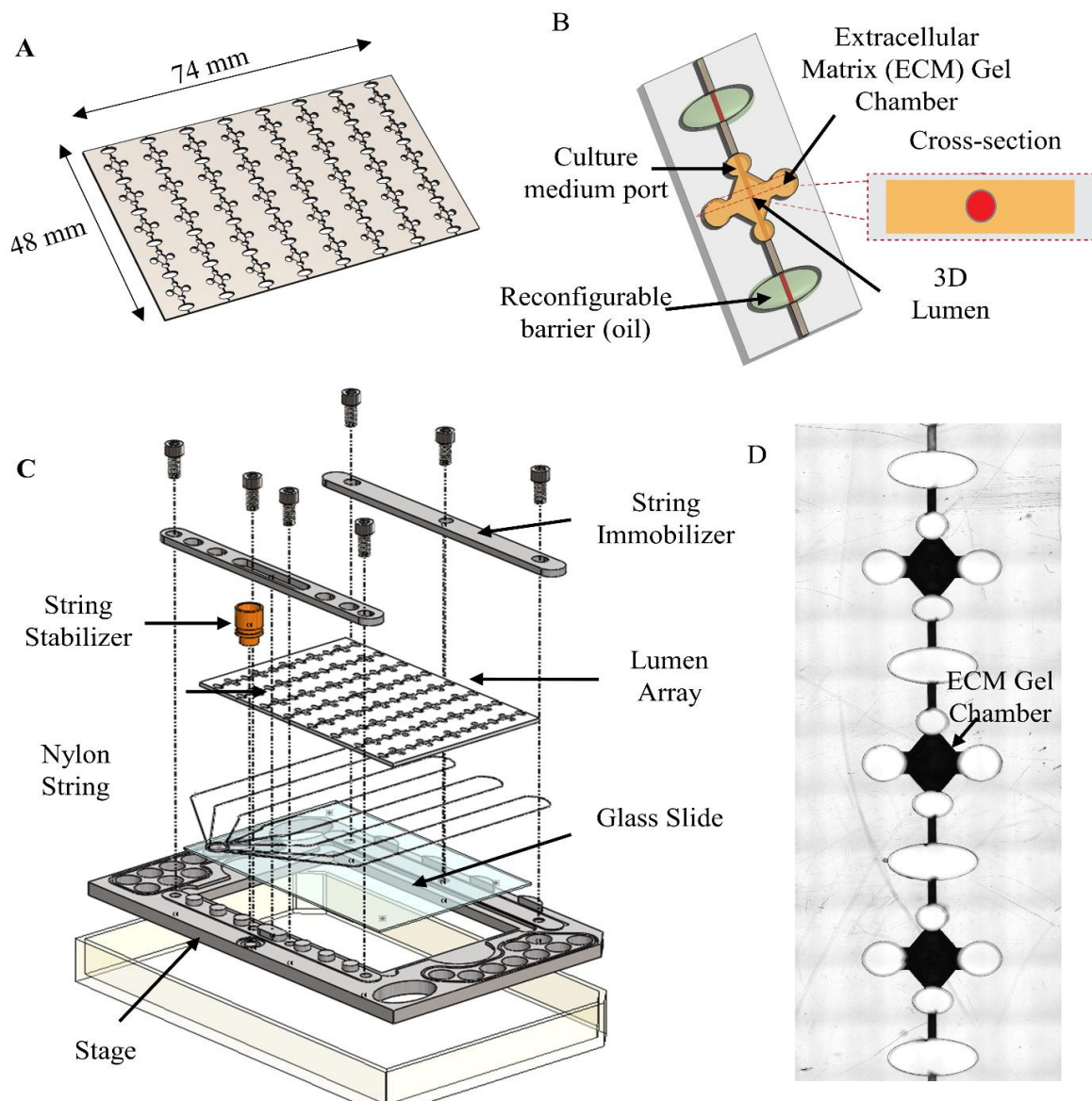


Figure 2.1 Array of tubular structures: device design and assembly. (A) Schematic representation of a microfluidic device consisting of multiple arrays of chambers used to generate tubular structures within an ECM gel. (B) Each system consists of an ECM gel chamber with gel loading ports and inlet/outlet ports for cell seeding into the 3D tubular structure. Chambers are connected to larger ports through channels, that can be used of excess media for cell culture or immiscible liquid barrier for compartmentalization. (C) Schematic showing unit assembly where the polystyrene/PDMS device is bonded to a standard glass slide. The tubular structures are generated by threading a Nylon string between the device and the glass slide around a stabilizer. The device with the string is secured to the aluminum stage and stabilized with immobilizers. An ECM gel is loaded into the gel chamber and after polymerization the Nylon string is released from the string stabilizer and removed from the device using one motion. String removal leaves behind hollow tubular structures with the ECM gel, instantly generating arrays of tubular structures. The assembled device can be contained within Omni Trays during culture experiments. (D) Brightfield image showing three systems in array highlighting the ECM gel chamber.

2.2.2 Integration with Laboratory Automation

As complexity of *in vitro* models increase, tedious and time-consuming protocols can contribute to poorly reproducible results. Automated technologies can alleviate some of these challenges by precisely reproducing machine-readable protocols. We have designed our microdevice to be fully compatible with automated liquid-handling systems and automated microscopes. The features of the devices are aligned precisely with a 96-well plate or 384-well plate Society for Biomolecular Screening (SBS) format. For example, the distance between the loading ports of gel chambers in series and in parallel is 9 mm, and the distance between the inlet and outlet ports of each individual tubular structure is 3.5mm. Here, we demonstrate integration of our device into an automated liquid setup for use in high-throughput experiments, **Figure 2.2A**. The Gilson Pipetmax robot was used to demonstrate pipetting operation, **Figure 2.2B**, including dispensing and liquid removal. The pipetting parameters, such as loading and retrieval speed to accommodate varying operation, such as surface coating, and fluidic properties (e.g., fluid viscosities), **Figure 2.2C**. The automatic dispensing system also allows precise volumes of liquids including ECM solutions to be loaded into individualized gel compartments on the assembled unit without mixing between gel compartments organized in series, **Figure 2.2D**.

To generate cell-lined tubular structures, we formed tubular intestinal epithelium using Caco-2 intestinal epithelial cells within a collagen type I (COL I) matrix. We first selectively coated the gel chamber of a PS device with polyethyleneimine (PEI), a positively charged polymer that enhanced collagen hydrogel adhesion to surface,

followed by glutaraldehyde (GA) treatment which aid in crosslinking collagen to the PEI coated substrate. Collagen hydrogels kept on ice were loaded onto the individually compartmentalized gel chambers and following polymerization at 37° C, excess PBS was placed on the inlet and outlet ports used for cell loading to displace the volume occupied by the Nylon string during removal. As previously described, the Nylon string was cut and removed to generate hollow tubular structures within COL I hydrogels. We found that filling the auxiliary chambers with a temporary hydrogel barrier prevented mixing between gel chambers in series during cell loading. We used a bovine COL I hydrogel at 3mg/ml, however, alternative hydrogel barriers including agar gel or fibrin gel may be used for this purpose. The excess PBS was removed and replaced with cell suspension at 17,000 cells/uL and the device was rotated 180° at an interval of 20 min for 2 h while incubating in a humidified chamber at 37° C to prevent evaporation. This facilitates cell adhesion to the matrix to form tubular structures. Cells that did not adhere to the matrix were then washed away by repeated pipetting using cell culture medium and the temporary hydrogel from the auxiliary chambers were aspirated off. The auxiliary chambers were then filled with culture medium to connect gel chambers in series or an immiscible liquid barrier (fluorinated oil) to prevent interaction. After reaching confluency in 1-2 days, the Caco-2 cells showed a stable morphology of a single monolayer against the gel forming epithelial tubes, as indicated by fluorescence staining of f-actin and the nuclei, **Figure 2.2E**. To minimize user interference and issues related to reproducibility during this process, we propose a workflow, **Figure 2.3**, to integrate automatic pipetting.

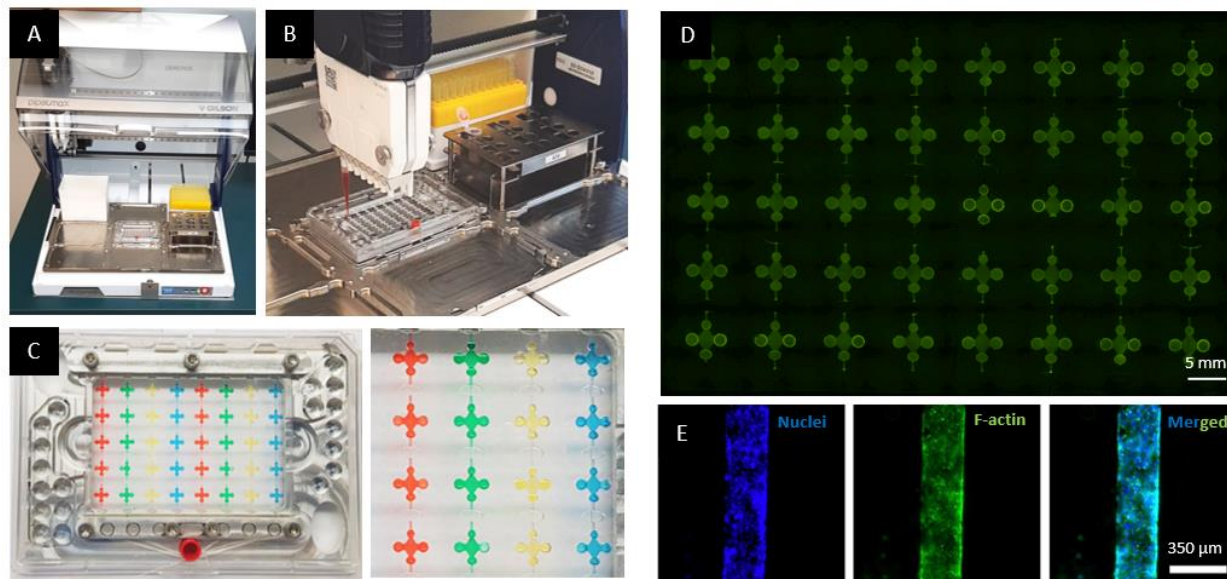
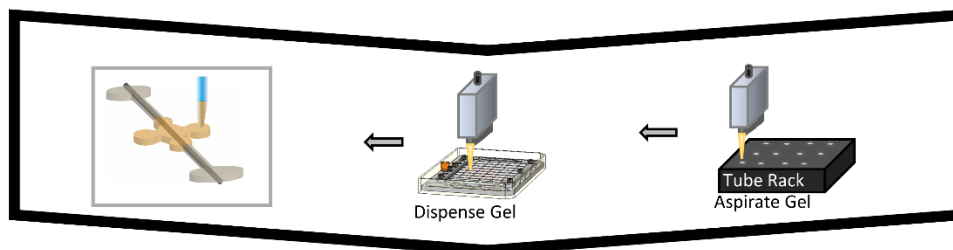
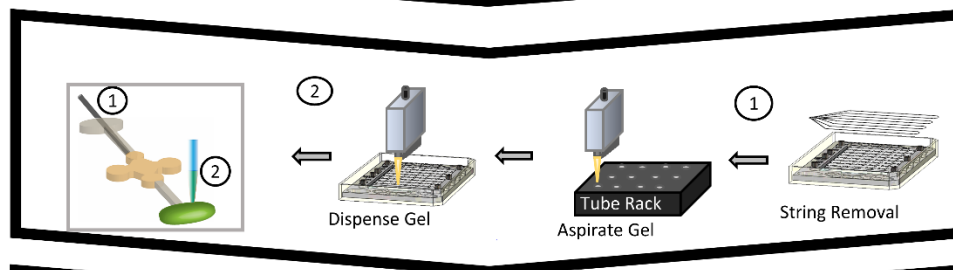


Figure 2.2 Device operation using liquid-handling setup. (A) Photograph of Gilson Pipetmax automatic liquid handling system. (B) Photograph showing liquid handling operations done by the Gilson Pipetmax robot on the tubular tissue array device. (C) Integration with Gilson Pipetmax accommodates robust liquid handling by dispensing different solutions into each tissue compartment. (D) Liquid handling can be performed on a variety of liquids including ECM hydrogel. Fluorescently (green) tagged-dextran solution was mixed with COL I gel and loaded onto the device using the liquid handler. (E) Caco-2 cells were used to generate tubular epithelium. Immunofluorescence image showing a confluent monolayer of cells stained for nuclei (blue) and f-actin expression (green).

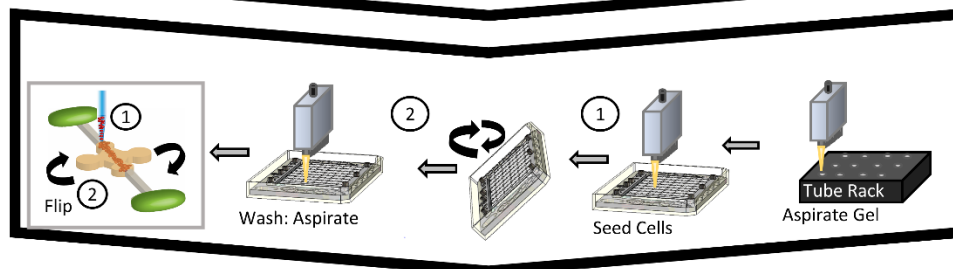
**Load Gel (4°C) &
Polymerize (37°C)**



**Remove String,
Load Gel at
Connection Ports
(4°C) & Polymerize
(37°C)**



**Seed Cells /
Generate Lumen
Structures (37°C) &
Wash Unadhered
Cells**



**Aspirate Gel +
Dispense Media or
Oil at Connection
Ports**

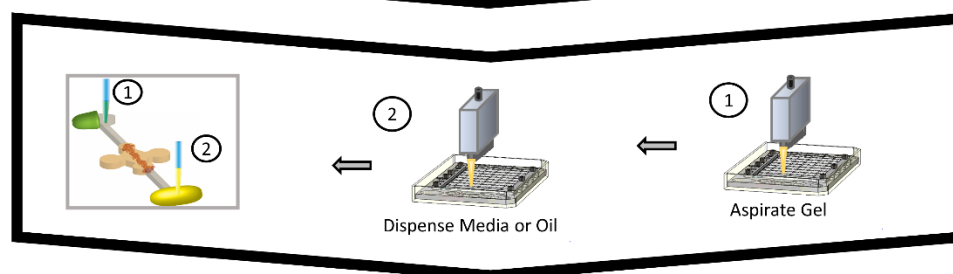


Figure 2.3 Illustration of workflow to integrate automated liquid handling.

2.2.3 Liquid Barrier Enabled Compartmentalization for Parallel Tissue Formation

In the previous section, we described how arrays of tubular structures within an ECM hydrogel can be formed in a reproducible manner with our platform. In this section, we explore array interconnections using liquid barriers and liquid bridges for compartmentalization or for creating gradients between adjacent culture systems. Cell culture medium or fluorinated oil is added to the auxiliary chambers between two consecutive culture chambers with tubular structures, **Figure 2.4A**, based on desired application. Owing to the availability of the pipet-accessible auxiliary chambers and interconnecting channels, the approach described here allows for compartmentalization of culture systems via the use of an immiscible liquid barrier. We have chosen fluorinated oil (FC-40) as an immiscible liquid barrier for this application. Fluorinated oils are widely used in droplet-based microfluidics and was chosen for two reasons: first, most organic compounds are insoluble in these oils making it suitable for its function as an immiscible barrier; and second, its biocompatibility for cell culture applications. By using fluorinated oil as a liquid barrier, parallel cell culture with discrete compartmentalization is achieved for multiple independent experimentation on the same device. On the other hand, for complex multi-tissue studies, the fluidic interconnections between culture systems in series with our device could be configured to create biochemical gradients. The auxiliary chambers between consecutive gel chambers are filled with a culture medium which connects the gel chambers through a liquid bridge. This allows us to form gradients between two consecutive gel chambers by adding a source to one gel chamber while the other acts as a sink.

The liquid repellent properties of fluorinated oil help to robustly separate interacting systems during regular cell culture experiments. We designed the auxiliary chambers to be non-circular and wider relative to the interconnecting channel width to prevent fluorinated oil from flowing into the culture chambers. To demonstrate the functionality of fluorinated oil as a liquid barrier, we examined the effects of adding excess liquid volume (20 μ L) in one culture chamber on the adjacent culture chamber, **Figure 2.4B**. Compared to a no media control, the fluorinated oil prevents mixing between chambers for robust compartmentalization during operation.

We also leverage the ability to connect adjacent systems via a liquid bridge to generate biochemical gradients. The complexity of tissue response and function is often shaped by the intricate patterns of stimuli inflicted on them in a space and time-dependent manner. Important signaling cues in cell biology are presented as concentration gradients, both at the subcellular level as well as in long range multi-tissue interactions. Microfluidic-based approaches have vastly improved our ability to control concentration gradients ^{70,71}. Flow-based devices can generate stable gradients quickly and maintain them over longer time periods, however subject cells to shear stress that aren't physiologically relevant. Diffusion-based gradient generators on the other hand alleviate the issue of shear stress by using gel-like materials ⁷², pressure balance between interconnecting chambers ^{73,74}, or porous membranes ⁷⁵ to conserve the presence of steep gradients. We demonstrate that using a liquid bridge between adjacent culture chambers, we can generate a diffusion-based linear gradient over prolonged periods of time. The long distance (millimeter scale relative to microscale) distance (4.5 mm or 9

mm) between culture chambers allows for longer diffusion time. This principle was experimentally validated by flowing cell culture medium containing fluorescently labeled dextran (70 kDa fluorescein isothiocyanate dextran) and by monitoring fluorescent signals to assess concentration, **Figure 2.4Ci**. A polystyrene 80-system device with distance of 4.5 mm between gel chambers was used in this experiment. Adding 70 kDa-dextran to the bottom chamber established a vertical gradient, **Figure 2.4Cii**. Although a gradient may still be present for several days, we monitored the gradient for 24 h as this is the average time between media and growth factor replacement in the device. Using a liquid barrier did not establish a gradient, **Figure 2.4Ciii** and this was confirmed by measuring concentration profiles of 70 kDa dextran in the adjacent chamber (at position B, Figure 2.4Ci) after 24 h, **Figure 2.4D**. The experimental diffusion assays behaved very similarly to what theory predicts (around 18% of the concentration in position A at time 0), as assessed by COMSOL computational simulations conducted on a simplified geometry, **Figure 2.4E-F**. Altogether, the ability to accommodate robust compartmentalization and establish biochemical gradients for prolonged periods offer opportunities to explore long-range spatial signaling such as multi-organ interactions. While well-plate and dish assays for adherent cultures remain the most convenient *in vitro* platforms for high-throughput applications, the more physiologically relevant 3D architectures in such traditional platforms are challenging to control. For such research questions, microfluidic systems, such as the one presented here, represent an attractive alternative, and integrating automation into these systems could compete with the throughput of traditional assays.

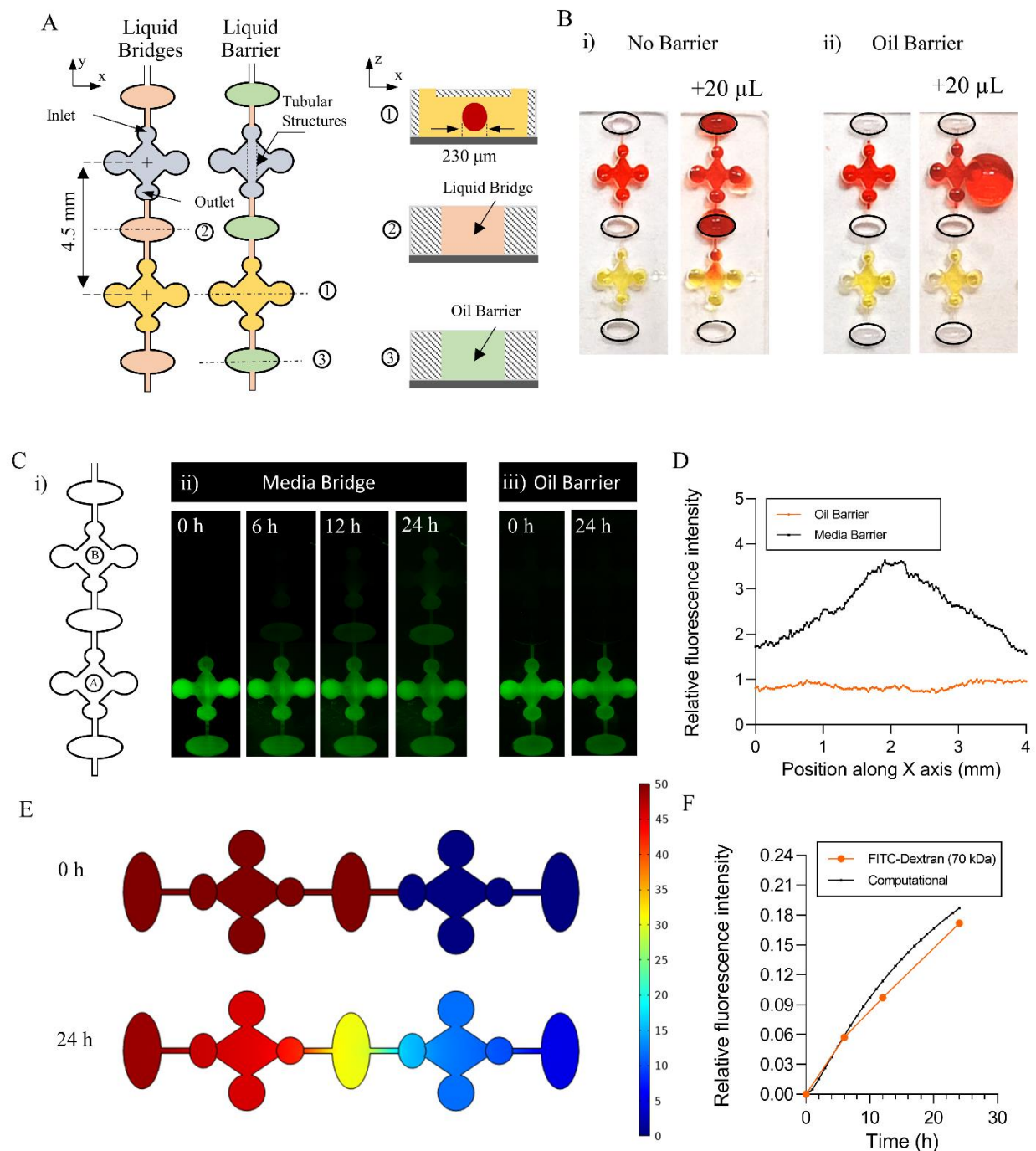


Figure 2.4 Characterization of fluidic interconnection within the tubular tissue structure array device. (A) Schematic illustration of the liquid bridge and liquid barrier setup. Tissue chambers are 4.5 mm apart, with an auxiliary chamber in between to make fluidic connections by adding liquid or to compartmentalize by using an oil barrier. (B) Photograph demonstrating functionality of the liquid bridge and the liquid barrier. A liquid bridge allows communication between tissue compartments and a liquid barrier prevents communication. (C) Characterization of diffusion-based gradients that can be generated using cell culture medium as a liquid bridge. 70 kDa fluorescein isothiocyanate dextran mixed in cell culture medium was added to tissue

compartment A, and molecular-diffusion of dextran was monitored over 24-h period (i). Dextran diffusion into compartment B is observed after 24-h in the media bridge system (ii). Liquid barrier prevented dextran diffusion into compartment B (iii). (D) Fluorescent intensity profile across tissue compartment B after 24 h. (E) Gradient formation simulated in the simplified computational model using COMSOL Multiphysics. Color bar represents concentration in micromolar. (F) Time course of the concentration C at the center point of the tissue compartment B expressed as a fraction of the bulk concentration added to compartment A. Concentration of dextran diffusion, as measured by fluorescence intensity is also plotted as a fraction of the intensity measured at the center point of compartment A.

2.2.4 Liquid Barrier Enabled On-Demand Co-Culture

Owing to the ability to compartmentalize tissues on-demand, the liquid barrier approach allows for parallel development of individualized 3D tissues, without interference (markers and signaling molecules) from other tissue compartments. Moreover, time-dependent inter-tissue communication can be established by first selectively stimulating one tissue compartment while preserving the other, then establishing co-cultures. To demonstrate time dependent inter-tissue communication, we implemented a new design incorporating multiple tubular structures, separated by a barrier compartment, within the same tissue/culture system. The array configuration was modified to accommodate the new design, **Figure 2.5A**. We implemented a mammary model that incorporates a breast cancer cell-derived duct surrounded by a COL I matrix to model early-stage breast cancer. Prior to gel loading, the barrier compartment was filled with fluorinated oil to separate the gel compartments, **Figure 2.5B**. The two lumens in each device were lined with MCF7 cells, an immortalized human mammary epithelial cancerous cell line, and parallel cultures were established without interactions. Docetaxel, an FDA-approved chemotherapeutic agent for locally advanced or metastatic breast cancer, was perfused through the left MCF-7 breast duct and incubated for 24h with the liquid barrier while the MCF-7 breast duct on the right was incubated in culture medium. Dead MCF-7

cells were quantified via LIVE/DEAD cell staining, **Figure 2.5C**. When compared to the system where the MCF-7 ducts were connected by a media bridge, the untreated MCF-7 duct in the system with a liquid barrier had lower fraction of dead cells, further validating the ability of the FC oil liquid barrier to compartmentalize cultures, **Figure 2.5D**. To then facilitate inter-tissue interactions, the liquid barrier was removed, and the two MCF-7 ducts were connected by a media bridge. The MCF-7 ducts on the left in both systems (previously connected via liquid ridge and sequentially connected by liquid bridge) were treated again with the same dose of docetaxel for an additional 24 h. MCF-7 ducts on the right in both systems showed an increased number of dead cells, as quantified by area covered by dead cells, **Figure 2.5E**. This demonstrates how FC oil liquid barrier can be exploited to temporally control interactions between two tissue compartments. While in this demonstration two tubular tissue structures were generated using the same cell type, future experiments could examine the effects of drug treatment on one tissue type on a secondary tissue type in a time-dependent manner.

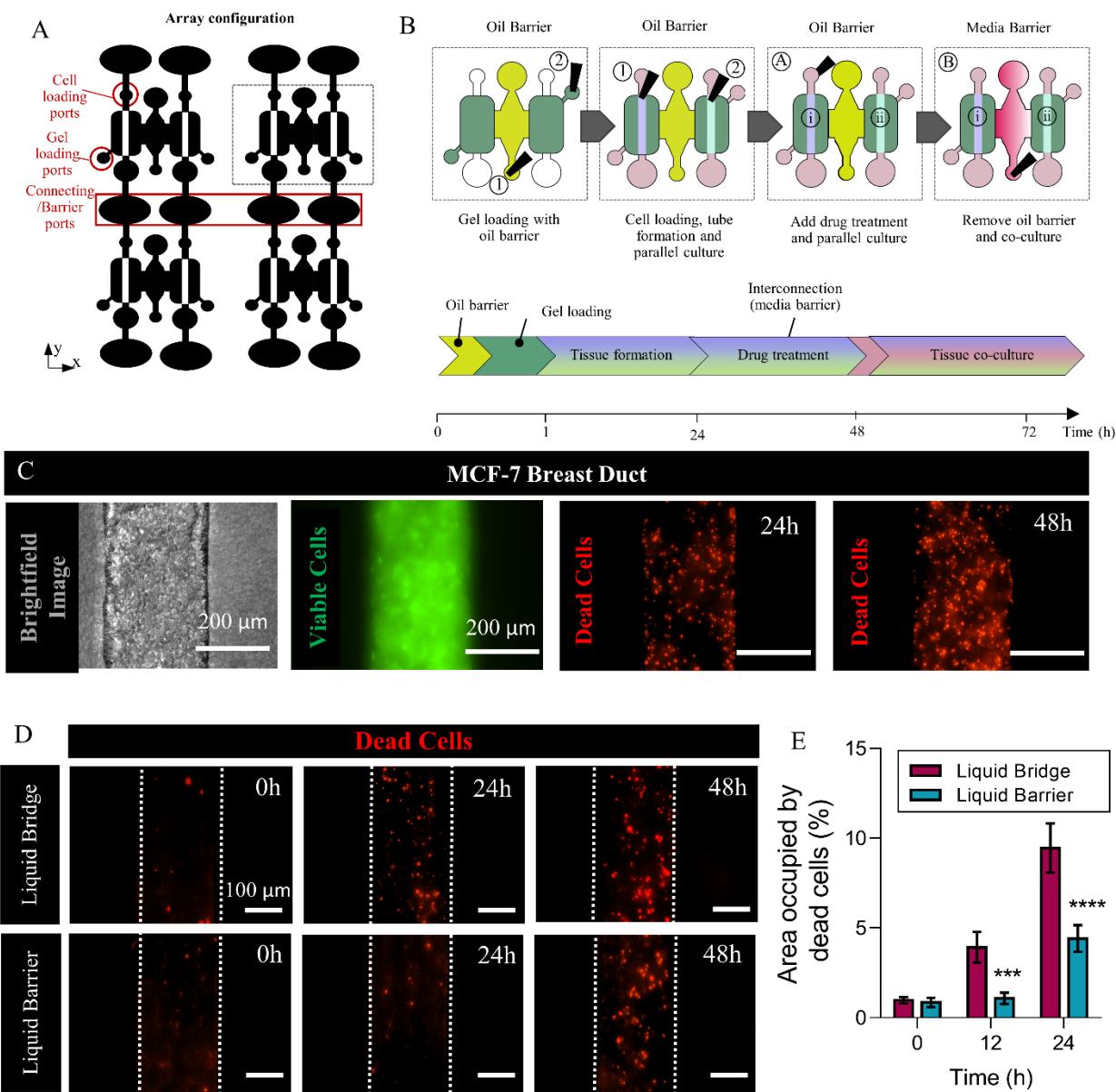


Figure 2.5 Compartmentalization and subsequent co-culture demonstration using FC oil liquid barrier. (A) Adjusted array configuration for a new design of a tissue system consisting of two tubular structures. (B) Schematic illustration describing the workflow and timeline used to demonstrate compartmentalization followed by co-culture using liquid barriers. Two mammary ducts are generated using MCF-7 breast cancer cells simultaneously using an oil barrier. The duct on the left was treated with a chemotherapeutic drug (docetaxel) for 24h in an interconnected (liquid bridge) and a compartmentalized (oil barrier) setup. In the compartmentalized setup, the oil barrier was removed and the duct on the left in each setup was treated again with docetaxel for an additional 48h. (C) Representative brightfield image showing MCF-7 cell-derived tubular ducts. Immunofluorescence images showing viable cells (green) and dead cells (red) in mammary ducts at position (i) after 24h and 48h of direct treatment with docetaxel. (D) Immunofluorescence images showing dead cells (red) in mammary ducts at position (ii), in interconnecting (liquid bridge) and compartmentalized (liquid

barrier) systems, after mammary ducts in position (i) were treated with docetaxel following the workflow described in (B). In the compartmentalized system, the FC oil barrier was removed after 24h. (E) Bar graph showing area occupied red positive cells indicating dead cells in mammary duct at position (ii), asterisk denotes **** $p \leq 0.0001$, and ** $p \leq 0.001$.

2.2.5 Liquid Barrier Reconfiguration

Current efforts to compartmentalize tissue chambers in MPSs rely on the use of microscale features (e.g., microposts) and silicon-based materials⁷⁶, which have limited utility in some research and commercial settings^{68,77,78}. Moreover, fabrication of these technologies requires high-resolution soft lithography, making it difficult to scale up manufacturing and challenging to integrate into some research settings. For example, laser engravers, while continuing to improve in resolution, are not able to pattern free-standing microscale features that facilitate compartmentalization as well as soft lithography-based methods. Phaseguides and microposts act as capillary pressure barriers for filling dead angles, mixing, and preventing gel from flowing into an adjacent channel⁷⁹. However, this technology only confines the gel to a compartment and loses its function when the gel compartments are connected by cell culture media. This creates a liquid bridge between gel compartments that cannot be reversed as the media components (i.e., proteins and growth factors which are hydrophilic) change the interconnecting surface chemistry towards hydrophilicity.

Herein, we demonstrate the potential of a reconfigurable liquid barrier to reverse this surface modification by cell culture. Dissimilar to microposts and phaseguides, a reconfigurable liquid barrier can re-compartmentalize tissue compartments after they have been connected by a liquid bridge in our device. Furthermore, unlike microscale

features which require high resolution-based methods to fabricate, the addition and removal of FC oil barrier can be done by simple pipetting.

To demonstrate the robust capabilities of the reconfigurable liquid barrier, we used the FC oil as a switch to control user-imposed pH in two interacting gel compartments, **Figure 2.6A**. We formed breast cancer cell-derived (MCF-7) duct surrounded by COL I gel in one compartment (right) as before and embedded colon cancer cell line (HCT 116) in COL I gel in the other compartment (left) using the parallel co-culture method, **Figure 2.6B**. At first, to demonstrate compartmentalization by FC oil we added PBS solution calibrated at pH 7.0 to breast duct compartment while the colon cancer cell compartment remained unchanged and measured the intracellular pH using a fluorescent pH indicator (SNARF-1). SNARF-1 AM fluorescence was detected at 580 (green channel) and 640 nm (red channel) for each scenario. The 580/640nm ratio, along with a pH calibration curve was used to calculate the intracellular pH.

As demonstrated in the fluorescence images and intensity plot profiles, no signal was detected in the colon cancer compartment while the breast cancer duct compartment showed fluorescent signals, **Figure 2.6C i**. The FC oil barrier was then removed, and the two compartments were connected by PBS bridge (not pH adjusted), and PBS (pH adjusted to 7.8) was added to the colon cell compartment allowing a pH gradient to be established, **Figure 2.6C ii**. This allowed the fluorescence signals in the colon cancer compartment to increase. Finally, to demonstrate re-compartmentalization or reconfigurable properties of the liquid barrier, the FC oil was reintroduced between the

two gel compartments. PBS (pH adjusted to 7.2) was then added to the colon cancer cell compartment, resulting in a change in the ratios of fluorescence intensity, **Figure 2.6C iii**. Taken together, the ability to bridge then separate interconnections between tissue compartments demonstrates the potential to do dynamic reconditioning experiments that would not be possible without a reconfigurable barrier. The pH, corresponding to the fluorescence intensity ratios, are plotted across the device for each scenario, **Figure 2.6D**, demonstrating the ability to compartmentalize, connect then re-compartmentalize tissue compartments in the same device.

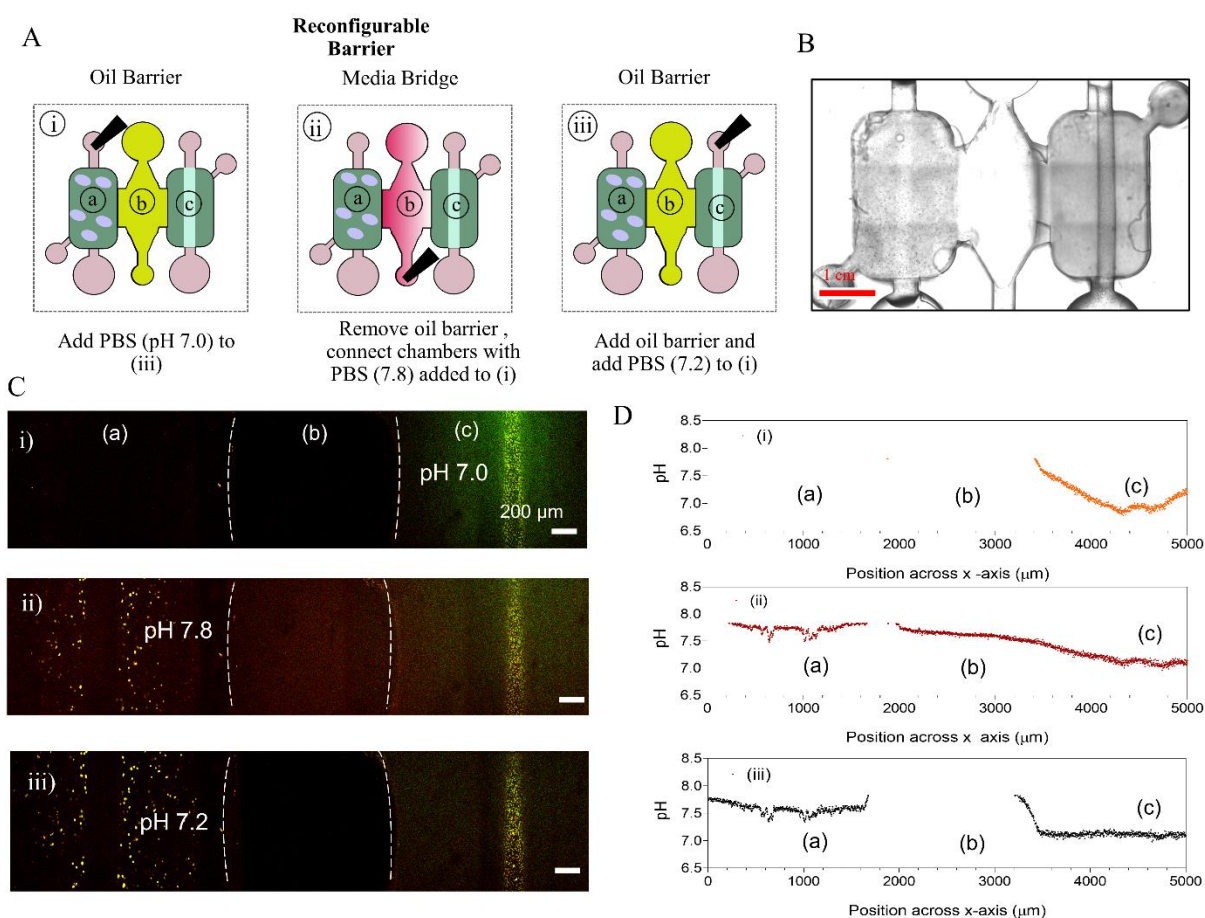


Figure 2.6 Characterizing functionality of reconfigurable liquid barrier. (A) Schematic illustration describing the workflow and timeline used to demonstrate liquid barrier reconfiguration for multi-tissue interactions using three scenarios, i, ii and iii. HCT-116 colon cancer cells were embedded in COL I hydrogel on the left and MCF-7 cell derived mammary ducts were formed on the right. In scenario i, the mammary duct is exposed to pH 7.0 while

separated from the colon cancer cell compartment via oil barrier. Then, in scenario, ii, the oil barrier is removed enabling communication between the two tissue compartments, and the colon cancer cell compartment is exposed to pH 7.8. Subsequently, in scenario iii, the oil barrier is added to re-compartmentalize the two tissues and the colon cancer cells were exposed to pH 7.2. (B) Representative phase contrast image showing colon cancer cells on the left and MCF-7 cell derived mammary duct on the right. (C) SNARF-1 AM fluorescence was detected at 580 nm (green channel) and 640 nm (red channel) for each scenario and the overlay is shown. (D) Graph shows the estimated pH across the two compartments at locations (a), (b) and (c) in scenario i, in scenario ii, and in scenario iii. The estimation was performed using the calibration curve.

The different demonstrations in this chapter provide evidence of the large potential of the approach described for a new high content assay platform. Regular tubular tissue arrays as well as more complex tissue interactions have been presented enabling experimentation in a high-throughput manner for multiple applications including cell biology, drug screening and tissue-on-a-chip modeling. For future applications, the central advantages of the presented approach include the possibility to establish continuous inter-tissue fluidic communication and perfusion. Due to the compatibility of fabrication methods, flexibility in designing the fluidic connections and barriers will enable a broad variety of experiments, which cannot be done in isolated systems

In summary, we presented a unique methodology that can rapidly generate arrays of tubular tissue structures and that can perform complex multi-tissue experimentation on a single microfluidic device. We demonstrated that the platform could support complex multi-tissue interactions including parallel, on-demand and reconfigurable co-culture. Overall, the platform features high usability and a multitude of functions, while keeping handling complexity at a minimum. If applied, this platform can play an important role in providing new insights into organ system-based interactions, for example in multi-organ

studies involving drug metabolism. This platform has the potential for advanced disease modeling and *in vitro* therapeutic drug and toxicology screening that can help accelerate drug development research.

2.3 Materials and Methods

2.3.1 Device Fabrication

The device ECM chamber was fabricated using soft lithography. The masks were designed using Adobe Illustrator and printed on a transparency. The layers were spun with SU-8 100 (Y13273 1000L 1GL, MICRO CHEM, Newton, MA) according to the manufacturer's specifications on a silicon wafer (CC-1385, WRS, San Jose, CA). After the photoresist was soft baked on a hot plate, a UV light source was used to transfer the device pattern from the printed mask to the photoresist. A post-exposure hard-baking step was executed. This process was repeated for additional layers. Upon completing all the layers, the mold was developed for 45 mins in SU-8 developer solution (PGMEA, 537543, Sigma, St. Louis, MO) and washed with iso-propyl alcohol and DI water after development. Poly-dimethylsiloxane (Sylgard 184 silicone elastomer base, 3097366-1004, Dow Corning, Salzburg, MI) (PDMS) was prepared at a ratio of 1:10 curing agent (Sylgard 184 silicone elastomer curing agent, 3097358-1004, Dow Corning, Salzburg, MI) and degassed in a vacuum for 30 mins. The PDMS was then poured over the SU-8 silicon mold on a hot plate and baked at 80 °C for 4 h.

2.3.2 Polystyrene Device Fabrication

Polystyrene devices were fabricated by CNC milling (PCNC 770, Tormach, Waunakee, WI) of 1.2 mm thick PS (ST313120, Goodfellow, Coraopolis, PA). The device was designed on Solidworks 2019, and then converted to machine code compatible with the mill using SprutCAM 11 software. The following drill bits were utilized from Performance Microtool to fabricate the PS microfluidic devices: square end mills/two flute/ diameters 0.0312" and 0.01". After milling, the PS device was submerged in IPA for two hours to clean it

2.3.3 Stage Design and Fabrication

All aluminum stage parts were first designed on Solidworks, and then converted into machine code compatible with Tormach Personal CNC 770 Series 3 mill by SprutCAM 11 software. All aluminum parts were fabricated from larger blocks of aluminum. To achieve all design features on all aluminum parts (i.e., the aluminum stage and both aluminum immobilizers) the following drills bits were used from Performance Microtool: square end mills/two flute/diameters 0.0625" and 0.02", ball end mill/diameter 0.0312", square end mills/two flute/diameters 0.25", 0.156", and 0.125". Once fully milled, sharp edges on the stage are shaven away using a deburring tool, and corners and sides are sanded to provide for a smooth fit into the single-well OmniTray.

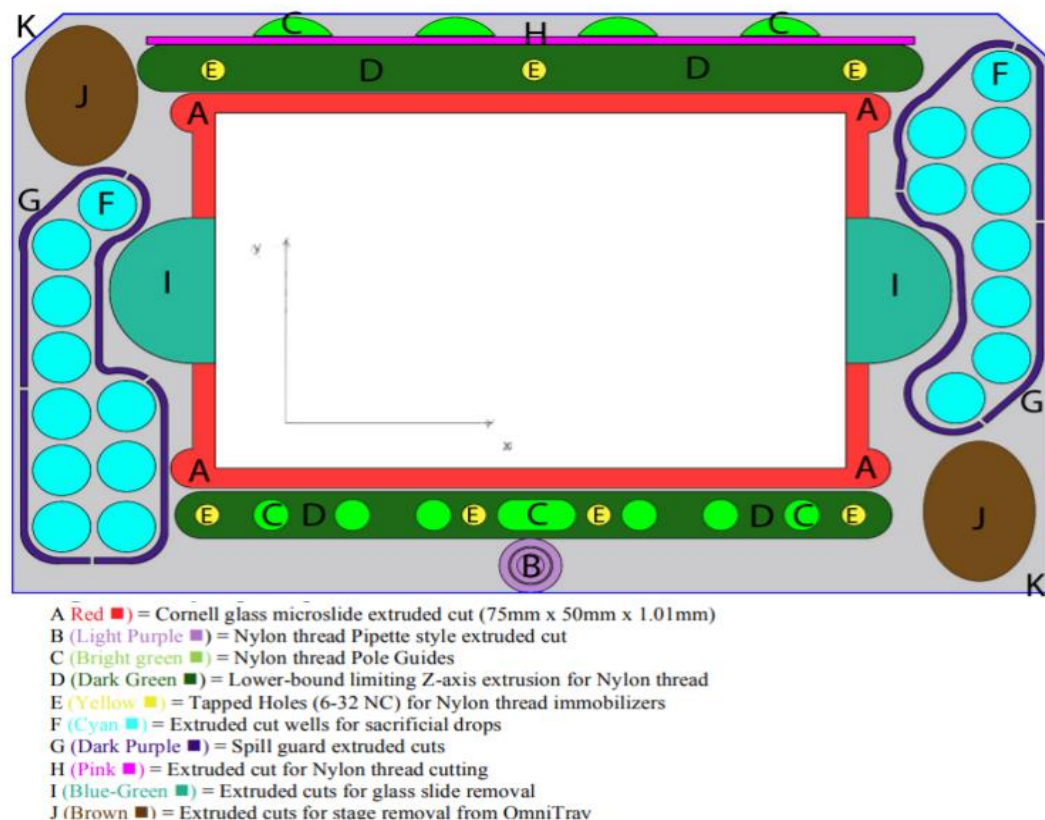


Figure 2.7 Key design features of the stage.

2.3.4 PDMS Device Bonding to Glass Slide

For PDMS chambers, there are two ways to bond the part to the glass slide. For non-permanent bonding, 70% ethanol was used to bond the PDMS part. To permanently bond the device to a glass surface, the device and the glass slide were oxygen-plasma treated (Femto, Thierry Corp., Royal Oak, MI). After plasma treatment and system assembly, the PDMS is carefully placed on the glass slide. Last, the 3D printed wrapping pole was first designed on Solidworks, and then converted to .STL file type to be printed via the MakerBot replicator desktop 3D printer. The 3D printed wrapping pole is made from Natural PLA provided by MakerBot.

2.3.5 Nylon Threading

Nylon thread is placed around the guiding poles on the stage using the map shown in **Figure 2.7**. First, push the 3D printed pipette tip Nylon thread holder into place. Then, tie the Nylon thread around the holder with a double knot. Holding the Nylon thread taut and rotating the stage around the Nylon thread, wrap the Nylon thread around the poles as shown. After returning to the pipette tip holder at the bottom of the stage, each time, rotate the stage three times so that the string is wrapped around the 3D printed holder three times. Repeat this after each consecutive wrapping step (Wraps 1-4 are shown in **Figure 2.7**). Once the Nylon thread is wrapped properly around the poles and pipette tip, cut the Nylon thread and secure it with a piece of tape.

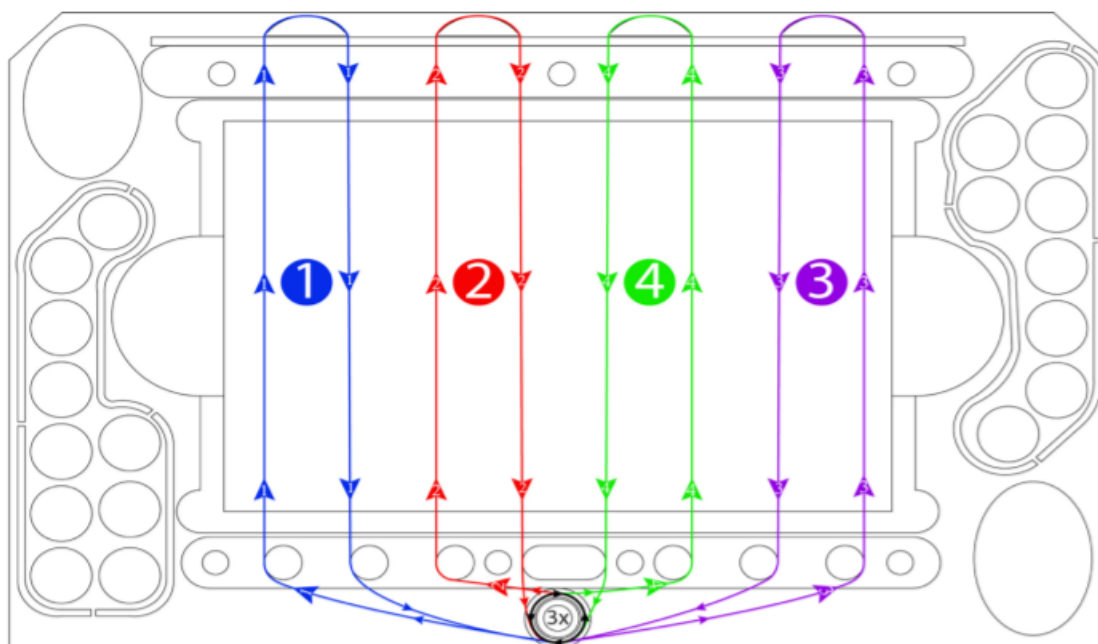


Figure 2. 8 Nylon threading configuration.

2.3.6 Collagen Gel Preparation

The following steps were carried out on ice to prevent fast polymerization of collagen. For a collagen solution with a final concentration of 6mg/ml, 80µl of rat tail collagen type-1 10mg/ml (354249, BD Biosciences, San Jose, CA) was combined with 20µl of 5X PBS and 3µl of 0.5 N Sodium Hydroxide (S318, Fisher Scientific, Pittsburgh PA). The mixture was incubated on ice for 20 mins. Finally, 34µl of PBS was added for a final collagen concentration of 6mg/ml and a pH of 7.4.

2.3.7 Gilson Pipetmax Robot Setup

The Gilson Pipetmax robot has capacity for a total of nine bed layout items (racks). This experiment requires four racks for use: the OmniTray stage setup, one tube rack on ice bed for collagen gel, a D200 pipette tip rack with a minimum of 15 pipette tips, and a pipette tip waste disposal bin. Empty the pipette tip waste disposal bin. Make sure the D200 pipette tip rack is filled with at least 15 pipette tips. Fill the OmniTray stage setup sacrificial liquid extruded cuts to the top with sacrificial drop solution to help prevent evaporation when the lid is on. Fill wells 9-13 with 500µL of collagen solution. Place all four racks into the designated area of the robot bed. Cover OmniTray stage setup with lids until fully prepared for experimentation.

2.3.8 Cell Culture

Colon cancer HCT-116 cells (ATCC) were cultured in RPMI 1640 (Thermo Fisher, 21870076) supplemented with 10% FBS (Thermo Fisher, 26140079). MCF-7 cells were grown in high glucose DMEM (4.5 mg/ml, Gibco, Gaithersburg, MD, USA; #11965092)

supplemented with 10% fetal bovine serum (FBS, VWR #97068-085) and 1% penicillin/streptomycin (Thermo Fisher, Waltham, MA, USA; #15140-122) and maintained in a 5% CO₂ 37°C incubator. Cells were trypsinized and resuspended at 17 million MCF-7 cells for tube formation. A 4.0 mg/ml collagen hydrogel containing 1 million HCT-116 cells/ml was prepared as follows: 10 µl of 10× PBS, 2.45 µl of 1M NaOH, 97.8µl of 8.43 mg/ml COL I, and 100 µl of cell suspension. The collagen hydrogel was injected into the chamber of the microdevice and polymerized at room temperature for 20 minutes. The PDMS rod was removed using sterilized tweezers after collagen polymerization. This generated a tunnel in the hydrogel through which media was perfused to nourish the cells. 5 ml of cell culture media was then added to the Petri dish and the devices were placed in an incubator at 37°C with 5% CO₂.

2.4 Acknowledgments

This work was supported by NIH R01 EB010039, University of Wisconsin Carbone Cancer Center Support Grant NIH P30 CA014520, the University of Wisconsin Graduate Engineering Research Scholars, and the University of Wisconsin T32 Hematology training grant T32 HL07899. We thank a predoctoral fellowship (F31CA247248) from the National Institute of Health (NIH) to M.H.

Chapter 3

Elucidating cancer-vascular paracrine signaling using a human organotypic breast cancer cell extravasation model

In cancer metastasis, extravasation refers to the process where tumor cells exit the bloodstream by crossing the endothelium and invade the surrounding tissue. Tumor cells engage in complex crosstalk with other active players such as the endothelium leading to changes in functional behavior that exert proextravasation effects. Most *in vitro* studies to date have only focused on the independent effects of molecular targets on the functional changes of cancer cell extravasation behavior. However, singular targets cannot combat complex interactions involved in tumor cell extravasation that affects multiple cell types and signaling pathways. In this study, we employ an organotypic microfluidic model of human vasculature to investigate the independent and combined role of multiple upregulated secreted factors resulting from cancer-vascular interactions during cancer cell extravasation. The model comprises a tubular endothelial vessel generated from induced pluripotent stem cell derived endothelial cells within a collagen-fibrinogen matrix with breast cancer cells injected through and cultured along the lumen of the vessel. Our system identified cancer-vascular crosstalk, involving invasive breast cancer cells, that resulted in increased levels of secreted IL-6, IL-8 and MMP-3. Our model also showed that upregulation of these secreted factors correlates with invasive/metastatic potential of breast cancer cells. Moreover, we used therapeutic

inhibitors to assess the independent and combined role of multiple signaling factors on the overall changes in functional behavior of both the cancer cells and the endothelium that promote extravasation. Taken together, these results demonstrate the potential of our organotypic model in elucidating mechanisms through which cancer-vascular interactions can promote extravasation, and in conducting functional assessment of therapeutic drugs that prevent extravasation in cancer metastasis.

This chapter has been adapted from a published manuscript in the journal *Biomaterials* titled "Elucidating cancer-vascular paracrine signaling using a human organotypic breast cancer cell extravasation model" (2021)⁸⁰. The manuscript was authored by Mouhita Humayun, Jose M. Ayuso, Raven A. Brenneke, María Virumbrales-Munoz, Sheena Kerr, Karina Lugo-Cintron, Suzanne M. Ponik, David J. Beebe

3.1 Introduction

Breast cancer is the second leading cause of cancer-related death in women⁸¹. Most patients who experience relapses display disseminated metastases rather than isolated local recurrences⁸². Thus, targeting metastasis, especially in the later stages of cancer progression, is critical to improving patient outcomes.

One key event in the metastatic cascade is the extravasation of circulating tumor cells (CTCs) out of blood vessels. Extravasation of tumor cells involves two critical steps: 1) arrest of CTCs on the blood vessel endothelium and 2) migration of CTCs across the endothelium through a process called transendothelial migration⁸³. Recent findings suggest that multiple routes exist leading to each event in the extravasation process. For instance, CTCs can be arrested not only by entrapment within capillary vessels/capillary bifurcations where the capillary diameter is less than the diameter of CTCs, but also by attachment to the endothelia of larger vessels where the shear flow is relatively low, via strong adhesion⁸⁴. Entry into the perivascular space can also involve several mechanisms including CTC migration across an intact endothelium via a paracellular route or transcellular migration by disruption of the endothelium⁸⁵. Understanding the molecular signaling that governs tumor cell behavior (i.e., adhesion, proliferation, and migration) and its interactions with surrounding tissue (i.e., the endothelium) during extravasation are crucial to identifying potential therapeutic targets for metastatic spread.

Currently, breast cancer metastasis can be studied in mice by tail vein, intracardial or orthotopic injections of breast cancer cells¹¹. However, in addition to low throughput due to practical constraints on the use of animal models (e.g., cost and time), there are important differences between human and mouse biology that hinder the identification of actionable targets in the clinic. *In vitro* approaches, on the other hand, often lack the three-dimensional (3D) complexity, spatial organization and relevant cell-to-cell and cell-extracellular matrix (ECM) interactions for modeling *in vivo* responses. Thus, there is a compelling need for human-relevant *in vitro* models that can reflect relevant 3D architectures of the *in vivo* microenvironment and capture the complex process of cancer metastasis.

Tumor cell extravasation into intact organs has been observed in animal models, but these events are rare and transient in nature, making it a difficult process to study. Organ-on-a-chip modeling techniques enable us to create multi-organ interactions and generate organ-specific tissue functions by providing precise control over 3D environmental features (e.g., tissue architectures and biomechanical cues), and microenvironmental interactions (e.g., cell-to-cell, cell-matrix, and soluble factor signaling)^{86,87}. In recent years, several microengineered platforms have been reported that can better recapitulate the interactions between human-relevant cells sources (e.g., cancer cells and endothelial cells) and the ECM observed *in vivo* to gain mechanistic insights into the process of cancer metastasis^{88–91}. Moreover, microfluidic *in vitro* models of tumor cell extravasation are beginning to emerge, and these models are specifically well-suited to investigate cancer-specific molecular mechanisms resulting

from biophysical and biomolecular cues that would otherwise be challenging in conventional *in vitro* systems^{15,92}. These microfluidic devices have been designed to model tissue invasion⁹³, systemic flow of tumor cells in circulation and their endothelial capture from flow, and subsequent extravasation through the endothelial monolayer¹⁷ or microvascular networks¹⁹ towards a chemotactic gradient generated by organ-specific cells^{94–96}. As tumor cells are not independent players in metastatic spread, several studies using these models have shed light on the impact of cancer-associated interactions with immune cells^{97,98}, the vasculature^{99,100}, and the underlying extracellular matrix containing components of secondary metastatic sites^{94,95 96} (e.g., bone and muscle) in generating pro-extravasation effects. These findings underscore the importance of exploring cancer-associated molecular signaling and cancer cell-mediated changes to the microenvironment, such as matrix remodeling, endothelial activation, and impairment to endothelial barrier function as potential therapeutic targets in metastatic progression. However, most investigations of tumor cell extravasation have been limited to examining the independent effects of molecular targets on cancer cell behavior, and often lack insight into cancer-associated molecular and functional changes to the microenvironment. Moreover, these microscale models have not been exploited to study the direct involvement of multiple signaling interactions and their additive influence on the creation of microenvironments facilitating cancer cell extravasation. In this work, we investigate the role that several cancer-vascular signaling factors play, individually and in combination, in altering cellular function and the components of the microenvironment to promote tumor cell extravasation.

In this study, we employ a human organotypic vascularized model to study breast cancer cell (BCC) extravasation and cancer-vascular interactions that facilitate modulation of endothelial properties and increase events of extravasation. One of the advantages of our approach is that the arrayable microfluidic platform allows us to directly investigate different combinations of therapeutics to probe specific molecular signaling factors in a robust and controlled manner. In particular, we identify multiple molecular targets and examine their influence on the functional behavior of cancer cells and the endothelium during extravasation. Our results show that BCCs can activate endothelial cells (ECs) through paracrine signaling and modulate components of the endothelial basement membrane during extravasation and, moreover, that paracrine signaling alone has significant impact on vascular barrier function. We examine the role of cancer-mediated IL-6, MMP-3 and IL-8 paracrine signaling in vascular disruption, basement membrane degradation and increased extravasation events using clinically active therapeutics. Finally and most importantly, we demonstrate the individual and combined effects of these molecular targets on the overall molecular secretion profiling and functional responses of both cancer cells and the endothelium. Our findings provide a strong rationale for exploring additive and synergistic effects of multiple signaling interactions as therapeutic approaches for preventing cancer cell metastatic progression.

3.2 Materials and Methods

3.2.1 Organotypic Vascular Device Fabrication and Assembly

The organotypic model of cancer cell extravasation presented here is fabricated using the LumeNEXT platform⁶⁶. Details of device fabrication and vasculature model formation can be found elsewhere^{66,101}. This approach allows for fabrication of one or more lumen structures with variable sizes, configuration and lumen spacing controlled by micromold design in soft lithography. Here, a three-lumen device was designed, with each lumen having a separate inlet and outlet port oriented in parallel to one another. All lumens were designed to be within a single chamber accompanied by perpendicularly oriented side ports. Two stacked PDMS layers, with microscale features patterned into them, formed the chamber with three lumen structures in which ECM gels can be loaded, **Figure 3.1A**. Once the gel is polymerized, removable PDMS rods form the hollow lumen structures surrounded by an ECM gel. PDMS rods used in this study were approximately $\sim 250\ \mu\text{m}$ in diameter and $\sim 500\ \mu\text{m}$ apart. The gel was $\sim 3\ \text{mm}$ in length, $\sim 5\ \text{mm}$ in width and $1.25\ \text{mm}$ high, **Figure A.1**. Once assembled, the PDMS layers were oxygen-plasma bonded onto a glass-bottom culture dish (P50G-1.5–30-F, MatTek Corporation, Ashland, MA) using a Diener Electronic Femto Plasma Surface System.

3.2.2 ECM Gel Preparation and Loading

The bonded devices were UV sterilized for 20 min and moved to the biosafety cabinet prior to ECM gel loading. To promote matrix adhesion to PDMS, the device chambers were treated with 2% polyethylenimine (03880, Sigma-Aldrich, Saint Louis, Missouri) in

deionized (DI) water solution for 10 min, followed by a 30 min treatment of 0.1% glutaraldehyde (G6357, Sigma-Aldrich, Saint Louis, Missouri) in DI water at room temperature. Devices were then flushed with DI water solution 5 times to remove excess glutaraldehyde. A mix of rat-tail collagen type I solution (Col-I) (354249, BD Biosciences, San Jose, CA) neutralized with 0.5N sodium hydroxide (1310-73-2, Fisher Scientific, Pittsburgh, PA), fibrinogen (9001-32-5, Sigma-aldrich, St. Louis, MO), 7.5 pH 5X phosphate buffered saline (PBS) and Induced pluripotent stem-cell derived endothelial cells (iPSC-EC) complete growth medium was prepared at a final concentration of 3 mg/mL Col-I and 1 mg/mL fibrinogen to form the ECM gel. The pH of the ECM mix was adjusted to 7.2 pH prior to loading the mix into the gel-chamber of the device. 15 μ L of prepared gel solution was loaded into each device and incubated at room temperature for 20 min then moved to an incubator at 37°C for 1 h.

3.2.3 Cell Culture

iPSC-ECs (Cellular Dynamics International, Madison, WI) were maintained in Vasculife Basal maintenance media (LM-0002, LifeLine Cell Technologies Frederick, MD) supplemented with iCell Endothelial Cell Medium Supplement (Cellular Dynamics International) and used up to passage 6. GFP expressing MCF-7 cells and MDA-MB-231 cells were generated by infecting cells with lentiviruses expressing turbo-GFP (pGIPz-turboGFP vector, purchased from Addgene) and selecting for stable expression in 5 μ g/ml puromycin for 5-7 days. MDA-MB-231 triple negative breast cancer cells and MCF-7 HER2 negative breast cancer cells were cultured in DMEM (ATCC, Manassas, VA) supplemented with 10% fetal bovine serum (FBS, 35-010-CV, Corning-cellgro,

Manassas, VA) and 1% Penicillin-Streptomycin (Pen/Strep, 15070063, ThermoFisher Scientific, Waltham, MA,) up to passage 20. Hs-578T triple negative breast cancer cells were maintained in DMEM (ATCC) supplemented with 10% FBS (Corning-cellgro), 0.01 mg/ml bovine insulin (ThermoFisher Scientific) and 1% Pen/Strep (ThermoFisher Scientific) up to passage 12. Prior to cell seeding within the device, Hs-578T cells were stained with CellTracker Green CMFDA (C7-25, ThermoFisher Scientific) in PBS for 10 min.

3.2.4 Cell Seeding and Lumen Formation

To generate lumen structures, a droplet of 30 $\mu\text{g}/\text{mL}$ fibronectin solution (Sigma-Aldrich) in iPSC-EC complete growth media was added to the outlet port of the center lumens and PDMS rods was pulled out from the inlet or outlet ports with a fine-tip tweezer, leaving behind a fluid-filled lumen within the ECM gel. The fibronectin solution in the center lumens was then incubated at 37°C for 20 min. Following incubation, the fibronectin solution was aspirated out of the center lumens prior to iPSC-EC seeding. iPSC-ECs were trypsinized with 0.05% Trypsin-EDTA (25300062, Thermo Fisher, Waltham, Massachusetts), suspended in iPSC-EC complete growth media and seeded into the outlet ports of the center lumens at 15,000 cells/ μL . The MatTek dish with the bonded devices were then incubated at 37°C and flipped (upside-down then right-side-up) every 30 min. After 2 hours of flipping and incubation, unadhered cells were aspirated out and the center lumen was filled with fresh media. Media was replaced every 24 h for two days before coating the center lumen with BCCs for direct contact co-

culture or side lumen for indirect co-culture. All cultures were maintained in a humidified incubator at 37°C with 5% CO₂.

3.2.5 Direct Contact and Indirect Co-Culture of BCCs

For direct contact co-culture, BCCs (i.e., MDA-MB-231, MCF-7 and Hs-578T cells) were trypsinized, resuspended in iPSC-EC complete growth media at 1800 cells/μL and loaded into the center or side lumen (2μL per lumen) via passive pumping. For co-culture involving paracrine signaling alone (indirect co-culture), BCCs were seeded into a lumen adjacent to the iPSC-EC vessel. The MatTek dishes were then flipped and incubated, as described before, to coat the lumens with BCCs. Unadhered cells were flushed and replaced with 30 μL of iPSC-EC complete growth media. Media was replaced every 24 h for the entire duration of culture.

3.2.6 Blocking and Neutralization

Anti-IL-6R mAb, Tocilizumab, (Actemra, Genentech/Roche, South San Francisco, CA), allosteric inhibitor of chemokine receptors 1 and 2 (CXCR1/2) or IL-8R, Reparixin (Cayman Chemical, Ann Arbor, MI, USA) and MMP-3 inhibitor, UK-356618 (Santa Cruz Biotechnology, Dallas, TX) were used for IL-6R, IL-8R and MMP-3 inhibition experiments. Dosing was determined by independent and combined treatment of iPSC-ECs cultured in a 96-well plate with tocilizumab, reparixin and UK-356618 at varying concentrations. Concurrently, a control set of iPSC-EC wells were treated with the vehicle (DMSO), **Figure A.7**. To inhibit IL-6, IL-8 and MMP-3 signaling in our system, MDA-MB-231 cells were co-cultured (direct contact) with iPSC-EC vessels for 2 h

followed by independent or combined treatment with media containing tocilizumab (100 µg/mL), reparixin (10 µM), UK-356618 (0.3 µM) and vehicle control. After 24 h of treatment, media were collected for cytokine secretion analysis, and vessels were used for quantifying extravasation events and dextran diffusion analysis.

3.2.7 Cytokine Quantification

Cytokine secretion analysis was performed on media collected from monocultures and co-cultures of iPSC-EC vessels and three different BCC types on day 4. For conditioned media experiments, conditioned media collected from monoculture systems after 48 h were diluted with iPSC-EC complete growth media (50:50) and subsequently added to separate monocultures of iPSC-EC vessels or MDA-MB-231 cells. Media were then collected from conditioned media treated systems after 48 h for analysis. For therapeutic inhibition experiments, media were collected from treated or vehicle control systems after 24 h. 25 µL of maintenance media were obtained in all cases from 4 separate systems on the final day of culture and pooled to generate one biological replicate. Four biological replicates were performed over three separate experiments. A custom selection of analytes (Angiopoietin-2, ANGPTL4, HB-EGF, IL-6, IL-8, MCP-1, MMP-1, MMP-3 and VEGF-C) from an oncology multiplex assay panel (R&D Systems, Minneapolis, MN) were selected for this analysis. Sample preparation was performed as per manufacturer's protocol and measured using MAGPIX Luminex Xmap (Luminex Corporation, Austin, Texas). Luminex xPonent software was used for data collection.

3.2.8 Immunofluorescence Staining

For immunostaining, lumens were fixed with 4% (v/v) paraformaldehyde (Alfa Aesar, Haverhill, MA) for 20 min and permeabilized with 0.2% (v/v) Triton-X 100 (MP Biomedicals, Santa Ana, CA) for 30 min at room temperature. To reduce non-specific background fluorescence from collagen, systems were incubated in 0.1 M glycine (Fisher Scientific, Pittsburgh, PA) for 30 min. Systems were washed with sterile PBS between each step. Cells were then blocked with 3% (wt/v) BSA (Sigma-Aldrich, St. Louis, MO) and 0.1% (v/v) Tween-20 (Fisher Scientific, Pittsburgh, PA) overnight at 4 °C. For antibody-based staining, primary antibodies diluted at desired concentrations (**Table A.1**) were added to the devices and incubated at 4 °C overnight. Excess primary antibodies were removed by washing the devices multiple times. Secondary antibodies diluted at 1:100 along with Hoechst 33342 (Thermo Fisher, Waltham, Massachusetts) in blocking-buffer were added to the devices and incubated for at 4 °C overnight. Stained vessels were washed multiple times with sterile PBS over a period of 24 h prior to imaging. For live cell imaging of endothelial vessels, iPSC-ECs were stained in red with the fluorescent lipid Dil (V22889, Thermo Fisher) in iPSC-EC complete growth media for 10 min prior to cell seeding within lumen.

3.2.9 Image Acquisition

Fluorescent images used to analyze extravasation events and vessel permeability were acquired using a Nikon TI Eclipse inverted microscope (Melville, NY) and analyzed using the National Institutes of Health ImageJ software. Confocal images were acquired

at University of Wisconsin-Madison Optical Imaging Core using a Nikon A1RS confocal microscope (Melville, NY).

3.2.10 Image Analysis (Extravasation events, ICAM-1 expression, and Col IV deposition)

Extravasation events were measured by capturing images across the z-plane of the lumen at 6x magnification. Images were processed using ImageJ software where z-plane images were maximally projected to create a 2D image. A smoothing filter and background subtraction was used. Extravasated cells were those present outside of the lumen-edge. GFP-expression and nuclear stain were used to count the number of extravasated cells. To characterize ICAM-1 expression and Col IV deposition confocal images were analyzed using ImageJ software. Briefly, raw images were prepared by enhancing contrast and removing noise. Same thresholding parameters and area of region of interest were applied to all images compared. From 2D projected, binarized images intensity profiles or mean intensities were obtained. Sequences of instructions for calculating mean intensities of ICAM-1 expression and expression profiles of Col IV deposition are shown in Appendix section **Figure A.2 and A.3**.

3.2.11 Statistical Analysis

GraphPad Prism 7 (GraphPad Software, La Jolla, CA) was used for statistical analysis. One-way ANOVA with Tukey post hoc test for pairwise comparison was used for significance testing on three or more datasets. Non-paired student's t-test was performed for determining statistical significance between two conditions. Tests were

considered significant for $p \leq 0.05$. The number of replicates ranged from $n = 4$ to $n = 6$ for each experimental condition.

3.3 Results

3.3.1 Organotypic Breast Cancer Cell Extravasation Model

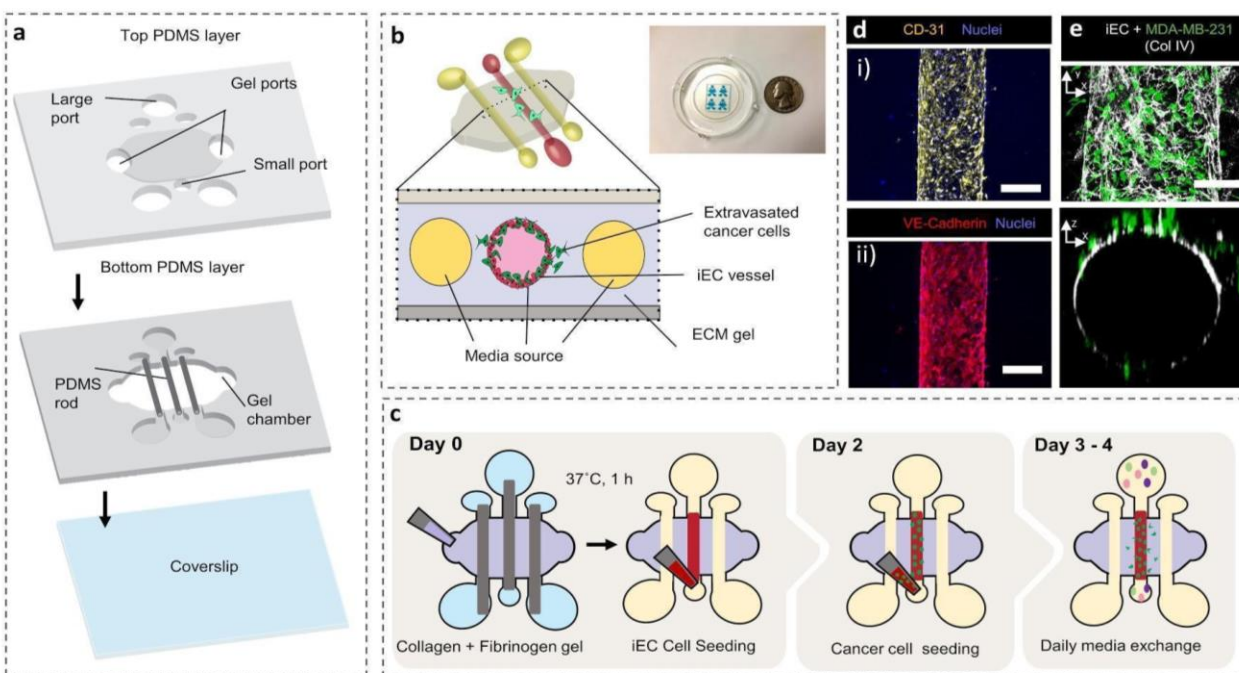


Figure 3.1 3D organotypic breast cancer extravasation model and setup. (A) Schematic representation of device layers and assembly. The top layer forms the cover of the devices and consists of features that make up the extracellular matrix gel (ECM) gel chamber and ports for fluid handling / cell seeding. The bottom layer consists of features making up the bottom-half of the ECM gel chamber and channels that support three lumen rods suspended across the gel chamber. The assembled layers are plasma-bonded to a glass coverslip. (B) Schematic isometric and vertical section view of the breast cancer extravasation model that mimics the structure of blood vessels surrounded by ECM. Top inset shows a photograph of the assembled microfluidic device. (C) Experimental setup and cell seeding configuration of the proposed model including breast cancer cells extravasating through an endothelial vessel. (D) Confocal image center lumen lined with induced pluripotent stem cell-derived endothelial cells (iPSC-ECs) that form a patent vasculature as characterized by expression of endothelial marker CD31 (i) and VE-cadherin (ii), scale bar indicates 150 μm . (E) Confocal image of human breast cancer cell line MDA-MB-231 extravasating across iPSC-EC vessels and collagen IV (top inset) deposited by iPSC-ECs. Cross-sectional 3D reconstruction of type IV collagen (Col IV) deposition with extravasated MDA-MB-231 cells (bottom inset), scale bar indicates 100 μm .

We engineered a microscale organotypic *in vitro* model that allows the study of cancer cell extravasation. The device consists of two thin PDMS layers with patterned microscale features bonded to a coverslip glass, **Figure 3.1A**. To generate lumen structures, three PDMS rods are embedded between the PDMS layers of the device. This method enables robust control over vasculature size, number, configuration and allows for fabrication of arrayed devices for assaying multiple conditions in parallel. The lumens can be lined with ECs to model blood vessels. Cancer cells can be introduced to the EC lined lumen and co-cultured to investigate extravasation behavior, **Figure 3.1B**.

To generate EC lined lumen structures, we used a gel consisting of 3 mg/mL type I collagen and 1 mg/mL fibrinogen, **Figure 3.1C**. iPSC-ECs line the center lumen of the device while the side lumens are used as additional media source to feed all cell types within the system. Within 48 hours of culture, iPSC-ECs form a continuous monolayer with a hollow lumen, similar to *in vivo* vasculature. The separate inlet and outlet ports of each lumen in the device are used for cell seeding and media exchange. *In vivo*, ECs form monolayer barriers that regulate the passage of fluids, compounds and cells via the use of cell-cell junction proteins¹⁰². In our model, iPSC-ECs expressed endothelial cell marker CD31 and junctional marker VE-cadherin, which were localized to the periphery of endothelial cell-cell contacts, indicating the presence of adherens junctions, **Figure 3.1D**. The establishment of a continuous monolayer resulted in the deposition of COL IV, a major component of the basement membrane.

To study cancer cell extravasation, human BCCs were seeded into the iPSC-EC-lined lumen through the pipette-accessible ports. The direct-contact co-culture of cancer cells on the endothelium mimics cancer cell-EC interactions, in larger vessels, after adhesion but prior to transendothelial migration. Following direct-contact co-culture within our model, MDA-MB-231 cells were found to be both adhered to the inner surface of the endothelial lumen and in the matrix space surrounding the vessel. 3D reconstruction of vessel cross-section showed extravasated MDA-MB-231 cells outside of the iPSC-EC lumen, **Figure 3.1E**. The ability to visualize co-localization of invasive BCCs during extravasation enables the study of cancer cell-mediated modulation of the endothelium.

3.3.2 BCCs Modulate Endothelial Properties and Basement Membrane

Components

To study BCC extravasation, we seeded MDA-MB-231 cells at a density high enough to observe at least one extravasation event within 24 hours of co-culture. Following, cell seeding, MDA-MB-231 cells appeared to extravasate out of iPSC-EC vessels within 8 hours, **Figure 3.2A**. Fluorescent microscopy images demonstrate the capability of our system to capture morphological dynamics of cancer-vascular interactions and single-cell extravasation events in high detail. Following co-culture, MDA-MB-231 cells appeared to take on spherical and elongated shapes both within the vasculature and in the matrix. Cells can be seen adhered to the inner surface of the lumen vasculature, partially protruding outside of the lumen barrier into the matrix, and fully transmigrated into the matrix, **Figure 3.2B**. Confocal microscopy also revealed exchange of membrane components between ECs and BCCs. Fragments of iPSC-EC membranes,

labeled with a lipophilic membrane stain, were observed within GFP expressing MDA-MB-231 cells during direct-contact co-culture, suggesting intercellular crosstalk, **Figure A.4.**

Cancer cells are known to prime the endothelium and facilitate their own transmigration across the endothelial barrier¹⁰. Attachment of cancer cells to the endothelium is mediated by adhesion molecules, which are absent or minimally expressed in unactivated endothelium^{10,103}. To investigate the effects of BCCs on EC modification, we assessed the expression of ICAM-1 on the vasculature in response to co-culture with MDA-MB-231 cells, **Figure A.5**. Recent reports show that BCC lines express ICAM-1, and it is relatively overexpressed in triple-negative BCC lines including MDA-MB-231 cells¹⁰⁴. To assess crosstalk-associated upregulation of ICAM-1 on the endothelium alone without addition of ICAM-1 signals from cancer cells, we examined ICAM-1 expression on iPSC-EC vessels in response to soluble factor signaling, **Figure 3.2C i-ii**. To achieve this, MDA-MB-231 cells were co-cultured in an adjacent lumen to the iPSC-EC lumen to determine their effect on ICAM-1 expression via secreted factor signaling. Mean fluorescence intensity values of ICAM-1 staining on iPSC-EC vessels increased in response to paracrine signaling from MDA-MB-231 cells relative to control monoculture conditions, **Figure 3.2C iii**. Details of intensity profile analysis can be found in **Figure A.2**. This result indicates that BCC secreted factors precondition the endothelium, increasing the expression of cancer associated adhesion molecules.

Modification of the iPSC-EC derived basement membrane by extravasating BCCs was also observed. COL IV is the most abundant component of basement membranes

making up 50% of basement membrane composition^{105,106}. Confocal microscopy showed COL IV deposition by ECs in our device, **Figure 3.2D i**, which were consistent with previously reported basement membrane distributions of vascular tissues¹⁰⁷. Following extravasation of MDA-MB-231 cells, large areas devoid of COL IV were observed surrounding the endothelium, **Figure 3.2D ii-iii**. Intensity profile analysis of COL IV deposition across iPSC-EC vessels exhibited an overall decrease in COL IV expression resulting from direct-contact co-culture with MDA-MB-231. Moreover, intensity profiles showed an intensity decrease (**Figure 3.2D iv, purple arrow**) at the position of interaction/overlap between MDA-MB-231 cells and the endothelium. Interestingly, our results suggest more COL IV remodeling and degradation resulting from direct-contact interactions between ECs and BCCs compared to paracrine mode signaling **Figure A.6**. COL IV intensity analysis showed similar COL IV deposition by iPSC-EC vessels in monoculture as in co-culture with paracrine mode signaling alone. These results suggest that physical interactions with the vasculature have more of an effect on COL IV remodeling by MDA-MB-231 cells than by the actions of paracrine crosstalk. Details on quantification of COL IV deposition and intensity profile analysis are listed in **Figure A.2-3**. Together, these results provide evidence of crosstalk leading to paracrine signaling-mediated modulation of endothelial properties, and physical remodeling of basement membrane by extravasating cancer cells within our model.

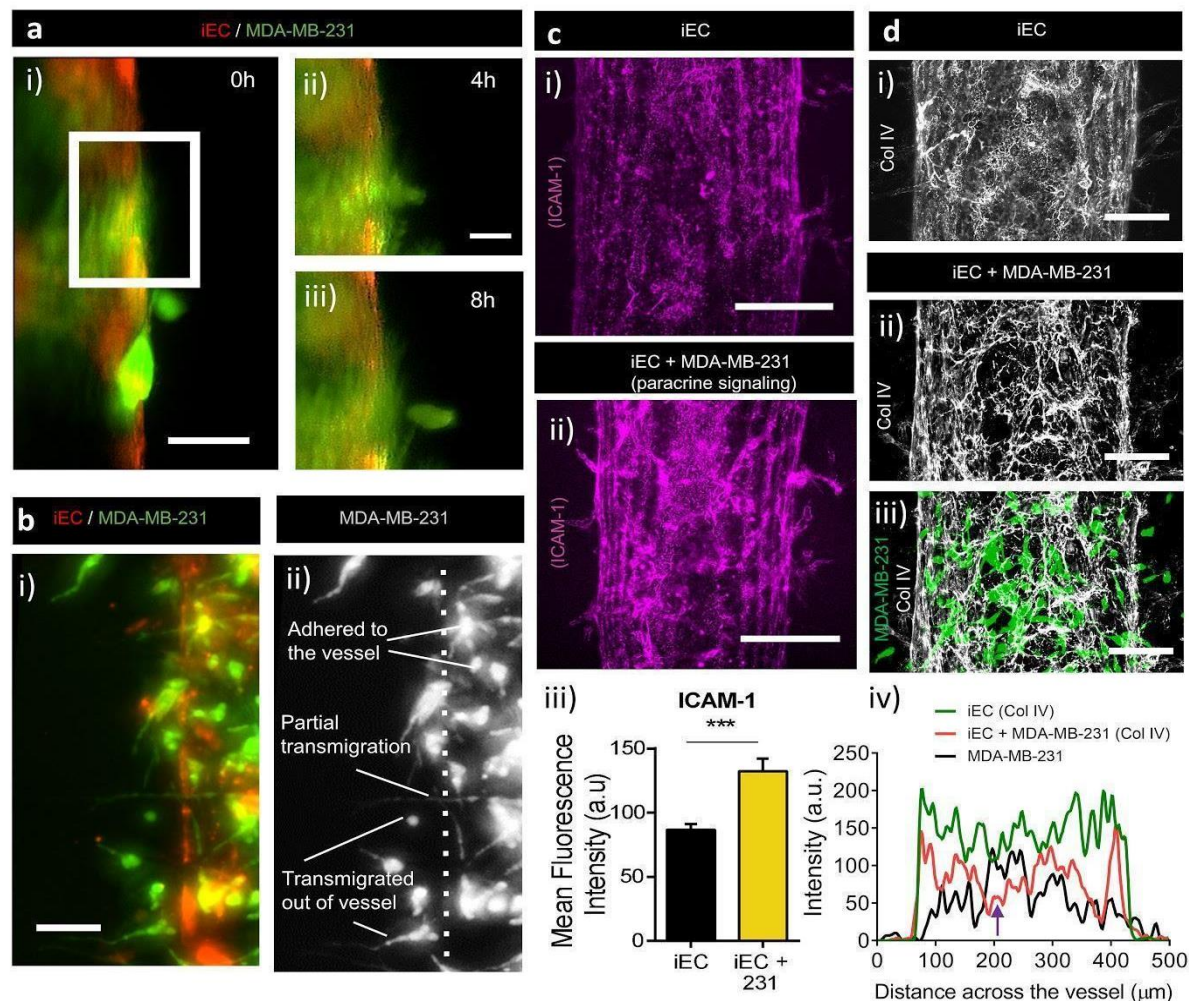


Figure 3.2 Breast cancer cell extravasation behavior and cancer-vascular interactions. (A) Fluorescent images of MDA-MB-231 cells extravasating out of iPSC-EC vessels within 8h of co-culture, scale bar indicates 50 μm . Protrusions of MDA-MB-231 cells across the iPSC-EC endothelium at 4h (i) and 8h (ii), scale bar indicate 20 μm . (B) MDA-MB-231 cancer cells (i) take on variety of morphologies during extravasation out of an iPSC-EC vessel, including adhesion to the internal surfaces of the vessel, partial transmigration and fully transmigrated out of vessels (ii), scale bar indicates 50 μm . (C) Confocal images of ICAM-1 expression on iPSC-EC vessels (i) and on iPSC-EC vessels in co-culture with MDA-MB-231 cells in an adjacent lumen (ii). Image intensity analysis of ICAM-1 expression on iPSC-EC vessels alone and in co-culture with MDA-MB-231 cells (iii), scale bar indicates 150 μm . (D) Type IV collagen (Col IV) deposition by iPSC-EC vessel alone (i) and after MDA-MB-231 extravasation (ii-iii), scale bar indicates 100 μm . Image intensity analysis of Col IV deposition by iPSC-EC vessels in monoculture and after MDA-MB-231 cells extravasation (iv).

3.3.3 Secreted Factor Analysis Reveals Distinct Profiles for Highly And Poorly Invasive BCCs

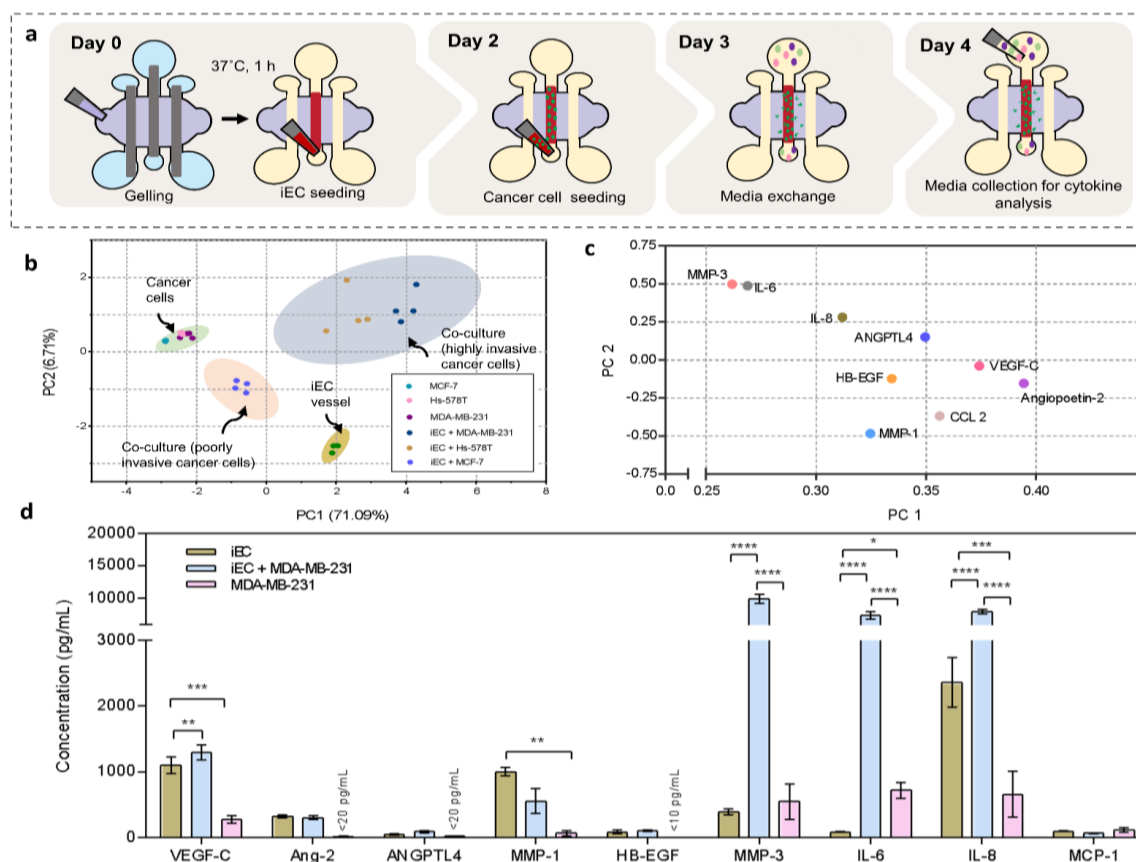


Figure 3.3 Protein secretion profiles iPSC-EC vessels and breast cancer cell cultured within the proposed model. (A) Schematic representation of breast cancer extravasation model setup and cell culture supernatant collection for a multiplexed enzyme-linked immunosorbent (MagPIX) assay. (B) Principal component analysis (PCA) is used to project protein secretion data sets of iPSC-EC vessel and breast cancer cells in monoculture and co-culture onto the first two components, PC 1(71.09%) and PC 2 (6.7%). Each dot represents one of four independent cultures per condition and the shaded ellipses represent 95% confidence intervals. PCA variance refers to amount of total variance observed between samples of conditions that segregate along that principal component. (C) PCA loadings plot on PC 1 and PC 2 are plotted for individual factors used for PCA scores plot in (b). (D) Cytokine concentrations measured in media collected from iPSC-EC vessels cultured alone, iPSC-EC vessels with extravasating MDA-MB-231 cells and MDA-MB-231 cells cultured alone. Plot: mean concentrations + SD, statistical analysis: ordinary one-way ANOVA with Tukey's multiple comparisons test, brackets denote comparisons between conditions that are statistically significant, **** $p \leq 0.0001$, *** $p \leq 0.001$, ** $p \leq 0.01$ and * $p \leq 0.05$ ($n=4$).

During extravasation, to cross structural barriers of blood vessels, BCCs secrete mediators that increase vascular permeability and enhance their own ability to undergo transendothelial migration⁸⁵. To investigate paracrine signaling between cancer cells and the endothelium, we examined secretion profiles of highly invasive (MDA-MB-231 and Hs-578T cells) and poorly invasive (MCF-7 cells) BCCs in monoculture and in co-culture with iPSC-EC vessels. Media were collected from the cell seeding ports on day-4 of culture and analyzed for protein secretion. For monoculture conditions, iPSC-EC vessels or BBCs were cultured within our system for 4 days prior to media collection. Whereas for co-culture conditions, iPSC-ECs were maintained for 2 days followed by BCC seeding, which were maintained for 2 additional days for a total of 4 days, **Figure 3.3A**. A custom selection of analytes (Angiopoietin-2, ANGPTL4, HB-EGF, IL-6, IL-8, MCP-1, MMP-1, MMP-3 and VEGF-C) were selected for this analysis based on their involvement in extravasation and breast cancer metastasis.

Principal component analysis (PCA) of protein secretion was performed to identify variations in secretion profiles based on cell types and culture conditions, **Figure 3.3B**. Principal components (PCs) 1 and 2 captured 77.8% of the total variation in the data set and the score plot of the PC1-PC2 comparison revealed four distinct groups of culture conditions. Co-culture conditions (blue and red shaded regions) and monoculture conditions (green and yellow shaded regions) formed separate clusters, demonstrating distinct secretion profiles within our system. The largest variance along principal component one (71.09%) was observed between invasive cell lines in co-culture with iPSC-EC vessels and in monoculture. This indicates a strong impact on the overall

secretion profiles resulting from BCC/iPSC-EC crosstalk involving invasive subtypes of BCCs. Notably, co-culture involving invasive cell lines (blue) were separately clustered from co-culture involving poorly invasive lines (red). Secretion of all BCC monocultures (green) clustered together while iPSC-EC vessels (yellow) secretion was clustered separately. These results show that using this protein secretion analysis we can delineate secretion of iPSC-EC vessels from BCCs cultured within our system and, moreover, that crosstalk between iPSC-ECs and BCCs yield distinct secretion profiles based on BCC subtypes (i.e., highly- invasive vs. poorly invasive).

To identify specific secreted factors contributing to the variances observed between culture conditions in the score plot, a loadings plot was generated along PC1 and PC2 **Figure 3.3C**. The loadings of all analytes examined positively correlated along PC 1, which corresponds to secretions of iPSC-EC vessels in monoculture and in co-culture with invasive cancer lines. According to the loadings plot factors such as VEGF-C, Angiopoietin-2 and CCL-2 are enriched in culture conditions involving iPSC-EC vessels. As iPSC-EC vessels in monoculture and co-culture cluster separately along PC2, we can determine factors that are enriched because of co-culture by interpreting the corresponding loadings plot. Accordingly, ANGPTL4, MMP-3, IL-6 and IL-8 correlate with co-culture of iPSC-EC vessels with invasive BCC lines, suggesting that these factors are upregulated because of their interactions. This is further illustrated in the protein concentration plots of iPSC-EC vessel and MDA-MB-231 cell monoculture and their co-culture, **Figure 3.3D**, where concentrations of IL-6, IL-8 and MMP-3 are significantly upregulated in the co-culture condition. Interestingly, these factors were not

significantly upregulated in cultures involving poorly invasive BCCs and iPSC-EC vessels suggesting a correlation between the specific roles of these factors and the invasive phenotype of BCCs.

3.3.4 Tumor and Endothelial Derived Factors Involved In Cancer-Vascular

Crosstalk

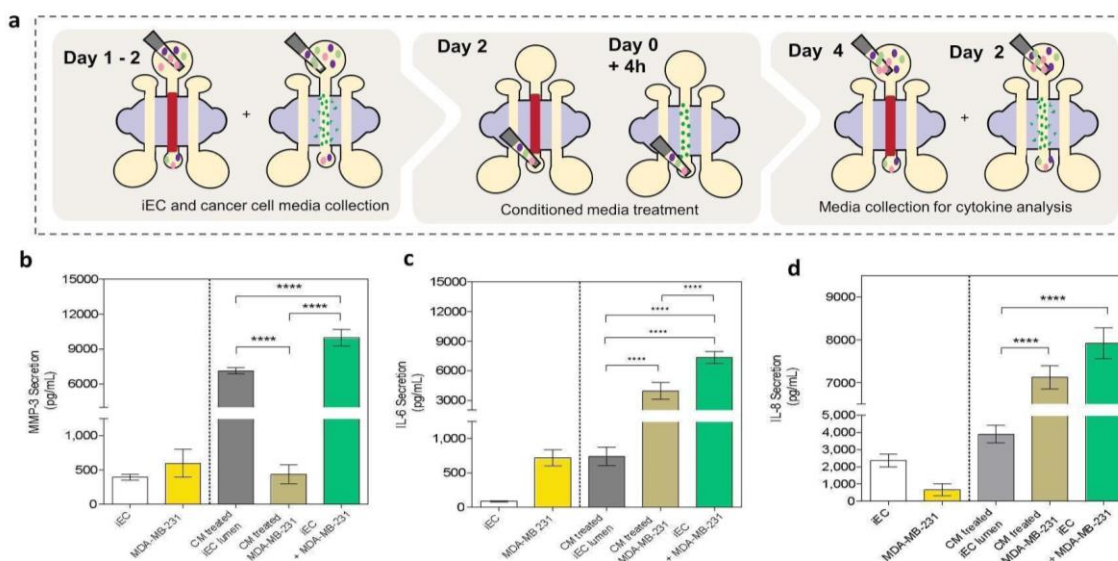


Figure 3.4 Cancer-endothelial crosstalk via soluble factor signaling. (A) Schematic representation of conditioned media experiments and cell culture supernatant collection for MAGPIX assay. (B – D) Secreted factor (MMP-3, IL-6 and IL-8) concentrations measured in media collected from iPSC-EC vessels cultured alone, iPSC-EC vessels cultured in MDA-MB-231 conditioned media, MDA-MB-231 cells, MDA-MB-231 cells cultured in iPSC-EC vessel conditioned media, and direct-contact co-culture of iPSC-EC vessels and MDA-MB-231 cells cultured in the device. Plot: mean concentrations + SD, statistical analysis: ordinary one-way ANOVA with Tukey's multiple comparisons test, brackets denote comparisons between conditions that are statistically significant, **** $p \leq 0.0001$ ($n=4$).

Our initial data showed that IL-6, MMP3 and IL-8 are increased during co-culture of iPSC-EC vessels and MDA-MB-231 cells, compared to the sum of their monoculture contributions. Here, investigate the individual roles of iPSC-EC vessels and invasive

BCCs in the upregulation of secreted IL-6, IL-8, and MMP-3 by performing conditioned media experiments. To eliminate the influence of culture methods on secreted factor signaling, we extracted cell-conditioned media from iPSC-EC vessels and BCCs cultured within our model. Given that the largest variance in the PCA analysis was observed between monoculture and co-culture of MDA-MB-231 cells with iPSC-ECs, we chose MDA-MB-231 cells as a representative cell line in subsequent experiments. Protein secretion levels were measured in the following five conditions: iPSC-EC vessels cultured alone, iPSC-EC vessels cultured in MDA-MB-231 conditioned media, MDA-MB-231 cells cultured alone, MDA-MB-231 cells cultured in iPSC-EC vessel conditioned media and direct-contact co-culture of iPSC-EC vessels with MDA-MB-231 cells, **Figure 3.4A**. Our analysis revealed that MMP-3 secretion was significantly increased not only when iPSC-ECs were exposed to direct-contact co-culture with MDA-MB-231, but also with MDA-MB-231 conditioned media, suggesting this increase is driven by an MDA-MB-231 soluble factor, **Figure 3.4B**. Conversely, IL-6 and IL-8 were upregulated significantly in direct-contact co-culture, and also in MDA-MB-231 cell culture with iPSC-EC conditioned media. This suggests that upregulation of these secreted factors may be contributed primarily by MDA-MB-231 cells in response to signaling from iPSC-EC vessels, **Figure 3.4C-D**. Together, these results show that MDA-MB-231 cells secrete high levels of IL-6 and IL-8 in the presence of iPSC-EC vasculature while iPSC-EC vasculatures upregulate MMP-3 secretions in the presence of MDA-MB-231 cells.

3.3.5 Cancer-Vascular Paracrine Signaling Leads to Impaired Vascular Barrier Function

Function

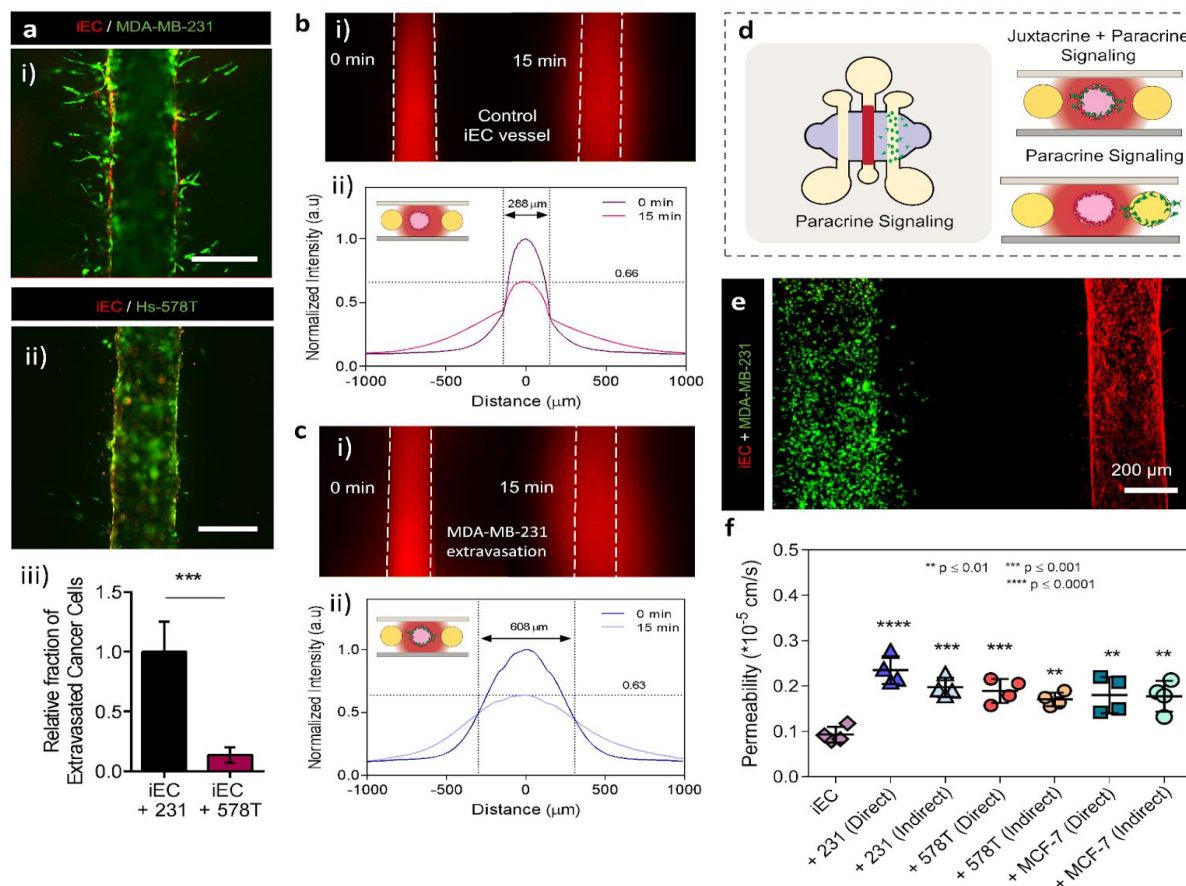


Figure 3.5 Impact of breast cancer cell extravasation on iPSC-EC vascular permeability. (A) Fluorescent images of invasive breast cancer cells MDA-MB-231(i) and Hs-578Ts (ii) extravasating out of iPSC-EC vessels, scale bar indicates 250 μm . (iii) Relative fraction of extravasation events for invasive breast cancer cell types of Hs-578Ts and MDA-MB-231. Plot: Relative fraction of extravasated cells + SD, statistical analysis: Student-test, *** $p \leq 0.001$, ($n=4$). (B-C) iPSC-EC vessel barrier function. Fluorescent images of 70 kDa dextran diffusion across iPSC-EC vessels over a 15 min period (Bi) and across iPSC-EC vessels with extravasated MDA-MB-231 cells (Ci). Normalized intensity profiles of 70 kDa dextran diffusion across iPSC-EC vessels where the peak intensity has decreased to 66% (bii) of the maximum intensity value with a profile width of 288 μm for iPSC-EC vessels and 63% with profile with of 608 μm with extravasation. (D) Schematic representation of device setup for assessing paracrine signaling between cancer cells and the endothelium. (E) Fluorescent images of MDA-MB-231 cells co-cultured with iPSC-EC vessel in an adjacent lumen relative to vessel. (F) The graph shows permeability coefficients of iPSC-EC vessels in co-culture with three different breast cancer cell subtypes (MDA-MB-231, HS-578T and MCF-7) in two different culture conditions (direct contact and indirect co-culture). Plot: mean permeability + SD, statistical analysis: Student-test, **** $p \leq 0.0001$, *** $p \leq 0.001$ ($n=4$).

Taking advantage of the capacity of our model to visualize cancer-vascular interactions, we examined extravasation behavior of three different BCCs (MDA-MB-231, Hs-578T and MCF-7) by analyzing events of extravasation and vascular permeability using confocal microscopy. While the invasive cell lines MDA-MB-231 and Hs-578T both migrated out of the vasculature, **Figure 3.5 Ai-ii**, MCF7 cells formed cell aggregates and remained within the lumen vasculature, **Figure A.7**. Among the invasive cell lines, MDA-MB-231 cells exhibited significantly higher extravasation efficiency compared to Hs-578T cells, **Figure 3.5 Aiii**, which is consistent with previous reports¹⁰⁸. These observations also correlate with higher levels of secreted IL-6, IL-8 and MMP-3 resulting from the crosstalk between iPSC-EC vasculature and invasive BCC lines, as observed in our secreted factor analysis. We also assessed the influence of direct-contact co-culture with BCCs on the barrier function of iPSC-EC vasculatures. To establish baseline barrier function of iPSC-EC vessels, we measured vascular permeability using methods previously described¹⁰⁹. Upon formation of a complete endothelialized lumen, the diffusive permeability of fluorescently tagged 70 kDa dextran were analyzed and compared to an empty lumen structure without an endothelium, **Figure A.8**. The endothelialized lumen exhibited lower diffusive permeability values compared to a lumen control without ECs, indicating the presence of barrier function. We then examined changes in diffusive permeability of iPSC-EC vessels resulting from co-culture with BCCs of different invasive profiles. iPSC-EC vessels in direct-contact co-culture with MDA-MB-231, Hs-578T and MCF-7 cells were filled with fluorescently tagged 70 kDa dextran solutions and imaged over a 15 min period, **Figure 3.5 Bi**. Intensity profiles of dextran diffusion across vessels were plotted and analyzed to

compare vascular permeability between monoculture and co-culture conditions, **Figure 3.5 Bii**. The diffusion profiles for iPSC-EC vessels in co-culture with MDA-MB-231 cells were broader compared to iPSC-EC vessels in monoculture, **Figure 3.5 Ci-ii**. Interestingly, despite the absence of extravasation events, co-culture of MCF-7 with iPSC-EC vessels resulted in broad diffusion profiles, similar to those obtained from the invasive cell lines (**Figure A.7**), indicative of higher permeability. Endothelial viability was confirmed to exclude EC death as a possible cause of this observation.

To further differentiate contributions of direct-contact cancer-vascular cell interactions, involving both juxtacrine and paracrine signaling, from paracrine signaling on vascular barrier function, we investigated the impact of co-culture using two distinct setups (i.e., direct-contact and indirect-contact co-culture). For direct-contact interactions, BCCs were injected into the EC-coated lumen, while for indirect-contact interactions (paracrine signaling only), BCCs were seeded in an empty lumen adjacent to an EC-coated lumen **Figure 3.5 D-E**. Vascular permeability in direct-contact and indirect-contact co-cultures were analyzed. Overall, dextran permeability in co-culture with BCCs were significantly greater than monoculture condition, **Figure 3.5 F**. Among the invasive lines (i.e., MDA-MB-231 and Hs-578T), direct-contact signaling induced a slightly higher vascular permeability compared to paracrine signaling alone. For MDA-MB-231 cells, direct-contact signaling lead to a 2.5-fold increase compared to 2.1-fold increase in paracrine signaling mode against monoculture vessels. Similarly for Hs-578T cells, there was a 2-fold increase in direct-contact mode signaling versus a 1.8-fold increase for paracrine

signaling. Conversely, no differences in permeabilities were observed between direct-contact and indirect-contact co-culture for poorly invasive cells (i.e., MCF-7 cells).

Although there were no substantial differences in barrier impairment of iPSC-EC vasculatures for invasive and poorly invasive cancer cell lines, secreted factor analysis revealed altered secretion of factors associated with increased vascular permeability, such as IL-6, **Figure 3.3 C**. A slight difference in the degree of barrier impairment between MDA-MB-231 cells and MCF-7 cells was observed for the direct-contact co-culture conditions. Co-culture with MDA-MB-231 cells induced a higher increase (2.5-fold) compared to MCF-7 cells (1.9-fold) in vascular permeability against monoculture controls. Interestingly, paracrine signaling interactions lead to a similar increase in vascular permeability for MCF-7 cells as the other invasive lines. This combined with our secreted factors analysis, which revealed distinct protein secretion profiles for invasive BCC lines compared to poorly invasive cell lines in co-culture with iPSC-EC vasculatures, suggest a different conditioning capability of MCF-7 that is contributing to this vascular impairment. Taken together, these observations suggest that to facilitate cancer cell extravasation, paracrine signaling alone can significantly contribute to impairing the barrier function of vasculatures. In addition, direct-contact interactions and subsequent events of extravasation further exacerbates this effect.

3.3.6 Therapeutic Inhibition of IL-6, IL-8 and MMP-3 Reduces Overall Secretion of Factors Associated with Breast Cancer Metastasis

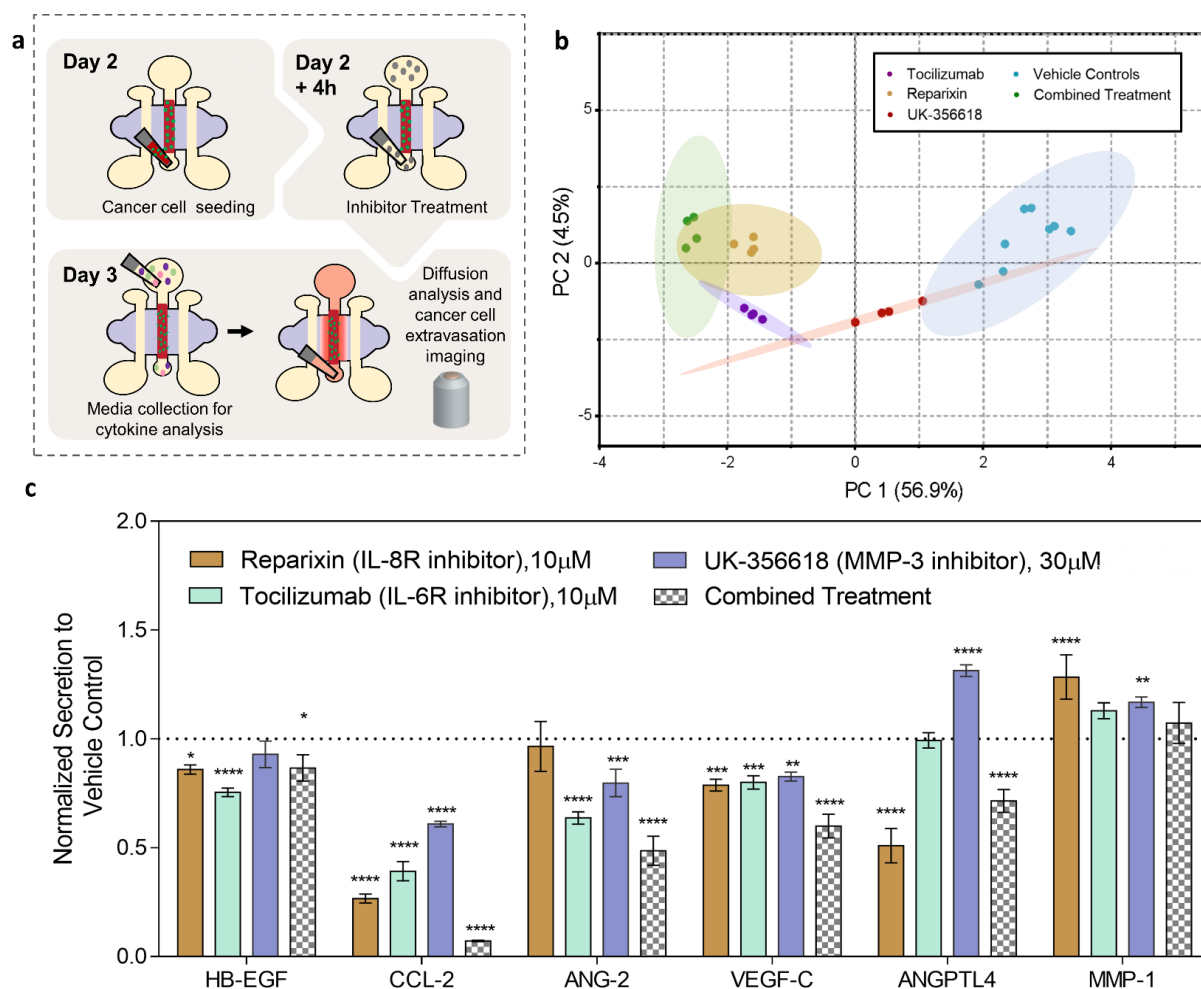


Figure 3.6 Protein secretion profiles of the breast cancer extravasation model with and with treatment of independent and combined therapeutic inhibitors. (A) Schematic representation of experimental workflow for molecular (MAGPIX) and functional (barrier function and quantification of extravasation events) assays. (B) PCA scores plots of secretion data sets from systems treated with therapeutic inhibitors both independently (Reparixin, Tocilizumab and MMP-3 inhibitor) and in combination (Reparixin+Tocilizumab+MMP-3 inhibitor) and treated with vehicle controls onto the first two components, PC 1(56.9%) and PC 2(4.5%). Each dot represents one of four independent cultures per condition and the shaded ellipses represent 95% confidence intervals. (C) Normalized cytokine concentrations measured in media collected from systems independently treated and in combination with therapeutic inhibitors relative to vehicle controls. Plot: fraction of vehicle control concentration + SD, statistical analysis: ordinary one-way ANOVA with Tukey's multiple comparisons test, brackets denote comparisons between conditions that are statistically significant, **** $p \leq 0.0001$, *** $p \leq 0.001$, ** $p \leq 0.01$, * $p \leq 0.05$ (n=4).

Our secretion profile analysis suggested a correlation between IL-6, IL-8, and MMP-3 secretion- and the metastatic potential of BCCs. Moreover, we found a significant impact of paracrine signaling on the functional behavior of iPSC-EC vasculatures. Considering these findings, we hypothesized that impaired vascular function and extravasation events can be mitigated by inhibiting the IL-6, IL-8 and MMP-3 paracrine signaling. Thus, we set out to explore the influence of these factors on the functional behavior of BCCs and iPSC-EC vasculatures by using therapeutic inhibitors. MDA-MB-231 cells were used as a representative invasive breast cancer line as they were revealed to be most invasive in our investigation. To inhibit IL-6 and IL-8 signaling, we used clinically active therapeutics tocilizumab, an anti-IL-6R mAb, and reparixin, an allosteric inhibitor of IL8R1/CXCR1 and IL8R2/CXCR2. For MMP-3 inhibition, we used an MMP-3 selective inhibitor, UK-356618. The chosen doses of therapeutic inhibitors were selected based on previous reports that demonstrated reduced cancer cell viability and migration either in monoculture or co-culture with other cell types. Specifically, tocilizumab has been shown to reduce viability of MDA-MB-231 cells to 40% and migration to 60% at 1.37 μ M in co-culture with lymphatic endothelial cells¹¹⁰. In another study, reparixin was found to significantly reduce MDA-MB-231 cell migration in 3D matrix at concentrations of 14 μ M or higher¹¹¹. UK-356618-mediated inhibition of cell migration has been demonstrated in lung cancer cells at 0.07 μ M concentrations¹¹². Concentrations in these studies were used to inform and set dosing ranges for the study presented in this work. Prior to evaluating the effect of these inhibitors on BCC extravasation, we tested their potential effect on endothelial cell viability. Viability analysis of iPSC-ECs was conducted to ensure the selected doses, while affecting

cancer cells, do not adversely influence viability and functionality of the endothelium. Briefly, iPSC-ECs were cultured in 96-well plates and treated with varying drug concentrations over a 24-hour period. For extravasation experiments, inhibitor dose was selected at >90% viability of iPSC-ECs. In this context, reparixin, tocilizumab, and UK-356618 decreased cell viability below 90% at concentrations above 500 µg/mL, 50 µM and 6 µM respectively, thus we used dosing below these concentrations (**Figure A.9**).

In extravasation inhibition experiments, iPSC-EC vessels were cultured for 48 h prior to MDA-MB-231 cell seeding within the vessel, **Figure 3.6A**. BCCs were added to the lumens, cultured for 2 h followed by 24-hours of single-drug or combined treatment with tocilizumab, reparixin and UK-356618. First, we examined if these treatments had off-target effects on the secretion of the other extravasation and metastasis-associated molecules previously inspected. Protein secretions of treated and control systems were analyzed after 24-hours of co-culture. PCA analysis of secreted proteins showed that the highest variance along PC1 which generates an axis between combined treatment and vehicle control systems. This indicates that combined treatment decreased overall secretions to a greater extent than anything other single treatment conditions. It should be noted that clustering analysis also revealed some overlap between systems independently treated with tocilizumab or reparixin and systems receiving combined treatment, suggesting a similar decrease in secretions (**Figure 3.6B**). Further investigation of normalized secretion levels indicates that HB-EGF, CCL-2, ANG-2 and VEGF-C were downregulated in treated systems while MMP-1 was upregulated, **Figure 3.6C**. Overall, this effect was most pronounced in systems receiving combined

treatment. These results further demonstrate the sensitivity of our system to detect changes in secretome profiles in response to therapeutic inhibitions.

3.3.7 Combination of Tocilizumab, Reparixin and UK-356618 Reduces BCC-Induced Barrier Dysfunction and BCC Migration in The Extravasation Model

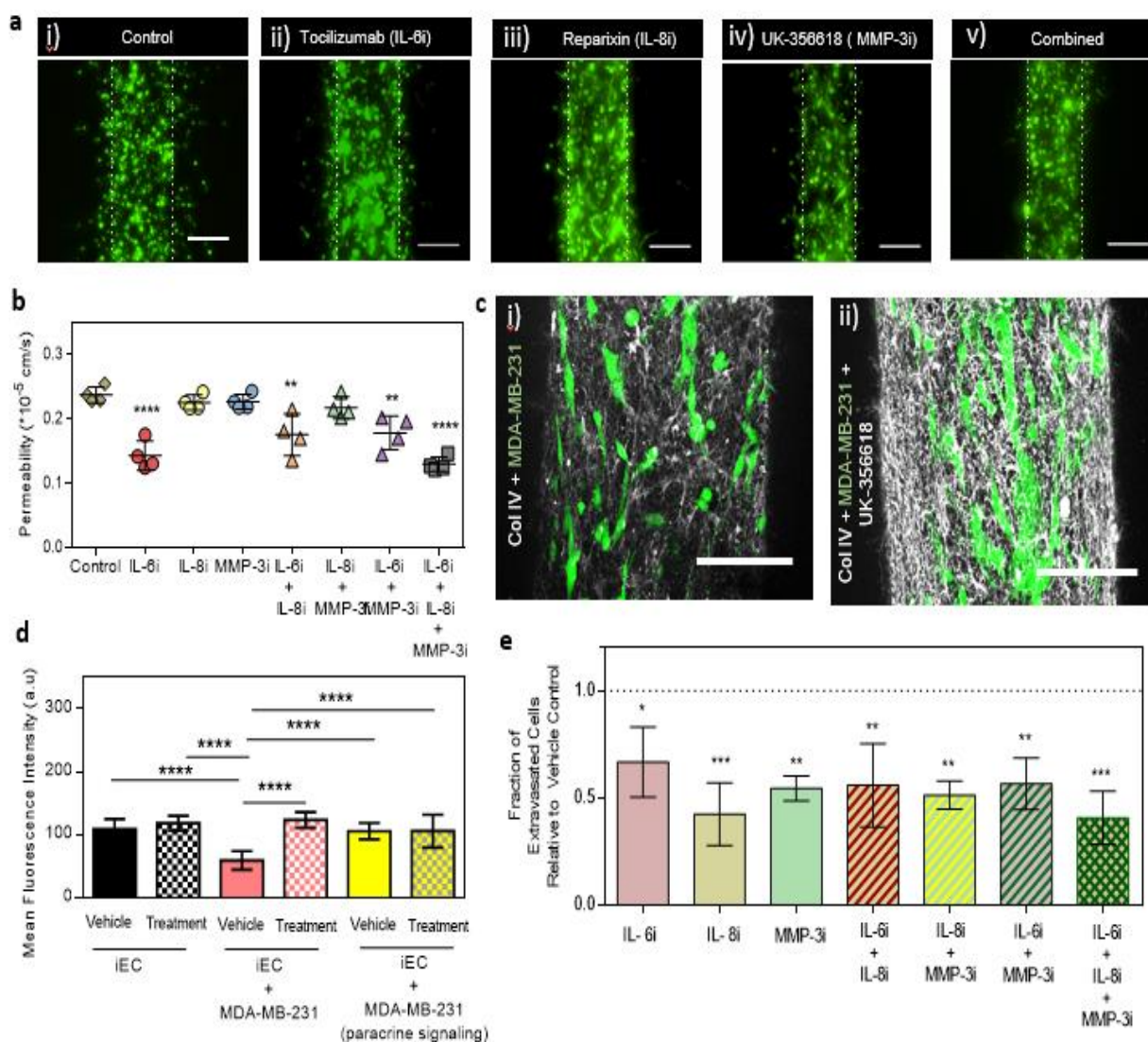


Figure 3.7 Functional responses (vessel permeability, basement membrane remodeling and extravasation events) of systems treated with therapeutic inhibitors. (A) Fluorescent images of MDA-MB-231 cells after 24 hours of culture under control (i), tocilizumab treatment (IL-6R, ii), MMP-3 inhibitor treatment (iii) and reparixin treatment (IL-8R, iv) and combined treatment (v), scale bar indicates 200 μ m. (B) The graph shows permeability coefficients of

iPSC-EC vessels for seven treatment conditions examined including no treatment control, independent treatment, and combination treatment. Plot: mean permeability + SD, statistical analysis: Student-test, **** $p \leq 0.0001$, ** $p \leq 0.01$ (n=4). (C) Confocal images showing Col IV deposition on (i) vehicle treated and (i) UK-356618 treated iPSC-EC vasculatures in direct contact co-culture with MDA-MB-231 cells, scale bar indicates 150 μm . (D) Mean fluorescence intensity analysis of Col IV deposition on vehicle treated and UK-356618 treated iPSC-EC vasculatures in monoculture or co-culture conditions with MDA-MB-231 cells. Plot: mean fluorescence intensity + SD, statistical analysis: ordinary one-way ANOVA with Tukey's multiple comparisons test, **** $p \leq 0.0001$. (E) Relative fraction of extravasation events for seven treatment conditions examined relative to vehicle control, including independent treatment, combined treatment of two inhibitors and all inhibitor treatments combined. Plot: Relative fraction of extravasated cells + SD, statistical analysis: Dunnett multiple comparison test, * $p \leq 0.05$, ** $p \leq 0.01$, *** $p \leq 0.001$ (n=4).

We also investigated the effects of therapeutic inhibition on extravasation behavior and vascular properties including barrier function and structural remodeling within the model. To examine if combined inhibition of IL-6, IL-8 and MMP3 induced a synergistic response in extravasation behavior and endothelial barrier function we exposed our co-culture systems to independent treatment and combinations of inhibitors. Confocal microscopy revealed that extravasation events declined in all the conditions analyzed compared to vehicle controls, **Figure 3.7A**. Previously, our results showed that extravasation of BCCs increased alterations to COL IV, deposited by iPSC-EC vessels, through direct-contact interactions more than through paracrine signaling. Given that MMPs play critical roles in degrading basement membrane components during tumor invasion, we explored the effects of MMP inhibition on COL IV remodeling during extravasation within our model. Our results show that UK-356618 treated systems had higher COL IV expression, as demonstrated by immunofluorescence staining, indicative of lower COL IV degradation during direct-contact interactions between cancer cells and the vasculature, **Figure 3.7B**. As previously established, COL IV expression was higher in monocultures of iPSC-EC vessels and in indirect-contact co-cultures than in direct-contact co-culture conditions, and vehicle treatment did not change these trends. A

slight, but not statistically significant increase in COL IV expression was observed in UK-35661 treated iPSC-EC vessels in monocultures relative to vehicle controls, **Figure 3.7C**. This trend was also observed in indirect contact signaling conditions, **Figure A.10**. These results suggest that MMP inhibition using UK-356618 can significantly reduce some of the COL IV remodeling observed in cancer-vascular crosstalk, particularly during physical contact interactions between cancer cells and the vasculature in extravasation. Consistent with ICAM-1 expression analysis in **Figure 3.2**, co-culture conditions resulted in a higher ICAM-1 expression overall, however no additional effects were observed in response to treatment compared to respective vehicle controls, **Figure A.11**.

Next, we examined the impact of tocilizumab, reparixin and UK-356618 on iPSC-EC vessel integrity during direct-contact co-culture with MDA-MB-231 cells. We found that vascular permeability decreased significantly in iPSC-EC vessels treated with tocilizumab independently, **Figure 3.7D**, and in pair combination with reparixin or the UK-356618. No notable changes in permeability were observed for other inhibitors and their paired combinations, however, combined treatment of all three inhibitors exhibited similar decrease in permeability to tocilizumab treatment. When treated independently, reparixin induced the greatest decline in quantified extravasation events, followed by the UK-356618 and tocilizumab, respectively, **Figure 3.7E**. Extravasation events also declined when pairs of inhibitors were applied: tocilizumab + reparixin, reparixin + UK-356618 and tocilizumab + UK-356618. Notably, reparixin induces a stronger response in reducing extravasation events, compared to other inhibitors or their paired

combinations. Combination of tocilizumab, reparixin and UK-356618, however, maximally reduced extravasation events to nearly 50% of the vehicle control, suggesting an additive effect on extravasation behavior of MDA-MB-231 cells. Taken together, these results show that tocilizumab and reparixin independently reduce iPSC-EC vessel permeability and MDA-MB-231 extravasation events respectively, however, combination of tocilizumab, reparixin and UK-356618 mitigates both functional changes.

3.4 Discussion

Extravasation of tumor cells are rare and transient in nature, making it the most difficult step in the metastatic process to study. Despite this challenge, various *in vivo* and *in vitro* studies have been conducted and indicate that entry into the perivascular space is heavily regulated by interactions between the various constituents of the metastatic microenvironment^{19,99}. During extravasation, juxtacrine and paracrine signaling between tumor cells and ECs are known to modulate endothelial function, remodel the ECM and promote transendothelial migration. While numerous microfluidic platforms have been developed to study mechanisms of cancer cell extravasation, few models have demonstrated their utility in conducting parametric studies on the functional assessment of therapeutic drugs. Development of models that can probe molecular and functional features of cancer-vascular interactions during extravasation in a higher-throughput fashion would advance discovery of treatment strategies to inhibit metastasis. Here, we developed an arrayable organotypic model of BCC extravasation to examine molecular signaling between cancer cells, endothelium and the ECM that influence function-level response. We demonstrated here the capabilities of our arrayable platform to study

cancer cell extravasation by 1) assessing the influence of juxtacrine/paracrine signaling on vascular barrier function and migratory behavior of cancer cells, and 2) evaluating downstream secreted factors and functional responses to multiple therapeutic inhibitors and their combinations.

The organotypic BCC extravasation model consists of an endothelial vessel (~250µm diameter) with cancer cells adhered to the inner surface of the vessel. The vessel recapitulates *in vivo* tubular structures within a collagen-fibrinogen matrix and is generated from human induced pluripotent stem cell-derived endothelial cells. iPSC-ECs are a desirable cell source as they can be engineered to acquire organ-specific properties and can enable the study of site-specific signatures in cancer metastasis^{113,114}. Moreover, metastatic dissemination can be studied using models developed from patient derived IPS cells for applications in drug screening and precision medicine therapies. iPSC-EC vessels generated within our systems exhibit both functional and morphological characteristics of a robust and stable endothelium, which include tight-junctional and endothelial-specific markers, basement membrane deposition and barrier function.

To demonstrate the ability of our model to mimic *in vivo*-like extravasation behavior, we assessed extravasation behavior of highly invasive (i.e., Hs-578T and MDA-MB-231) and poorly invasive (i.e., MCF-7) BCCs within our systems and showed a positive correlation between extravasation capabilities and invasive/metastatic potential observed *in vivo*. We also demonstrate the impact of BCC secretion on endothelial

properties and direct-contact remodeling of basement membrane components by BCCs. Tumor cells are also known to modulate and prime the endothelium by upregulating pro-metastatic signaling pathways. Endothelial ICAM-1 expression is involved in tumor cell adhesion to the endothelium during metastasis, which is common across numerous types of cancer¹¹⁵. Moreover, ICAM-1 expression on the endothelium correlates with the production of pro-tumoral cytokines that are associated with enhanced vascular permeability. We observed increased ICAM-1 expression in our iPSC-EC vessels in response to MDA-MB-231 cells within our system, which demonstrates cancer cell derived modification of endothelial behavior through paracrine signaling to promote adhesion and extravasation. Aside from paracrine signaling-mediated modifications, physical modulation of the endothelial basement membrane is also observed in our system. This is consistent with previous reports showing that in tail vein-injected mice, colon carcinoma cells exit blood vessels by dynamically remodeling the endothelium and the basement membranes to induce gaps. For instance, transmigrating cells are known to remodel type IV collagen, a major component of the basement membranes, through either proteolytic or non-proteolytic processes²⁴. In our model, large areas of COL IV discontinuities surrounding iPSC-EC vessels can be observed where extravasation of MDA-MB-231 cells is found. Moreover, gaps were seen localized to the sites of BCCs suggestive of COL IV remodeling to create passageways for transmigrating cells.

Next, we performed secreted factor analysis on several BCC lines within our system to better define paracrine signaling-mediated cancer-vascular crosstalk. Our analysis

revealed distinct expression profiles of oncological factors associated with breast cancer metastasis for highly invasive and poorly invasive BCC lines. We found that for invasive breast cancer lines (Hs-578T and MDA-MB-231), IL-6, IL-8, and MMP-3 secretions were upregulated. Consistent with these findings, previous clinical studies have shown that both IL-6 and IL-8 are found at high concentrations in serums of lung and liver metastasis cancer patients¹¹⁶ and these concentrations correlate with the stage of cancer¹¹⁷. Moreover, MMP-3 secretion is associated with breast cancer invasiveness¹¹⁸. Interestingly, it is also known to play a pivotal role in the degradation/remodeling of laminin and COL IV¹¹⁹, which may suggest a role of MMP-3 secretions in MDA-MB-231-mediated COL IV remodeling observed within our system. In breast cancer metastasis, IL-6 is known to induce disruption of endothelial barrier function^{120,121}. Moreover, both IL-6 and IL-8 have been shown to synergistically enhanced BCC migration in a density-dependent manner¹⁰³. To resolve the cancer-endothelial crosstalk observed within our system, we identified the independent contributions of iPSC-EC vessels and MDA-MB-231 cells, to the overall secretion of IL-6, IL-8 and MMP-3. We found that MDA-MB-231 cells secrete higher levels of IL-6 and IL-8 in response to signaling from iPSC-EC vessels while higher MMP-3 levels are secreted by the vessels in response to BCC signaling. Furthermore, these results correlate with higher cancer cell migration rates and increased vascular permeability observed within our system, demonstrating the impact of paracrine signaling on cellular function. Taken together, this suggests that BCCs may promote their own migration and impair vascular function through IL-6 and IL-8 secretions in response to paracrine signaling from the vasculature. Likewise, the iPSC-EC vasculature may also be promoting basement membrane degradation and

consequently tumor cell motility via MMP-3 secretions in response to factors secreted by BCCs. The approach used here to elucidate these molecular signaling illustrates the potential of our model in deciphering cell type-derived molecular factors driving extravasation of tumor cells.

In vitro studies report that during cancer cell extravasation, alterations to the endothelium are made temporarily where the vessel integrity is restored quickly after transmigration^{19,122}. However, our molecular diffusion analysis showed an increase in vascular permeability following transmigration of cancer cells, suggesting a more complex conditioning capability of the vasculature by BCCs. Contact-dependent juxtacrine signaling in addition to paracrine signaling are important drivers of cancer cell-mediated changes to endothelial barrier function during cancer cell extravasation⁸⁵. Our analysis confirmed that increases in endothelial permeability results from both juxtacrine interactions and paracrine signaling between iPSC-EC vasculature and BCCs. Interestingly, our results suggest that paracrine signaling alone are sufficient to promote increased vascular permeability and enhanced MDA-MB-231 cell migration. While it is difficult, with the current setup, to resolve the contributions of cancer-endothelial dependent juxtacrine interactions from the contributions of paracrine signaling that inherently exists within a co-culture microenvironment, we demonstrate the extent to which direct-contact interactions enhances the functional changes elicited by paracrine signaling. We hypothesized that the upregulation of IL-6, IL-8 and MMP-3 may partially account for the functional changes observed within our system, including increase in vascular permeability, enhanced cancer cell extravasation, and cancer cell-

mediated COL IV degradation. To further elucidate the contributions of these factors to the functional changes observed, we conducted blocking experiments within our model.

FDA-approved drugs that specifically target metastasis are few in numbers, yet metastasis is the leading cause of cancer-related deaths. The heterogeneity of tumor in metastases makes it challenging for single-agent therapies that are essential for tumor cell survival or proliferation to produce sustained results¹²³. Many therapeutics are currently combined based on evidence from additive or synergistic effects observed in preclinical models and in patients^{111,123}. New treatment strategies will need to consider therapeutic interference of multiple receptors, signaling pathways and their supporting microenvironments to overcome drug resistance and produce sustainable, long-term control over tumor growth. Our work suggests that by concurrently inhibiting IL-6, IL-8 and MMP-3 the impact on extravasation events of MDA-MD-231 cells as well as endothelial structure and barrier function can be reduced. An antibody inhibitor for MMP-3, UK-356618, and clinically active therapeutics tocilizumab and reparixin were used in these investigations. Broad-spectrum MMP inhibitors have met with mixed outcomes against cancer, partly due to the anti-cancer benefits of some MMPs. As a result, highly specific MMP targets are now being tailored to reduce adverse systemic effects. Tocilizumab and reparixin have been in current clinical trials both individually or in combination with other therapeutics for their effectiveness against several cancer types and metastasis^{124,125}. Our results indicate that MMP inhibition using UK-356618 significantly mitigated COL IV remodeling and overall extravasation events that resulted from MDA-MB-231 cell interactions with iPSC-EC vasculatures. This further confirms

our hypothesis that upregulated MMP secretions facilitates cancer cell extravasation by basement membrane degradation. Our investigations have also revealed that reparixin was most effective at reducing extravasation events of MDA-MB-231 cells when used independently or in combination with both tocilizumab and UK-356618. However, reparixin alone or its combination with any one of the IL-6 or MMP-3 inhibitors did not prevent vascular impairment to the same extent as simultaneous inhibition of all three factors did. Similarly, tocilizumab prevented impairment of vascular barrier function when used alone or combined with other inhibitors but did not impact cancer cell migration significantly. Combined treatment of reparixin, tocilizumab and UK-356618 were required to prevent simultaneous changes in cancer migration behavior and vascular permeability. Together, these results highlight the importance of exploring combination treatment strategies to enhance effectiveness of controlling cancer dissemination by targeting multiple pathways and mechanisms.

Indeed, other factors such as ECM density, may also have interdependent roles in the cellular responses observed in this study. For instance, recent work examining the role of ECM density in conditioning lymphatic vessel properties revealed that higher matrix density resembling cancerous tissue (i.e., COL-I density of 6 mg/mL) induces higher secreted levels of IL-6 and exacerbates vessel leakiness compared to lower matrix density (i.e., COL-I density of 3 mg/mL)¹⁰⁰. Moreover, an increase in ECM density has also been shown to impact MMP secretion rates and enhance invadopodia-mediated ECM degradation by MDA-MB-231 cells¹²⁶. While the current study uses a normal collagen density of 3 mg/mL, these studies indicate that ECM density may also have

influence on the levels of secreted levels of factors such as IL-6 and MMPs investigated within our system. Future studies could explore the specific roles and impact of other biological factors on vascular barrier integrity and cell migration behavior observed in this model.

One important aspect of the organotypic modeling approach used here is the ability to compartmentalize and de-couple contributions of individual microenvironmental factors which can be challenging and costly to do *in vivo*. By sequentially adding supporting cell types and ECM components, independent contributions as well as contributions from crosstalk between various microenvironmental components can be determined using this model. More importantly, future studies incorporating IPS cells from patients affected by metastatic disease or patient-derived cells could be used to accelerate the development of new therapies targeting or preventing cancer metastasis. Potential application of this model could be extended to stratify patients that will develop metastatic disease.

In conclusion, we have presented here a 3D organotypic vascularized model to analyze the cancer cell-EC interactions involved in BCC extravasation. We have provided quantitative assessment of the interplay between BCCs and the endothelium by investigating paracrine signaling and functional responses of the endothelium and BCCs resulting from these interactions. Moreover, we identified the role of IL-6, IL-8 and MMP-3 in regulating vascular permeability and cancer cell extravasation behavior. Our data revealed that metastatic cell line MDA-MB-231 upregulates secretions of IL-6 and IL-8

in response to crosstalk with iPSC-EC vasculatures to impair barrier function and influence their own extravasation behavior. Conversely, iPSC-EC vasculatures respond to this crosstalk by secreting more MMP-3 and promoting BCC migration by degradation of basement membrane components. Combined therapeutic inhibition of these factors reduced overall secretion of metastasis-promoting factors, vascular impairment, and events of BCC extravasation. Importantly, we demonstrate the utility of our system in conducting highly parametric studies and testing combination therapeutics that target multiple and distinct signaling interactions involved in BCC extravasation.

3.5 Acknowledgments

We thank a predoctoral fellowship (F31CA247248) from the National Institute of Health (NIH) to M.H. We also acknowledge University of Wisconsin Carbone Cancer Center Support Grant (NIH P30CA014520) and the NIH (R01CA186134) for funding support.

Chapter 4

Innate immune cell response to host-parasite interaction in a human intestinal tissue microphysiological system

Protozoan parasites that infect humans are widespread, and lead to varied clinical manifestations, including life-threatening illnesses in immunocompromised individuals. Animal models have provided insight into innate immunity against parasitic infections; however, species-specific differences and complexity of innate immune responses make translation to humans challenging. Thus, there is a need for novel *in vitro* systems that can elucidate mechanisms of immune control and parasite dissemination. We have developed a human microphysiological system of intestinal tissue to evaluate parasite-immune-specific interactions during infection, which integrates primary intestinal epithelial cells and immune cells to investigate the role of innate immune cells during epithelial infection by the protozoan parasite, *Toxoplasma gondii*, which affects billions of people worldwide. Our data indicate that epithelial-infection by parasites stimulates a broad range of effector functions in neutrophils and NK cell-mediated cytokine production that play immunomodulatory roles, demonstrating the potential of our system for advancing the study of human-parasite interactions.

This chapter has been adapted from a prepared manuscript titled "Innate immune cell response to host-parasite interaction in a human intestinal tissue microphysiological system" The manuscript is authored by Mouhita Humayun, Jose M. Ayuso, Raven A. Brenneke, Keon Young Park, Bruno Martorelli Di Genova, Melissa Skala, Sheena C Kerr, Laura J. Knoll, David J. Beebe

4.1 Introduction

Infections caused by parasitic pathogens are a global health problem that affects more than a quarter of the world's population, yet effective antiparasitic therapeutics are limited and often come with severe adverse reactions. Similarly, vaccines are limited for any food or water-borne parasitic infection¹²⁷. Immune responses initiated by the innate immune system in the intestinal tissue are a part of the frontline defense against parasitic infections. A more complex picture of their role in shaping protective immunity development and pathogenesis are beginning to emerge. Infection by the protozoan and intracellular parasite *Toxoplasma gondii* affects about a third of humans worldwide making it one of the most widespread human pathogens in the world ¹²⁸. Human exposure to *T. gondii* infection occurs primarily through the oral route due to ingestion of contaminated food or water¹²⁹. However, there are significant knowledge gaps in how the innate immune system interacts with human intestinal parasites like *T. gondii* in the local microenvironment of the intestinal tissue that either reduce parasite dissemination or contribute to the development of invasive systemic disease. As responses to parasitic infection by the innate immune system play key roles in shaping protective immunity, improved knowledge of the mechanisms that initiate innate immunity and contribute to pathogenesis are central to developing effective therapeutics and vaccines.

The gut epithelium and vascular barrier regulate what enters the host tissue beyond the intestinal epithelial barrier and what enters the circulation. Functionally, the intestinal epithelial barrier separates the luminal contents from immune cells found in the gut parenchyma and prevents the systemic dissemination of the microbiota and enteric

pathogens to liver, spleen, and other peripheral tissues¹³⁰. During parasitic infection, immune cells in the gut-parenchyma coordinate host-protective responses necessary for resolving acute infection and preventing tissue-dissemination¹³¹. Currently, murine hosts are predominantly used as translational models for *T. gondii* infections in humans. Despite the vast knowledge of basic and translational human immunology obtained from mouse studies, several components of the mouse immune system are incongruent with the human immune system^{21,132}. Humanized mice allow for improved modelling of the human immune systems and have emerged as alternatives to traditional rodent models. However, challenges remain due to the lack of critical adhesion molecules and other signaling proteins in humanized mouse models that are required for mounting human-specific immune responses to infections^{133,134}. While *in vivo* animal models replicate microenvironmental complexity and physiological conditions, several aspects including species-specific differences, limited ability to image pathogen trafficking and the time/expense of mechanistic study makes investigation of pathogen trafficking challenging in these models. Thus, there is a need for relevant human *in vitro* models to interrogate the innate immune responses to pathogens.

Organ-on-chip devices and microphysiological systems (MPSs) have overcome some of the challenges of traditional *in vitro* approaches by enabling the integration of three-dimensional (3D) complexity, spatial organization and relevant cell-cell and cell-extracellular matrix interactions for modeling *in vivo*-like responses^{135–137}. Several technologies for modeling pathophysiological processes in human tissue have emerged that represent important steps forward in the evolution of organ-on-a-chip platforms.

MPS of the lung^{50,138,139}, brain¹⁴⁰, bladder¹⁴¹, liver¹⁴² and intestine^{45,49,64,143–145} have been developed for studies of host interactions with viruses, fungi, bacteria, and parasites^{29,46}. In the context of modeling host-microorganism interactions, viral infections and bacterial colonization in the epithelia have been the primary applications of MPSs, with emerging applications in testing antiviral therapeutics and modeling innate immune responses. Immune cell trafficking across endothelial and epithelial barriers have been studied using these models^{64,146}, but difficulties persist with integrating membrane-free interfaces that mimic tissue composition of the gut epithelial and vascular barrier, including cellular and extracellular matrix (ECM) components, and tissue architecture (i.e., endothelial vessel, epithelial lumen geometry) that can critically influence host and pathogen responses. Recent efforts to model the 3D tissue anatomy of intestinal epithelia have culminated in the establishment of organoid-on-a-chip systems that retain the cellular diversity and regenerative potential offered by organoid technology while addressing the problem of lumen accessibility using microengineering or tissue engineering approaches^{48,147,148}. Using advanced 3D bioprinting techniques, culture of intestinal tubes can be maintained long-term in ECM gels within these systems¹⁴⁷. These systems can support *in vitro* tissue homeostasis of the intestinal epithelium, and its interactions with underlying tissue components. However, functional responses of innate immune cells and concomitant molecular analysis of responses to microorganisms in these models have not been characterized.

In this work, we developed a novel MPS of the human intestinal tissue to study host-parasite interactions and innate immune cell response to parasite infection *in vitro*. By

using a highly tractable micromolding technique for creating hollow structures, we generated tubes of intestinal epithelium and endothelium supported by ECM gel, recapitulating the lumen geometries of the gastrointestinal tract and blood vessels. We microengineered a human-relevant model of the gut-epithelium and vascular barrier, within the intestinal tissue, that provides means for studying gastrointestinal parasitic infections and the associated interactions with innate immune cells. We demonstrate adaptation of this model to incorporate primary human intestinal stem cells from organoids derived from intestinal tissue resections. We used the system to model parasite invasion and replication within the intestinal epithelium, followed by leukocyte trafficking to the site of infection. Neutrophils and NK cells are critical for early protection and reducing parasite burden during *T. gondii* infection^{149,150}. By measuring gene transcription, metabolic changes, and cytokine secretions, we gained interesting insights into the function of human innate immune cells, including neutrophils and NK cells, during the initial stages of *T. gondii* parasite infection of the intestinal epithelium. Hence, the engineered MPS model of the intestinal tissue emulates critical features of host-parasite interactions enabling us to address questions related to human-relevant tissue response, activation of innate immunity, and the role of immune cells in parasite dissemination.

4.2 Results

4.2.1 Development of an Intestinal Tissue MPS for Studying Host-Pathogen

Interactions

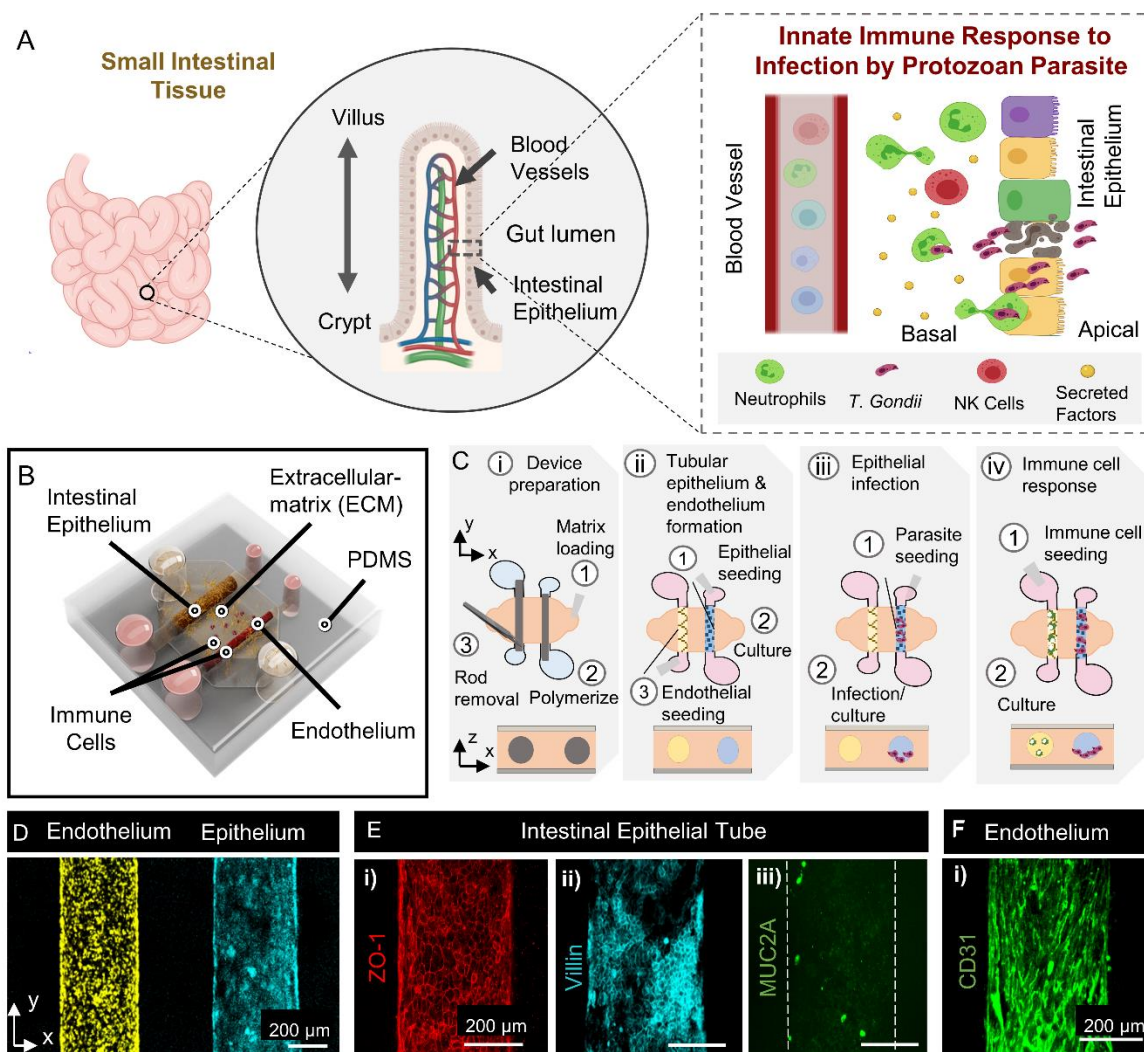


Figure 4.1 Human intestinal tissue microphysiological system for studying innate immune responses to parasitic infection. (A) Schematic representation of the design rationale for modeling parasite infection of the intestinal epithelium and innate immune cell responses. (B) 3D rendered illustration of the intestinal tissue MPS which include tubular intestinal epithelium and endothelium within an ECM gel. Immune cells are introduced into the lumen of the endothelium for modeling and elucidating innate immune responses to parasite infection of the epithelium. (C) Schematic representation describing the experimental approach to setup each component (i-iv) of the MPS used in this study. (D) Fluorescence image showing the formation of a confluent Caco-2 intestinal epithelium (yellow) and HUVEC endothelium

(cyan). (E) The model retains phenotypic characteristics of tight junction markers (i, ZO-1), microvilli markers (ii, villin) and markers of mucus producing goblet cells (iii, MUC 2A) for the epithelium. (F) HUVEC endothelium in the co-culture with the epithelium retains expression of endothelial marker (CD31).

Infection by *T. gondii* is naturally acquired through oral ingestion of food or water that are infected with parasite cysts or oocysts¹⁵¹. The intestinal epithelium, characterized by a villus-crypt axis consisting of a single layer of constantly renewing and differentiating epithelial cells, separates microbes in the lumen from the intestinal vascular systems,^{26,152} **Figure 4.1A**. Experiments in mice and cell line/explant studies have shown that translocations of *T. gondii* from the apical surface of the intestinal epithelium to the basal side, during acute infection, may occur via epithelial transmigration or following epithelial invasion and intracellular replication^{153,154}. Tissue damage caused by the *T. gondii* epithelial invasion and intracellular replication leads to the secretion of a host of inflammatory factors by intestinal tissue-resident cells¹⁵⁵, **Figure 4.1A**. Presence of these factors increases the expression of integrins and chemokine receptors on endothelial cells of local vasculature that promote immune cell extravasation into the lamina propria. Leukocytes, primarily neutrophils, are then recruited to the site of infection from neighboring vasculature where they encounter effector-enhancing cytokines and pathogen-derived products to neutralize the parasite by killing or controlling their replication^{151,156–158}, **Figure 4.1A**. Other innate immune cells such as NK cells are also recruited from the vascular system that further amplifies the inflammatory response by producing effector-enhancing cytokines^{159,160}, **Figure 4.1A**. A robust immune response during these early stages of the *T. gondii* infection is critical for shaping innate immunity which in turn induces acquired immunity.

To model these initial stages of *T. gondii* infection, we bioengineered an intestinal tissue MPS that incorporates 3D tubular structures of the intestinal epithelium and the endothelium, and immune cell components to allow the analysis of host immune responses against intestinal pathogens in a more physiologically relevant culture microenvironment, **Figure 4.1B**. Inspired by previous work by ourselves and others, we generated lumen structures within a gas and nutrient-permeable collagen-based ECM hydrogel using a micromolding technique for modeling tubular geometries of the intestinal epithelium and the gut vascular barrier within intestinal tissue^{42,147,161–163}. The hydrogels are integrated into a polydimethylsiloxane (PDMS) elastomeric device with a central chamber, that contains the ECM gel, connected to two pairs of inlet and outlet ports that support PDMS rods used for molding the tubular structures, **Figure 4.1C i**. Following ECM gel polymerization, the rods are pulled out of the chamber leaving behind hollow lumen structures. The inlet and outlet ports connected to the chamber provide direct access to the lumens which can be used for cell seeding and for the supply of medium and growth factors during culture. We injected and cultured intestinal epithelial cells inside one of the tubular structures to form an epithelial lumen with direct access to the apical surface. After the epithelial lumen is formed, in the same manner, we seeded and cultured vascular endothelial cells in the adjacent lumen to generate a biomimetic endothelial vessel, **Figure 4.1C ii**. To model epithelial invasion of *T. gondii*, parasites are seeded into the apical surface of the epithelium through the inlet port and cultured, **Figure 4.1C iii**. Next, immune cells are introduced directly into the endothelial vessel and cultured for evaluating the immune response, **Figure 4.1C iv**. Altogether, our model mimics critical components of the intestinal tissue including the epithelium,

adjacent blood vessels, and immune cell components for studying responses to infection by protozoan parasites. For initial characterization of the model, we generated tubular intestinal epithelium using the human colon epithelial cell line, Caco-2 and formed a tube-shaped endothelial vessel using human umbilical vein endothelial cells (HUVECs), **Figure 4.1D**. The ECM hydrogel provides structural support for the formation of continuous layers of epithelial and endothelial cells that functions as a barrier between the apical side of the lumen and the underlying matrix. The intestinal epithelium generated within our system expresses tight junction marker ZO-1, which is involved in barrier function, as well as villin-1 which is involved in microvilli formation and epithelial restitution after damage, **Figure 4.1E i-ii**. The intestinal epithelium is increasingly recognized as a critical component of mucosal innate immunity against invading microorganisms through the secretion of mucin and antimicrobial proteins. We demonstrate the expression of mucin 2 (MUC2), which is secreted by goblet cells in the intestinal epithelium and forms a major component of the inner mucus layer, **Figure 4.1E iii**. Expression of these cell lineage markers indicates differentiation and maturation of the epithelium cultured within our system. To assess characteristic features of the endothelial vasculature, we stained for and observed the expression of endothelial junction protein CD31, **Figure 4.1F**. Together, these results show that co-cultures of tubular intestinal epithelium and endothelium supported by collagen-based ECM gel retain the phenotypic characteristics of a mature epithelium and endothelium.

4.2.2 Generation and Characterization of Primary Small Intestinal Tubes in the Intestinal Tissue MPS

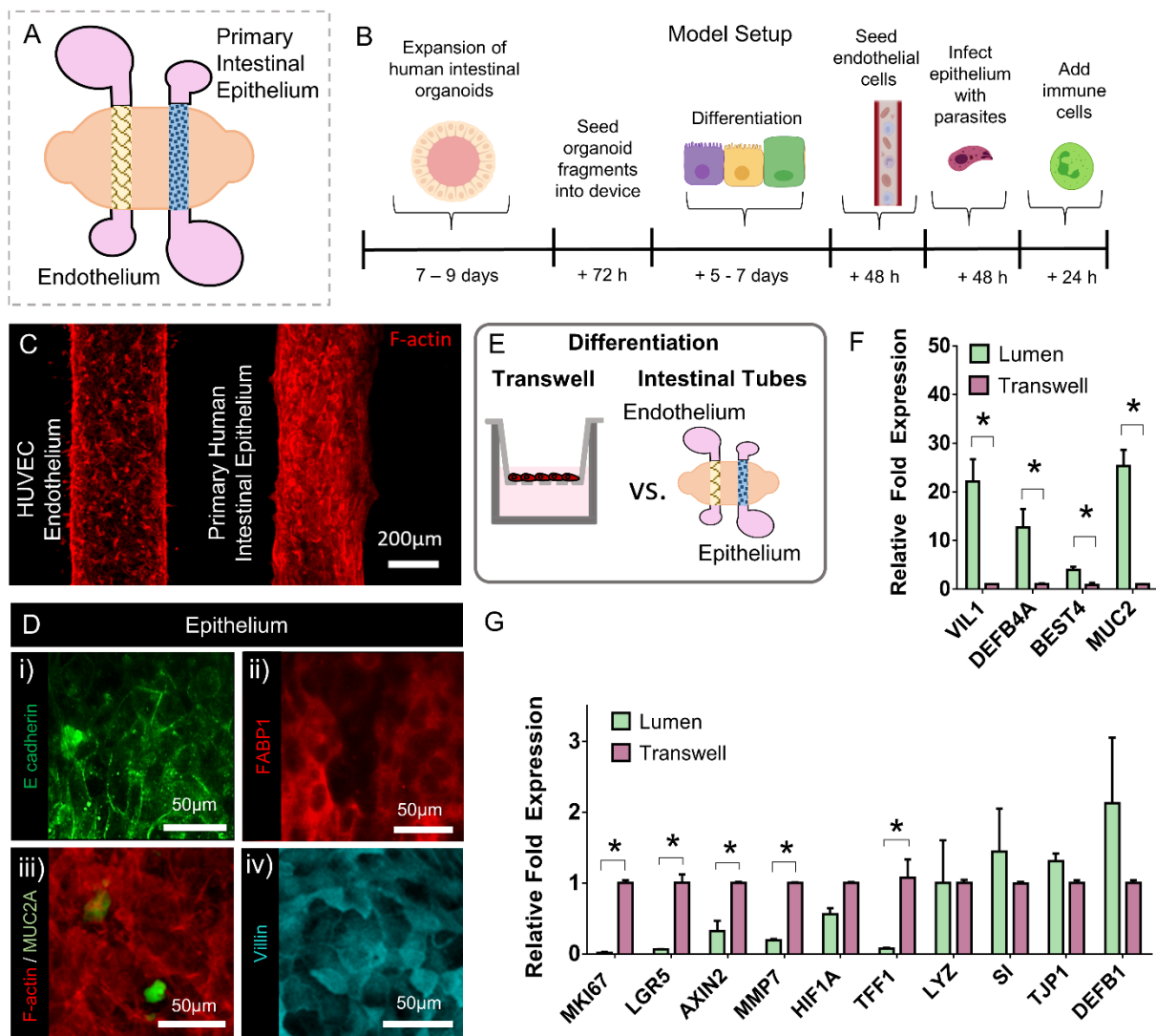


Figure 4.2 Integrating primary intestinal epithelial cells in the human intestinal tissue MPS. (A) Schematic representing the spatial distribution of the tubular intestinal epithelium and endothelium used in the intestinal tissue MPS. (B) Optimized culture protocol and timeline to setup the intestinal tissue MPS. This includes expansion of intestinal organoids, formation of intestinal tubes, differentiation of the epithelium, formation of the tubular endothelium, parasite infection of the epithelium and addition of immune cells into endothelium. (C) HUVEC endothelial cells and primary intestinal epithelial cells formed lumen structures in the intestinal tissue model as shown by immunostaining of F-actin (red). (D) Following culture and differentiation of the tubular epithelium, the intestinal epithelial cells show retention of phenotypic characteristics including expression of (i) epithelial cell-adhesion protein (E-

cadherin, green), (ii) enterocyte-specific marker (FABP1, red), (iii) marker for mucin-producing cells (MUC 2A, green), and (iv) marker for protein involved in formation of microvilli (Villin 1, cyan). (E) Schematic representing the culture and differentiation of human primary intestinal epithelial cells in transwells and in the intestinal tissue MPS. (F) Bar graph showing differential gene expression of markers associated with proliferation and differentiation, and a functional intestinal epithelium in the intestinal tissue MPS versus in transwell culture. Genes analyzed include villin-1 (VIL1) for microvilli formation; β -defensin-4 (DEFB4) for antimicrobial peptides; Bestrophin-4 (BEST4) for absorptive cells and mucin 2 (MUC2) for goblet cells. (G) Bar graph showing gene expression of downregulated genes along with other markers of intestinal epithelial cells in the intestinal tissue model versus in transwell culture. Genes analyzed include proliferation marker (MKI67) for stem cells, leucine-rich-repeat-containing G-protein-coupled receptor 5 (LGR5) for intestinal stem cells; Axis Inhibition Protein 2 (AXIN2) for crypt regeneration; Matrix Metalloproteinase-7 (MMP7) bactericidal and anti-inflammatory effects; hypoxia-inducible factor-1 (HIF1A) for hypoxia; Trefoil Factor 1 (TIFF1) for mucosal repair; lysozyme (LYZ) for Paneth cells; sucrase-isomaltase (SI) specific for absorptive enterocytes; tight junction protein-1 (TJP1) for tight junctions in the epithelium and β -defensin-1 (DEFB1) for antimicrobial peptides. Values are presented as mean \pm SD from 4 independent experiments involving tubular or monolayer epithelium generated from human intestinal organoids (asterisk denotes P value of ≤ 0.05).

In vitro cultures of patient or iPSC-derived intestinal epithelial stem cells in 3D organoids can generate a fully differentiated and polarized epithelium^{164–166}. However, the relative inaccessibility of the apical surfaces makes the inoculation of larger pathogens, such as *T. gondii* compared to bacteria or viruses, into the cavity difficult to perform. Moreover, the variable 3D geometry of organoids makes real-time imaging of host-pathogen interactions technically challenging. Therefore, we adapted our intestinal tissue MPS to integrate the formation of tubular epithelium using primary human intestinal epithelial cells, from intestinal organoid fragments, to provide a model that retains the major epithelial cell types and provides easy access to the apical surface, **Figure 4.2A**. To incorporate primary human intestinal epithelial cells, we obtained surgical samples from macroscopically normal regions of the human small intestinal tissue. Human intestinal crypts containing functional stem cells, derived from the jejunum region of the small intestine, were used to generate organoids, and cultured for > 5 passages prior to use within our model. Jejunal organoids cultured in an expansion medium for 7-9 days were

dissociated into a mix of fragments and single-cell suspensions before being introduced into the lumen tube of the microdevice, **Figure 4.2B**. To maximize coverage of the luminal surface, primary small intestinal cells were seeded into the device twice and cultured in expansion media for 24h between each cell seeding. The device was flipped upside down prior to the second round of cell seeding to facilitate cell adhesion to the top half of the lumen surface. Initially, the large majority of cells appear spread across the luminal surface within 1-2 days of cell seeding and progressively grow to form a continuous epithelium. Following cell adhesion to the matrix (approximately 72h from initial cell seeding), the culture medium is changed to a differentiation medium, and the intestinal epithelium is cultured for 5-7 days to promote differentiation of epithelial subtypes. We utilized a previously published differentiation culture medium formulation and made further modifications (**see Materials and Methods**) to accommodate the culture of HUVECs in the adjacent lumen following differentiation of the epithelium. HUVECs were seeded into the adjacent lumen and the device was inverted every 30 min over a two-hour period to coat the lumen with endothelial cells. The tubes of intestinal epithelium and endothelium were co-cultured for an additional 48h prior to infection with *T. gondii*. For modeling immune response to parasite infection, the intestinal epithelial tube was infected with *T. gondii* for 48h and immune cells including neutrophils and NK cells were added to the lumen of the endothelium followed by co-culture within the model for 24-48h, **Figure 4.2B**.

The incorporation of human primary intestinal epithelial cells within our intestinal tissue model led to well-developed tubes of small intestinal epithelium and an adjacent

vascular lumen, as indicated by immunofluorescent staining of F-actin, **Figure 4.2C**. Furthermore, the small intestinal epithelial lumen expressed E-cadherin and FABP1 which are typical markers of intestinal epithelial origin ^{167,168}, **Figure 4.2Di and ii**. Similar to the tubes generated from the intestinal epithelial cell line, Caco-2, epithelial tubes generated primary intestinal epithelial cells exhibited positive expressions of MUC2 and villin, **Figure 4.2Diii and iv**.

In vivo, the intestinal epithelium rests on a supporting basement membrane composed of structural and adhesive proteins that epithelial cells use to anchor, migrate, and differentiate ¹⁶⁹. Matrix properties such as ECM ligands, stiffness and porosity are key factors that influence a wide range of cell behaviors including viability, tissue organization/architecture, and stem cell renewal and differentiation ^{170–173}. To further characterize the degree of differentiation induced in the intestinal tissue MPS, we conducted gene expression analysis of the intestinal tubes and compared the differentiation potential against epithelial monolayers grown in a standard culture platform (transwell), **Figure 4.2E**. Small intestinal epithelial cells in the intestinal tissue MPS and the transwell system were cultured under the same conditions: in the presence of expansion media for 2 days, followed by 7 days of culture in the differentiation medium. Reverse transcription and quantitative PCR (RT–qPCR) demonstrated that both the tubular (microphysiological model) and the monolayer (transwell) epithelium expressed region-specific marker, brush border enzymes such as sucrase-isomaltase (SI), which is native to jejunal tissue. SI gene expression was preserved beyond passage 25, indicating that the regional identities of organoids are

intrinsically programmed. Genes associated with normal proliferation and differentiation, or functional human intestinal epithelial cells were compared, **Figure B1 and 2**, and several genes were differentially expressed. RT-qPCR analysis revealed that jejunal epithelial differentiation in the intestinal tissue device resulted in increased expression of differentiation genes (VIL1 (marker for microvillar actin filament and enterocytic epithelial maturation), MUC2 (marker for mucin-producing cells), DEFB1 (marker for production of antimicrobial peptide, β -defensin 1), and SI) compared to differentiation in the transwell system, **Figure 4.2F**. Conversely, lower expression of proliferative genes (LGR5 (leucine-rich repeat-containing G-protein-coupled receptor 5, marker for stem cell renewal), KI67(a marker for proliferation), AXIN 2 (a marker for crypt regeneration), and MMP7(a known marker of Paneth cells, required for activating cell defensins ¹⁷⁴) were found in the intestinal tissue model relative to the transwell system,¹⁷⁴ **Figure 4.2G**. These results show that small intestinal epithelial cultures in the intestinal tissue model display features of their intestinal regional identity, and compared to standard culture techniques, exhibit improved differentiation characteristics/potential, and attenuated proliferative characteristics.

4.2.3 Modeling Protozoan Parasite Infection in Human Intestinal Epithelium

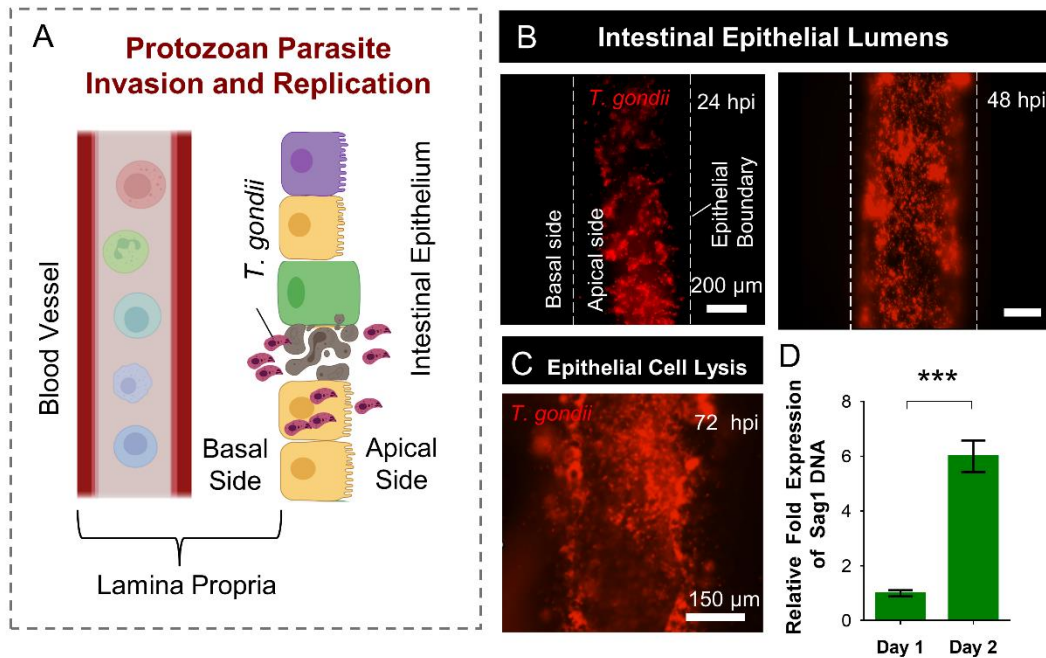


Figure 4.3 Modeling protozoan parasite invasion and replication in the intestinal epithelium. (A) Schematic representation of epithelial infection by *T. gondii*. Infection involves epithelial invasion, intracellular replication and transmigration or epithelial cell lysis of *T. gondii*, which release the parasites into the lamina propria containing immune cells and intestinal vasculature. (B) Caco-2 epithelial tubes were infected with m-cherry tagged *T.gondii* of the ME49 strain for 24h and imaged by fluorescence microscopy. The images depict time course images at 24h (i) and 48h(ii), showing that viable *T. gondii* were present within the epithelial lumen. White dotted line represents the epithelial boundary separating apical (luminal) surface from the basal surface. (C) Fluorescent images depicting epithelial cell lysis 72h following infection with m-cherry tagged *T.gondii*. (D) Gene expression analysis of genomic DNA from the epithelium for tachyzoite marker SAG1 shows significant up-regulation (approximately 6-fold expression) after 48h of infection relative to 24h. Values are presented as mean \pm SD from 2 independent experiments and 12 different devices (asterisk denotes P value of ≤ 0.001).

Having established that the intestinal tissue MPS recapitulates tubular geometries of the intestinal epithelium and vasculature, the system has strong potential for modeling parasite invasion, replication, and translocation beyond epithelium into the lamina propria, **Figure 4.3A**. *T. gondii* infects the small intestinal epithelium cells following ingestion of parasites found in contaminated meat, produce, or water ¹⁵¹. During acute

infection, *T. gondii* parasites that invade the intestinal epithelium differentiate into a rapidly replicating life-stage, referred to as the tachyzoite stage, which then disseminates throughout the body^{151,175}. To model *T. gondii* infection of the intestinal epithelium, we introduced tachyzoites into the tubular epithelium of our intestinal tissue MPS. Our model provides an exposed luminal surface accessible to pathogens, allowing us to directly expose the cells to the parasite. Caco-2 epithelial tubes were exposed to approximately 8×10^7 transgenic mCherry-tagged *T. gondii* (type II ME49 strain) tachyzoites per tube. The lumen of the epithelial tube was washed with media 16h post-infection (hpi) to remove parasites that did not adhere to or invade the epithelium. Discrete and dense areas of parasites could be observed within a small proportion of epithelial cells using fluorescence microscopy at 24hpi and were largely contained within the boundaries of the epithelial tube, **Figure 4.3B**. The proportion of epithelial cells harboring the parasites increased between 24hpi and 48hpi and epithelial cell lysis was observed at 72hpi, **Figure 4.3C**, releasing tachyzoites into the lumen of the epithelium and the basal side of the epithelium. To confirm and quantify parasite replication, SAG1 (*T. gondii* surface antigen) gene expression levels were assessed at 24 hours and 48 hours via qPCR, **Figure 4.3D**. SAG1 expression analysis in the infected epithelium showed a 6-fold increase at 48hpi relative to 24hpi. Together, these results demonstrate that tubular intestinal epithelium generated in our human intestinal tissue MPS can support the invasion, replication, and translocation of *T. gondii* beyond the epithelium, which are key initial stages of the infection process prior to the encounter with innate immune cells.

4.2.4 Neutrophil Response to *T. gondii* Infection of the Intestinal Epithelium

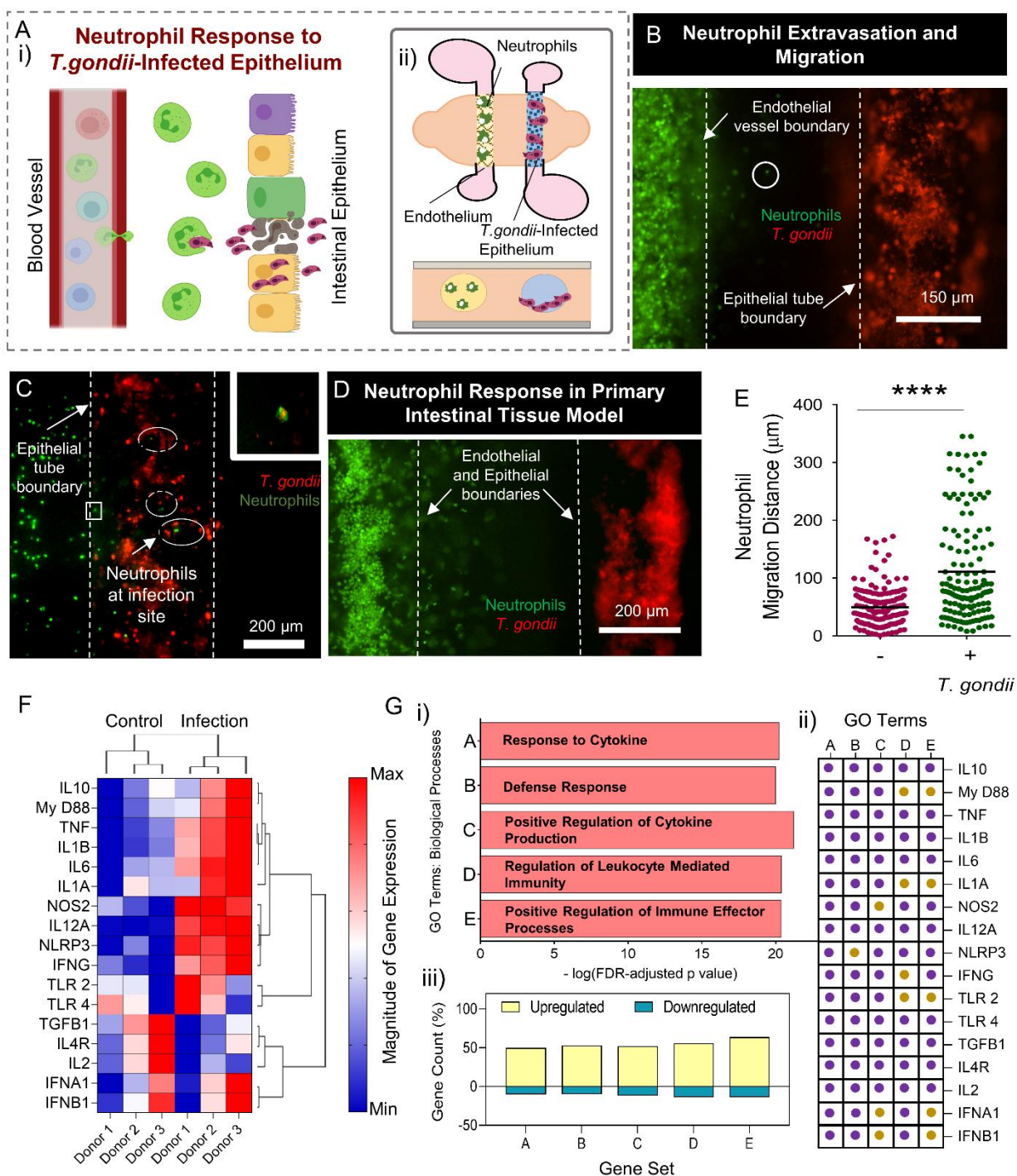


Figure 4.4 Neutrophil response to *T. gondii* infected epithelium. (A) Schematic depicting neutrophil trafficking and interaction with a *T. gondii*-infected intestinal epithelium as seen in vivo (i). Illustration representing the spatial distribution of components, a *T. gondii*-infected

intestinal epithelium, an endothelial vessel and neutrophils) used in the intestinal tissue MPS to explore neutrophil response. (ii). (B) Confocal image showing the interface between the gut epithelium and endothelium. Caco-2 epithelial tubes were infected with m-cherry tagged *T. gondii* for 48h before introducing neutrophils into the endothelial vessel. Neutrophils were seen to extravasate and migrate towards the infected epithelium. (C) Confocal image showing neutrophils trafficking to the infection site with some neutrophils interacting with the *T.gondii*-infected epithelium. White dotted circular lines highlight neutrophil co-localization with the infected epithelium. Inset shows co-localization of neutrophils with *T. gondii*. (D) Confocal image showing neutrophil extravasation and trafficking towards a *T. gondii*-infected epithelial tube generated from primary intestinal epithelial cells. Epithelial tubes were infected with m-cherry tagged *T. gondii* for 72 h before introducing neutrophils into the endothelial vessel. (E) Grouped scatter plot showing migration distance following extravasation of neutrophils towards *T.gondii*-infected primary intestinal epithelium. Each dot represents the migration distance of a single neutrophil from the endothelial vessel boundary (asterisk denotes P value of ≤ 0.0001). (F) Differential gene expression and hierarchical clustering analysis of 17 genes conducted in neutrophils from infected systems relative to control systems. Neutrophils from 3 nondiseased donors were used with gene expression profiles analyzed for each donor in control (without infection) and infected systems. Each cell in the matrix corresponds to the expression level of one gene in a sample. The intensity of the color from blue to red indicates the magnitude of differential expression (see color scale to the right of the image). The dendrograms at the top of the figures indicate relationship among experimental conditions which define clusters of conditions (control and infected). The dendrograms at the left of the figures indicate relationship among the profiles of the selected genes which define clusters of higher and lower expression in infected systems, after clustering analysis. Hierarchical clustering was conducted using average linkage clustering with Pearson correlation as the default distance metric. (G) Bar graph showing the top five most relevant GO terms associated with the 17 genes analyzed with their corresponding $-\log(\text{FDR-adjusted P value})$ (i). GO terms associated with each gene are highlighted with purple dots and genes not associated are highlighted with light dots (ii). The percentage of genes associated with each GO term according to their fold changes in expression (increase in yellow and decrease in blue) (iii).

Phagocytes involved in innate immunity (i.e., dendritic cells, macrophages, and neutrophils) are the first cells to encounter intracellular pathogens after they cross the epithelial barrier of the intestine¹⁷⁶. In mice, neutrophils are recruited in abundance to the sites of *T. gondii* infection and account for a high proportion of *T.gondii*-invaded-phagocytes in the small intestine following oral entry,¹⁵⁸ **Figure 4.4Ai**. However, little is known about how neutrophils traffic and behave at the gut-infection site, and data in mouse studies remain to be validated in human models. Therefore, to gain insight into the behavior and response of human neutrophils to *T. gondii* infection we employed our intestinal tissue MPS to assess neutrophil recruitment behavior to the infection site from

a neighboring blood vessel, **Figure 4.4Aii**. We infected Caco-2 intestinal epithelial tubes in our intestinal tissue MPS with ME49 tachyzoites for 48 h, as previously described, **Figure 4.3B**. Neutrophils isolated from healthy donor blood were introduced to the endothelial lumen of infected systems and observed for migration behavior over a course of 16h. Time-lapse imaging of the intestinal tissue MPS revealed neutrophils migrating within the endothelium and some events of transendothelial migration across the endothelium into the surrounding matrix towards the infected epithelium, **Figure B.3**. We observed increased neutrophil speed and displacement from the endothelium in our infected systems compared to uninfected controls, **Figure 4.4B**. Migrating neutrophils were also seen in the matrix near the infected epithelium, and some small fractions of neutrophils were observed within the lumen of the infected epithelium, **Figure 4.4C**. Confocal imaging also revealed the presence of fluorescently labeled neutrophils within the infected epithelium co-localized with mCherry-tagged ME49 tachyzoites, **Figure 4.4C (inset)**.

When we infected primary small intestinal epithelial cells within the intestinal tissue MPS, a similar increase in end-to-end displacement was observed compared to uninfected systems, **Figure 4.4D-E**. To directly examine the effects of *T. gondii* infection on gene transcription, we performed RT-qPCR analysis on neutrophils in our model with an infected and uninfected primary small intestinal epithelium. We selected 17 genes that are involved in establishing a protective immunity and activating immune effector functions against invading pathogens. Differential gene expression analysis revealed that infection of the intestinal epithelium with *T. gondii* indeed upregulates multiple

genes in neutrophils involved in innate immune responses, including IL10, MYD88, TNF, IL1B, IL6, IL1A, NOS2, IL12A, NLRP3, and IFN- γ , **Figure 4.4F**. We identified the 10 most significant Gene Ontology (GO) terms related to biological processes, **Table B.1**, based on the GSEA molecular signatures database (<http://www.gsea-msigdb.org/>). The five most relevant GO terms, **Figure 4.4G**, represent biological processes related to response to cytokines, defense response, positive regulation of cytokine production, regulation of leukocyte mediated immunity and positive regulation of immune effector functions, **Figure 4.4Gi**. The majority of the genes chosen in our study are involved in these biological processes, **Figure 4.4G ii** and the overall gene expression of each of these gene sets was generally upregulated in neutrophils from the infected systems, **Figure 4.4G iii**. These expression patterns suggest that biological processes such as defense response, regulation of leukocyte mediated immunity, and positive regulation of immune effector functions which are key functions of neutrophils during acute *T. gondii* infection are active in neutrophils from our infected systems. Together, these results show that infection of the intestinal epithelium with *T. gondii* in our intestinal tissue MPS elicits responses consistent with those observed *in vivo* behavior where increased transendothelial migration, trafficking of neutrophils towards the infection site, and activation of pathways involved in defense response to invading pathogens are observed.

4.2.5 IFN- γ Mediated Neutrophil Response to *T. gondii* Infection

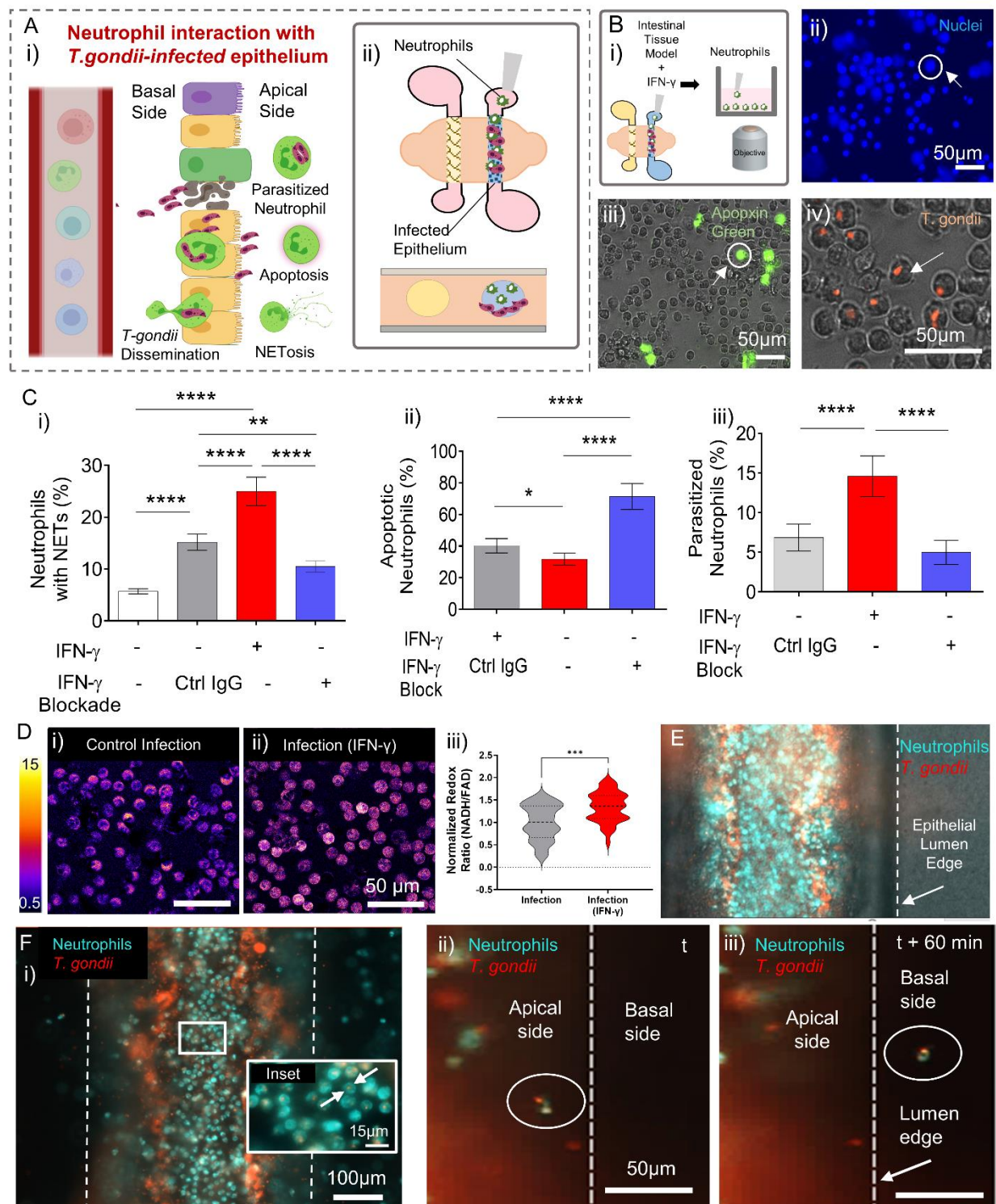


Figure 4.5 Neutrophil effector functions and contribution to *T. gondii* dissemination beyond the intestinal epithelium. (A) Schematic depicting in vivo responses of neutrophils at the site of *T. gondii*-infected intestinal epithelium (i). Illustration representing the spatial

distribution of components (neutrophils introduced directly into the *T.gondii*-infected intestinal epithelium) used in the intestinal tissue MPS to investigate neutrophil effector functions. (B) Caco-2 epithelial tubes were infected with m-cherry tagged *T. gondii* for 72h before introducing neutrophils into the lumen of the tube. Neutrophils were co-cultured with the infected epithelium for 6 h prior to collection in well plate and imaging (i). Immunofluorescence image showing neutrophils stained with Hoechst 33342 for DNA. White circular line highlights neutrophils with decondensed nuclei indicating or NET formation (ii). Combined brightfield and fluorescence image showing neutrophils stained with Apoptin Green (abcam) as indicator of cells undergoing apoptosis, white circle highlights an Apoptin Green positive neutrophil (iii). Combined brightfield and fluorescence image showing parasitized neutrophils, white arrow highlights a neutrophil directly interacting with a *T. gondii* parasite (iv). (C) Bar graphs showing percentage of neutrophils undergoing NET formation (i), apoptosis (ii) and parasitization (iii) in response IFN- γ stimulation and blockage. Values are presented as mean \pm SD of neutrophil response from 3 non diseased donors (asterisk denotes **** $p \leq 0.0001$, ** $p \leq 0.01$ and * $p \leq 0.05$). (D) Optical metabolic imaging was used to visualize intracellular NAD(P)H and FAD fluorescence intensities of neutrophils in infected systems without (i) and with IFN- γ stimulation (ii) [redox ratio = NAD(P)H intensity divided by FAD intensity]. Violin plots showing the analysis of neutrophil redox ratio based on NAD(P)H and FAD intensity (iii), (asterisk denotes *** $p \leq 0.001$). (E) Combined brightfield and fluorescence image showing neutrophils within a *T. gondii*-infected epithelium. (F) Fluorescence image showing some neutrophils with internalized *T. gondii* after 6h co-culture with infected epithelium(i). Fluorescence images showing *T. gondii* trafficking by neutrophils across the epithelial barrier, white dashed line indicates the epithelial boundary separating apical and basal surface (ii-ii).

In the context of *T. gondii* infection, IFN- γ is a cytokine that plays a major role in host resistance and is critical for coordinating protective immunity^{177–180}. IFN- γ mediates its protective effects by stimulating lysosomal activity¹⁸¹, inducing expression of nitric oxide synthase and effector genes¹⁸², and modulating metabolic activity¹⁸³ in phagocytes. Neutrophils, upon infiltration to the site of infection, execute a broad range of immune effector functions which include phagocytosis, production of reactive oxygen species (ROS) or antimicrobial peptides, and activation of programmed cell death pathways to reduce the pathogen's chances of survival^{184,185} **Figure 4.5Ai**. Here, we investigate the influence of stimulation and inhibition of IFN- γ on the effector functions and metabolic activity of neutrophils following an encounter with a *T. gondii* infected epithelium. To evaluate this, we generated tubular epithelium with Caco-2 cells, infected them with *T. gondii* tachyzoites, as previously described, and introduced primary human neutrophils

into the lumen of the epithelium, **Figure 4.5Aii**. As *T. gondii* is an intracellular pathogen, we infected the apical side of the Caco-2 epithelium and allowed incubation for 72 h, with consistent media replenishment, which resulted in some epithelial cells undergoing cell lysis and exposing *T. gondii* to the luminal contents (**Figure 4.3C**). Neutrophils, isolated from healthy donor blood, were then added into the epithelial lumen to maximize encounter probability with *T. gondii*, and co-cultured for 6h prior to collection and assessment **Figure 4.5Bi**. Neutrophil extracellular trap (NET) formation, apoptosis and parasitization of neutrophils were examined, **Figure 4.5Bii to iv and Figure B.4**. We first examined and quantified the fraction of neutrophils undergoing NET formation, which are released from neutrophils in response to invading pathogens. A key step in NET formation is the release of antimicrobial DNA complexes into the cytosol of the cell. As such, the measurement of decondensed nuclei has been a recognized method for quantifying neutrophils undergoing NET formation¹⁸⁶. We used Hoechst nuclear stain to distinguish between intact and decondensed nuclei, where intact was characterized by normal trilobed nuclei and decondensed was characterized by diffuse staining with large nuclear area, **Figure 4.5Ci**. Neutrophils were stained with Hoechst prior to introduction into the lumen of *T.gondii* infected epithelium and removed after 6h for analysis. IFN- γ stimulation significantly increased the fraction of neutrophils undergoing NET formation compared to control infection. Conversely, blocking IFN- γ significantly decreased the fraction of NET-forming neutrophils relative to IgG controls, unstimulated controls, and IFN- γ stimulated systems. To evaluate the influence of IFN- γ on apoptotic cell death, we examined the induction of apoptosis using a caspase 3/7 activity assay. Our results indicate that blocking IFN- γ significantly triggered apoptosis while IFN- γ stimulation

slightly but not significantly suppressed it, **Figure 4.5Cii**. We then examined the effects of IFN- γ on the fraction of *T. gondii* parasitized neutrophils. To eliminate parasites non in contact with neutrophils from analysis, neutrophils collected from the epithelium were resuspended in culture medium and centrifuged at 200g for 3 min prior to imaging. Consistent with the trends observed with NET formation, IFN- γ stimulation significantly increased the fraction of *T. gondii* parasitized neutrophils relative to unstimulated systems, **Figure 4.5Ciii**. Blocking IFN- γ decreased the fraction of *T. gondii* parasitized neutrophils compared to IFN-stimulated systems, demonstrating the sensitivity of neutrophils to IFN- γ stimulation.

We also investigated the influence of IFN- γ on neutrophil metabolic activity by means of optical metabolic imaging, which quantifies relative amounts of NAD(P)H and FAD^{187,188}, and by extension the redox ratio. The optical redox ratio is used to obtain information on the dynamic changes in oxidation-reduction rates in cells and is sensitive to alterations in cellular metabolic rates¹⁸⁷. Optical NAD(P)H/FAD redox ratios increased in neutrophils after 6h in our IFN- γ stimulated systems indicating increased metabolic activity, **Figure 4.5D**, and these observations were conserved when the analysis was limited to *T. gondii* internalized neutrophils, **Figure B.5**. Relative to unstimulated systems, lower FAD intensity was observed in response to IFN- γ stimulation. Altogether, these findings suggest that neutrophil effector functions are IFN- γ -dependent where IFN- γ stimulation enhances neutrophil effector functions by increasing events of *T.gondii* internalization, NET formation, and cellular metabolic activity of neutrophils while prolonging their life span. More importantly, these results

demonstrate the utility of our intestinal tissue MPS in testing the sensitivity of immune cells to stimulants that may influence their response to pathogens.

Following an encounter at the infection site, engulfed microbes are carried by migratory phagocytes such as macrophages and neutrophils beyond the epithelia of barrier organs into deeper tissue and draining lymph nodes, contributing to pathogen dissemination to other organs,¹⁸⁹ **Figure 4.5A**. In *T. gondii* infected mice, parasite-containing neutrophils in the small intestine have been shown to transport the parasite across epithelial barriers to facilitate parasite spread both within the intestine to other regions and beyond to the spleen and mesenteric lymph nodes^{158,190,191}. To investigate whether dissemination of *T. gondii* by migratory neutrophils beyond the epithelium could be observed in our intestinal tissue MPS, we introduced neutrophils into an infected intestinal epithelium generated from Caco-2 cells **Figure 4.5E**. Within 6 hours, *T. gondii* containing neutrophils could be seen within the lumen of the intestinal epithelium, **Figure 4.5Fi**. Time course imaging revealed translocation of *T. gondii* containing neutrophils from the apical side to the basal side of the epithelium, **Figure 4.5Fii and iii**. These results show that our intestinal tissue MPS can recapitulate the mechanisms of parasite dissemination by migratory phagocytes as seen *in vivo*. Furthermore, our ability to visualize immune cell-mediated transport of pathogens within our intestinal tissue MPS could provide valuable insight into how intracellular pathogens disseminate and present opportunities to investigate new targets for therapeutic intervention.

4.2.6 Innate Immune Cell Response to Parasite Invasion and Replication In The Intestinal Epithelium

The innate immune system coordinates the first immunological defense against an invading pathogen ¹⁹². As cytokine production by intestinal epithelial and endothelial cells is a key feature of early host immune response, we wanted to evaluate the capacity of our intestinal tissue MPS to produce the inflammatory mediators required for immune effector functions in response to parasite invasion, **Figure 4.6A**. We analyzed inflammatory cytokines secreted in culture media prior to the addition of immune cells using a Luminex multiplex bead-based ELISA assay. Our results revealed that infection of the primary small intestinal epithelium with *T. gondii* induced significantly higher levels of proinflammatory cytokines/chemokines MCP-1, MIP-1 α , IL-1 α , IL-1 β , GM-CSF, IL-6, and IL-8 secretion in culture media at 48 hpi compared to uninfected controls, **Figure 4.6B**. Secretion of anti-inflammatory cytokines such as IL-4, IL-10, and IL-13 on the other hand showed no change in the infected systems compared to control uninfected systems. Together, these cytokines make up critical components of the inflammatory milieu that contribute to coordinated immune defenses like immune cell trafficking, activation, and effector functions against parasites during acute infection.

Adhesion molecules on endothelial cells are known to mediate leukocyte rolling, adhesion, and subsequent transendothelial migration as part of an inflammatory response to injury or infection. We investigated the effects of infection on the firm adhesion of immune cells to the endothelium. Fluorescently labeled primary human peripheral blood mononuclear cells (PBMCs) were added to the endothelium 48 hpi with

ME49 *T. gondii* and washed away after 2 hours to evaluate endothelial adhesion of immune cells, **Figure 4.6C**. Indeed, the percentage of PBMC adhering to the endothelium doubled relative to systems without infection, **Figure 4.6D**. A similar increase in endothelial adhesion was also observed when NK-92 cells were added to the endothelial vessel, **Figure 4.6D and Figure B.6A**. Overall, these results provide strong evidence of epithelial-endothelial crosstalk during parasite infection that promotes immune cell adhesion to endothelium, a critical step in endothelial transmigration and recruitment of immune cells to the infection site. Concurrent with the high levels of proinflammatory cytokines observed in our system, increased levels of soluble adhesion molecules, sP-selectin, sICAM-1, and sE-selectin were also found in the culture media of infected systems, **Figure B.6B**.

Before adaptive immunity is established, NK cells restrain the spread of infection by secreting inflammatory cytokines that are critical for stimulating protective immunity¹⁹³. To explore NK cell-mediated production of cytokines in our *T. gondii* infected intestinal tissue MPS, we compared cytokine secretions in infected systems in the presence and absence of NK cells. NK-92 cells were introduced in the endothelial lumen of infected systems at 48 hpi and cultured for 24 hours, **Figure 4.6E**. Secreted factor analysis was performed on media collected from systems 24 hours after the introduction of NK cells into the lumen of the endothelium. Our results show that the presence of NK cells in infected systems led to significantly higher levels of pro-inflammatory factors including IFN- α , IL12p70, TNF- α , IP-10, IL-17a, MIP-1 α , MIP-1 β , and IFN- γ , **Figure 4.6F**. The presence of NK cells in infected systems also induced significantly higher secretion of

IL-10, IL-4, and IL-13 which are known to suppress pro-inflammatory cytokine production. While the induction of a robust inflammatory response is critical for host resistance against *T. gondii*, unregulated inflammation can result in exacerbated immunopathological reactions causing tissue damage. Thus, anti-inflammatory factors may have critical roles in reducing inflammatory reactions and suppressing collateral damage because of upregulated inflammation during parasite infection.

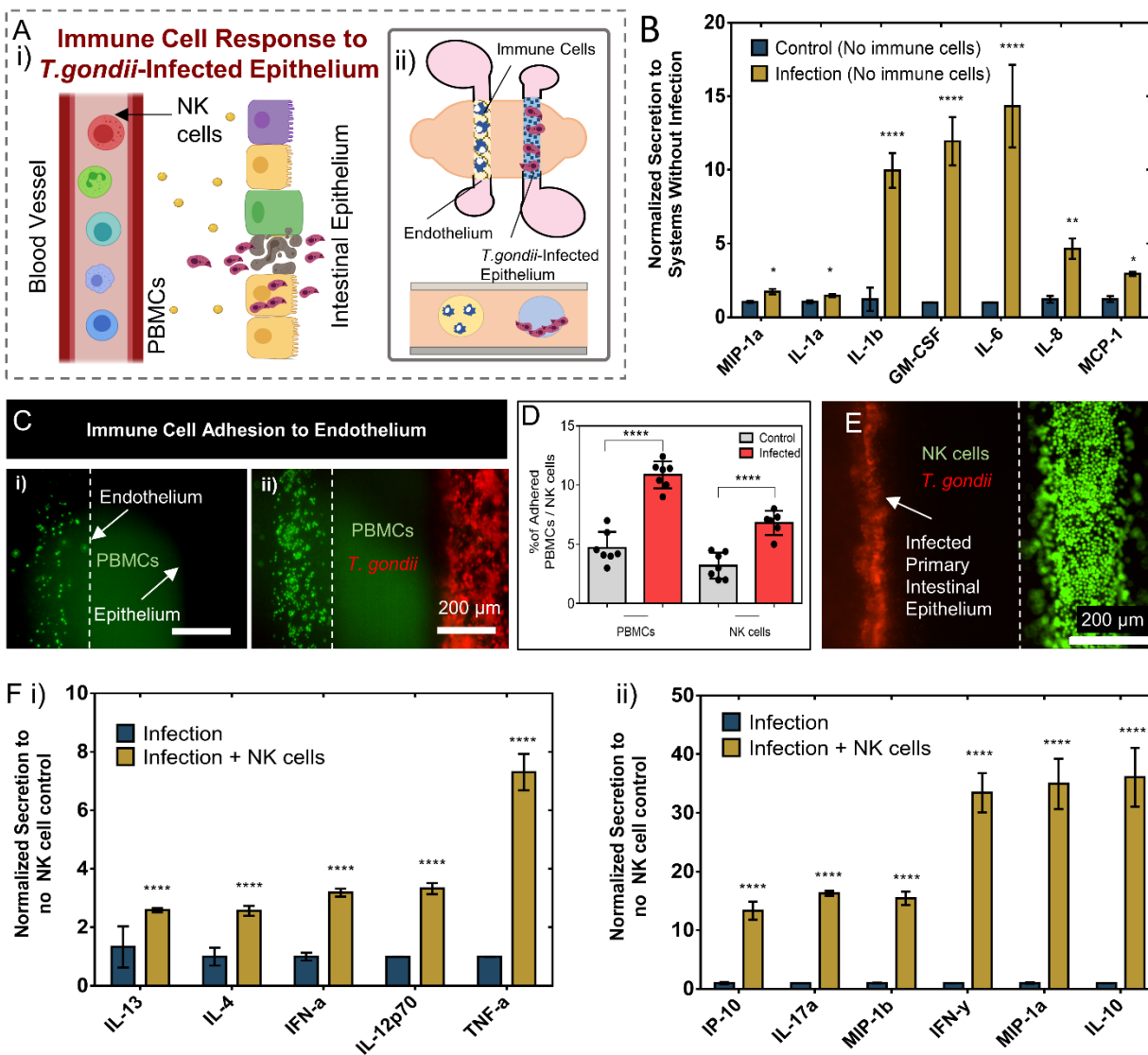


Figure 4.6 Immune cell response and cytokine secretions within the intestinal tissue MPS. (A) Schematic conceptualization of immune cell response to soluble factor signaling during the initial stages of *T. gondii*-infection (i). Illustration representing the spatial distribution of components (*T. gondii*-infected intestinal epithelium, endothelial vessel, PBMCs or NK cells) used in the intestinal tissue MPS to investigate immune response. (B) Cytokine concentrations measured in media collected from the intestinal tissue MPS consisting of endothelial vessel and primary intestinal epithelial tubes infected with *T. gondii* normalized to control, uninfected systems (asterisk denotes **** $p \leq 0.0001$, ** $p \leq 0.01$ and * $p \leq 0.05$). (C) Fluorescence image showing differences in PBMC adhesion events to the endothelial vessel in control (i) and infected (ii), Caco-2 epithelium. (D) Bar graphs showing percentage of PBMCs and NK cells adhering to the endothelium of control and infected systems following co-culture for 2h. PBMCs and NK cells were added to the lumen of the endothelial vessel after Caco-2 epithelial infection by *T. gondii* for 48h. Five devices were prepared on two different days for each condition. (E) Fluorescence image showing *T. gondii*-infected primary intestinal epithelial tube in co-culture

with an endothelial vessel containing NK cells. Epithelial tubes were infected for 72h prior to adding NK cells into the endothelial vessel. (F) Cytokine concentrations measured in media collected from infected intestinal tissue MPS consisting of an endothelial vessel, NK cells and primary intestinal epithelial tubes infected with *T. gondii* normalized to infected systems without NK cells. In all cytokine measurement experiments nine devices were prepared on two different days for each paired conditions (infected vs. control, and infection in the absence vs. presence of NK cells), media from three devices were pooled to make one replicate. Values are presented as mean \pm SD asterisk denotes **** $p \leq 0.0001$).

4.3 Discussion

Development of improved treatment strategies against parasitic infections requires increased knowledge of the pathogen-tissue-immune system interactions. Murine models have made substantial contributions to our understanding of innate immunity against parasitic infections, but sufficient differences in the organization of the immune system between humans and mice warrant the need for improved models. Therefore, the development of new tools that allow researchers to elucidate mechanisms involved in immune responses and defense strategies against parasites and other activators of the immune system in humans could accelerate the development of antiparasitic drugs and therapeutic strategies. In this regard, we have bioengineered an integrated microphysiological system of the intestinal tissue for exploring human innate immune cell responses to parasite infection in the gut. Tubular tissue structures like the intestines and the vasculature system serve essential roles in separation of internal contents and pathogenic microbes in the intestinal lumen from systemic dissemination. Our human intestinal tissue MPS incorporates *in vivo*-like tubular geometries of the intestinal epithelium and endothelium allowing us to explore host-parasite interactions and tissue-dissemination that occur during the initial stages of infection. Using our

model, we examined epithelial infection by *T. gondii*, an intracellular parasite that initially infects the small intestine following ingestion. We introduced a suspension of *T. gondii* tachyzoites directly onto the apical surface of the intestinal tubes and using live-cell microscopy we demonstrated that our tubular intestinal epithelium supports invasion and intracellular replication of *T. gondii*. As an important component of the intestinal immune network, the innate immune system is considered the most important defense line against pathogens breaching the epithelial barrier and plays a pivotal role in maintaining immunity and preventing tissue dissemination through the vascular system. Although incorporating tubular intestinal epithelium within scaffolding matrices has previously been reported ^{145,147,161}, the originality of our model relies on the integration of vascular and immune cell components. This enables us to investigate the various facets of innate immune cell responses, including extravasation and trafficking, to *T. gondii* infection of the intestinal epithelium and its translocation across the epithelial barrier. One additional design aspect of our system is the compatibility with live-cell microscopy enabling dynamic visualization of host-microbe interactions occurring at the interface between the intestinal epithelium and the neighboring vasculature at high spatiotemporal resolution. Using these techniques and molecular analysis, we examined early responses from human innate immune cells like neutrophils and NK cells and investigated parasite-immune cell interactions during epithelial infection that influence immune effector functions and tissue dissemination.

Current *in vitro* studies of parasitic infections primarily rely on human cell lines that often do not recapitulate *in vivo* phenotypes. On the other hand, maintaining long-term

proliferative cultures of the human intestinal epithelium *in vitro* have met with continuing difficulty due to the complex interactions between cell types and the presence of molecular signaling required for stem cell maintenance. Organoid technologies enable the expansion of primary intestinal stem cells and are regarded as a powerful *in vitro* tool for modeling intestinal epithelial tissue due to their structural and functional resemblance to *in vivo* tissue ^{194–196}. While apical access can sometimes be limited when using these techniques, methods to form epithelial monolayers from intestinal organoid fragments have been reported ^{197–199}, where the major epithelial cell types found in 3D organoids are retained when cultured on hard surfaces coated with Matrigel or collagen ²⁰⁰. Building on these methods, here we adapted our intestinal tissue MPS to integrate the formation of tubular epithelium using primary human intestinal epithelial cells.

We used a simple micromolding based technique to generate tubular structures within a hybrid matrix, composed of type I collagen, type IV collagen, and Matrigel. Our data indicates this matrix-supported culture and differentiation of human intestinal epithelial cells, both cell lines (e.g., Caco-2) and primary organoid-derived intestinal stem cells obtained from jejunal tissue resections. Maintenance of primary human-patient derived small intestinal cells also require stimulation from the basal compartment by niche factors that help retain stem cell components while supporting differentiated enterocyte-goblet cell function ^{165,195}. To support the integration of the endothelial vessel and immune cells (i.e., neutrophils, NK cells, and PBMCs) into our systems, we optimized culture protocols and media compositions for differentiating a primary intestinal

epithelium and to support all cell types within the intestinal tissue MPS. Although several molecular and functional properties of the intestinal epithelium within the system are expected to change due to constantly evolving differentiation states and influence from co-culture with other cell types, we confirmed through visual inspection of the system the epithelium and endothelium remain intact. Further, we show that phenotypic characteristics and barrier properties of both the epithelium and endothelium are retained for the duration of the experiments (5 days post endothelial cell seeding), which correlates with the turnover of intestinal epithelia *in vivo*²⁰¹. Intestinal tubes generated within the hybrid matrix, both from the Caco-2 cell line and primary intestinal stem cells, exhibited key properties of the intestinal epithelium including a polarized epithelium expressing markers of tight junctions, goblet cells, and microvilli formation. Interestingly, gene expression analysis showed that expansion of primary intestinal stem cells in tubular structures resulted in increased maturation and differentiation, while retaining key characteristic features of the jejunal epithelium compared to primary epithelial monolayer formed in transwells. Gene expression analysis also demonstrated upregulation of pathways involved in gut epithelium regeneration compared to transwell cultures. These results agree with previous reports showing that a suitable matrix with relevant ECM proteins and biophysical properties are key factors in providing physical support and facilitating the differentiation of intestinal stem cells¹⁷³.

By integrating blood vessels, circulating innate immune cells, and primary intestinal epithelial cells within a biomimetic 3D scaffolding matrix, we incorporated key cellular components and relevant cell-ECM interactions of the intestinal tissue for improved

modeling of parasite interaction with the diverse cell types of the epithelium and immune cell responses during epithelial infection. However, one limitation in this work is that we did not incorporate components of the microbiome that can also impact the mechanisms of parasite interaction with the epithelium and innate immune cells. This would require additional control over environmental factors such as oxygen levels to accommodate oxygen-sensitive species of the microbiome. Future studies could incorporate this layer of complexity by incubating the intestinal tissue MPS in a hypoxia incubator (i.e., 1% O₂) and perfusing oxygenated medium through the vascular lumen.

Initial responses against *T. gondii* are managed by innate immune cells, with neutrophils, dendritic cells, and monocytes playing a central role^{132,202,203}. Early depletion studies in mice using monoclonal antibodies showed that neutrophils are important for host survival during acute infection²⁰⁴. Further highlighting their importance, depletion of neutrophils showed decreased levels of gamma interferon (IFN- γ), interleukin-12 (IL-12), and tumor necrosis factor (TNF), indicative of a weaker type I immune response, and development of lesions in multiple organs including lung, liver, and brain. Using our intestinal tissue MPS, we recapitulated events with human neutrophils including extravasation and migration towards the *T. gondii* infected epithelium, reminiscent of the process of leukocyte trafficking to the site of infection previously observed in mouse models¹⁵⁸. To reduce donor-to-donor variability from adult intestinal stem cells, we used organoid-derived stem cells from a single donor for generating tubular intestinal epithelium, however, neutrophils from multiple blood donors were used to capture responses from neutrophils in this study. Our results showed that

the interaction of *T. gondii* infected primary small intestinal epithelium with neutrophils led to increased expression of genes involved in biological processes including response to cytokines, defense response, positive regulation of cytokine production, regulation of leukocyte mediated immunity, and positive regulation of immune effector functions. However, in this work, we used RT-qPCR to analyze ≈ 17 genes related to neutrophil response, which only represents a fraction of the total number of alterations involved in establishing this immune response. Future investigations could include RNA-sequencing to provide a more in-depth molecular analysis of the biological processes activated in neutrophils in response to *T. gondii* infection in our model. On the other hand, our study also highlighted changes in the functional behavior of neutrophils that correlate with the biological process involved as determined by gene expression analysis. In line with the transcriptional changes observed, dynamic visualization of neutrophil behavior at the epithelial and vascular interface showed increased migration speed and end-to-end displacement from the endothelium in response to the infection of the epithelium. Strikingly, some instances of direct interaction between neutrophils and excysted *T. gondii* within and near the epithelium could also be observed, demonstrating the capability of our model in capturing parasite invasion, replication, and initial response of neutrophils in the same experiment.

Host-directed therapies that target signaling pathways for parasite clearance bypass many problems encountered by anti-parasitic drugs including poor patient compliance and the emergence of drug-resistance parasites²⁰⁵. By targeting host pathways that are redundant in the host but are critical for parasite survival, there is a reduced chance of

developing treatment resistance due to the slow rates of mutations in molecules and processes in the host relative to parasites. In this work, we examined the effects of a host-targeted pathway on the effector functions of neutrophils. Once at the site of infection, local production of inflammatory mediators regulates intercellular communication that mobilizes several defense mechanisms in tissue-resident cells and immune cells ²⁰⁶. IFN- γ has a multitude of immunomodulatory functions and is considered one of the most potent pleiotropic cytokines ^{179,180,207}. IFN- γ interactions with T cells, NK cells and activated macrophages have been widely researched, however, investigations into the role of IFN- γ during the initial responses of neutrophils and other innate immune cells to infection by parasites have been limited. We demonstrated the influence of IFN- γ on traditional neutrophil functions including parasitization, NET formation, and apoptosis of neutrophils. IFN- γ treatment favorably affected neutrophil functions with increased parasitization, NET formation, and overall metabolic activity in neutrophils. In contrast, neutrophil apoptosis, the process of programmed cell death, decreased which limits exposure of destructive neutrophil productions to surrounding tissue. IFN- γ blockage reversed these trends, further highlighting the importance of IFN- γ on traditional neutrophil functions of anti-microbial activities and showing the utility of our model for investigation of human immune responses. We also demonstrate the ability of our model to investigate parasite dissemination facilitated by neutrophils, both within the lumen of the intestinal epithelium and beyond by crossing the epithelial wall into the surrounding tissue. These observations are also consistent with data in mice that show the involvement of neutrophils in the spread of *T. gondii* infection with the intestinal tissue ¹⁵⁸. Altogether,

we demonstrate the sensitivity of our system in capturing the changes in various effector functions and antimicrobial activity of neutrophils in response to inflammatory stimulus and blockage.

Our secreted factor analysis revealed that our intestinal tissue MPS produces a wide array of proinflammatory cytokines/chemokines (MCP-1, MIP-1 α , IL-1 α , IL-1 β , GM-CSF, IL-6, and IL-8) that enhance and activate defense mechanisms in innate immune cells during *T. gondii* infection. In mice, these factors are known to have immunoregulatory roles during acute infection. For instance, the production of MCP-1 and MIP-1 α in our system is consistent with *in vivo* data in mice showing higher expression of these chemokines in *T. gondii* infected intestinal epithelial cells ²⁰⁸. Also, mice deficient in MCP-1 and its chemokine receptor CCR2 fail to generate adequate immune response during acute *T. gondii* infection ²⁰⁹, highlighting its critical role in regulating innate immunity. Elevated levels of IL-1 α and IL-1 β have been previously observed in the serum of *T. gondii* infected mice (one-week post-infection) and are known inflammatory mediators/regulators of host tissue homeostasis during acute infection ^{210,211}. Moreover, aside from their involvement in inflammation, chemokines like GM-CSF, IL-6, and IL-8 play important roles in the recruitment and enhanced survival of phagocytic cells like neutrophils during acute innate response to *T. gondii* infection ^{212–214}. Together, these cytokines make up critical components of the inflammatory milieu that contribute to coordinated immune defenses like immune cell trafficking, activation, and effector functions against parasites during acute infection. In accordance with the increased levels of these cytokines in our infected systems, we observed increased neutrophil

trafficking and transcriptional changes associated with responses to cytokines and positive regulation of immune effector functions in neutrophils. While we have not explored the direct influence of these cytokines on the functional behavior of neutrophils, future studies using our model could explore spatial and temporal relationships between neutrophils and infection-derived factors that enhance their overall effector functions against parasites.

During innate immune responses, *T. gondii* infection-induced production of inflammatory cytokines, drive NK cells to produce a host of factors such as IFN- γ and TNF- α that amplify effector functions and inflammatory responses driven by other innate immune cells ²¹⁵. Intriguingly, NK cell production of immunosuppressive cytokines that counterbalance inflammatory responses during disseminated pathogenic infection with *T. gondii* have also been found ²¹⁶, shedding light on the role of NK cells in facilitating immunoregulation. While the mechanisms haven't been clearly defined, the immunoregulatory roles of NK cells are likely important for preventing inflammation-dependent pathology during parasite infection. Further exploration of secreted factor analysis shows that incorporating NK cells into our systems upregulates several immunoregulatory signaling factors critical for amplifying the production of inflammatory and enhancing effector functions in other innate immune cells. In the presence of NK cells, several cytokines were uniquely elevated IFN- α , TNF- α , IFN- γ , IL-17a, IP-10, IL-4, IL-13, IL-12p70, and IL-10 in our infected systems. IFN- α , a member of the type I interferon family, has recently been shown to enhanced cytokine secretion and cytotoxic potential in NK cells ²¹⁷, and TNF- α together with IFN- γ are major proinflammatory

cytokines produced by NK cells as means of host protection against *T. gondii* ¹⁶⁰. Moreover, these two cytokines are recognized as essential immune effectors against intracellular pathogens. IL-17 has been implicated in resistance to *T. gondii* where IL-17R^{-/-} mice showed defects in neutrophil recruitment and increased parasite burden ²¹⁸. As NK cells are often considered to function at the interface of the innate and adaptive immune response ²¹⁹, NK cell production of chemokine, IP-10, can be critical for generating an adaptive immune response and influencing the recruitment of effector T cells to the *T. gondii* infection site ²²⁰. Interestingly, cytokines typically involved in the resolution of cell-mediated inflammation (IL-4, IL-13, and IL-10 ²²¹) were also elevated in our infected systems with NK cells. Conventionally, IL-4 and IL-13 are thought to counter NK cell effector functions by limiting the production of IL-12. However, recent work shows that stimulation with IL-4 or IL-13 enhances TNF- α and IFN- γ production in NK cells in the presence of IL-12, underscoring the immunoregulatory roles of these cytokines ²²². Elevated IL-10 levels observed are also in line with previous reports showing that NK cells produce IL-10 during acute *T. gondii* infection which interferes with the activation of the adaptive immune responses ²²³, further highlighting the immunoregulatory roles of NK cells. While the source of these cytokines is unclear in our analysis, secretion of these factors is markedly higher in our infected intestinal tissue MPS with NK cells, indicating a direct or indirect contribution from NK cells. The local effects of this inflammatory environment on the effector functions of neutrophils and other innate immune cells may be tested with future experiments within our platform and using tools/methods for examining complex interactions *in vitro*.

Collectively, our secreted factor analysis demonstrated a wide array of immunoregulatory cytokines, chemokines, and adhesion molecules generated within our primary intestinal tissue MPS during *T. gondii* infection, which are essential for generating a robust immune response. These molecules are critically involved in innate immunity against intracellular pathogens in the following ways: 1) promoting leukocyte adhesion to the endothelium and transendothelial migration, 2) trafficking, recruitment, and survival of phagocytic cells, and 3) enhanced activation, cytotoxic activity, and effector functions of immune cells involved in the innate and adaptive immune responses. These data confirm the presence of an immunomodulatory cytokine milieu that can support mounting a strong immune response to parasitic infections.

The primary objective of this work was to create a microphysiological system that recapitulates complex interactions between key components of the human intestinal tissue and to demonstrate its usefulness in studying innate immune responses to parasitic infection. Recreating the initial stages of parasitic infection by *T. gondii* and the accompanying innate immune response of the intestinal tissue highlights the potential of our microphysiological model to fill the gaps in studying human tissue responses through mechanistic correlations between various molecular and functional cell data to both animal and human clinical data. The readily accessible approach to generating 3D geometries of tubular organs within biomimetic ECM scaffolds, which accommodate the development and maturation of stem cells, and enables dynamic visualization of host-microbe interactions at a high spatiotemporal resolution, could answer questions that

have so far been difficult to address and may have substantial potential for discovery of cell-mediated immune responses and development of host-directed therapies.

4.4 Materials and Methods

4.4.1 Intestinal Tissue MPS Fabrication and Assembly

The intestinal tissue MPS was fabricated using the LumeNEXT approach as previously reported⁶⁶. Briefly, this approach uses a micromolding technique to fabricate one or more lumen structures with variable size, configuration and lumen spacing controlled by micromold design in soft lithography. Here, we use a two-lumen setup, each having a separate inlet and outlet port within a single chamber was used accompanied by perpendicularly oriented side ports. Two stacked PDMS layers, with microscale features patterned into them, formed the culture chambers in which scaffolding ECM gel can be loaded, while removable PDMS rods formed the hollow lumen structures surrounded by the ECM gel. The master molds for the PDMS layers were made using SU-8 100 (Microchem) which were spin-coated onto wafers, soft-baked (i.e., heat at 65°C for 30-40 min and then at 95°C for 90-120 min depending on layer thickness), exposed to UV through a mask of desired patterns and post-baked at 95 °C for 20-30 min. This procedure was repeated for additional layers prior to development in propylene glycol monomethyl ether acetate (Millipore Sigma). After developing, PDMS (Sylgard 184 Silicon Elastomer Kit, Dow Corning Corporation) was applied to the masters at a ratio of 10:1 base to curing agent and allowed to polymerize for 4 h at 80 °C. The rods were drawn from needles with gauge size, 23 gauge ($\approx 340 \mu\text{m}$ inner diameter). Prior to device assembly, the PDMS layers and rods were soaked in 100% ethanol for several

days to extract any uncured PDMS oligomers. Following PDMS extraction, the rods were placed in between two layers, across the body of the chamber (≈ 3 mm in length) in ledge features stemming from the smaller inlet and larger outlet ports to hold the rods in the middle of the chamber. The side ports (≈ 4 mm apart) of the chamber were used to fill the chamber with ECM gel and the height of the chamber was about (≈ 1.25 mm). Once assembled, the PDMS layers were oxygen-plasma bonded onto a glass-bottom MatTek dish using a Diener Electronic Femto Plasma Surface System.

4.4.2 ECM Gel Preparation and Loading

The bonded devices were UV sterilized for 20 min and moved to the biosafety cabinet, prior to ECM gel loading. To promote matrix adhesion to PDMS, the device chambers were treated with 1% polyethylenimine (Millipore Sigma) in DI water solution for 10 min, followed by a 30 min treatment of 0.1% glutaraldehyde (Millipore Sigma) in DI water solution. Following surface treatment, devices were flushed with DI water solution 5 times to remove excess glutaraldehyde. A high concentration rat tail collagen I (Col-I) (Corning) neutralized with 0.5N sodium hydroxide (Fisher Scientific), was mixed with 7.5 pH 5X phosphate buffered saline (PBS), complete growth medium or organoid expansion medium, human placental type IV collagen (Col-IV) and Matrigel to achieve a final ECM solution containing 4 mg/mL Col-I, 15% Matrigel and 50 μ g/mL Col-IV. The pH of the ECM mix was adjusted to 7.2 pH prior to loading the mix into the gel-chamber of the device. The devices were first kept at room temperature for 20 min then moved to an incubator at 37°C for at least 1 h prior to cell loading. To prevent dehydration during polymerization, PBS was added to the MatTek dish surrounding the devices. PDMS

rods were then removed leaving behind hollow tubular structures within the ECM gel which can be lined with cells.

4.4.3 Crypt Isolation and Gut Organoid Culture

Small intestinal crypts were isolated using a previously established protocol.²²⁴ from jejunal tissue resection samples removed from nondiseased tissue of de-identified individuals²²⁴. Jejunal tissue resections were performed at University of Wisconsin-Madison upon the donors' informed consent and methods were carried out in accordance with Institutional Review Board (IRB) (Protocol# 2016-0934). Small intestinal organoids were established from isolated crypts by resuspending in Matrigel (Corning; growth-factor-reduced, phenol-red-free formulation), and culturing in 24-well plates (Polystyrene, Nunc, Non-Treated Multidishes, Thermo Fisher Scientific) at 37°C in the organoid expansion media. Expansion medium consisted of a mixture of base medium (BM;45%v/v), L-WRN conditioned medium (CM;45%v/v), supplement mix, 1x Primocin (InvivoGen) and 10% heat-inactivated fetal bovine serum (FBS; Millipore Sigma). BM was prepared from Advanced Dulbecco's modified Eagle's medium (DMEM)/F12 (Thermo Fisher Scientific) supplemented with Glutamax (2 mM; Thermo Fisher Scientific), Hepes (10 mM; Thermo Fisher Scientific), penicillin/streptomycin (Pen/Strep) (Thermo Fisher Scientific), B-27 Supplement (Thermo Fisher Scientific), N2 supplement (Thermo Fisher Scientific) and 1% cell-culture grade bovine serum albumin (BSA). L-WRN CM was prepared using L-WRN cells from American Type Culture Collection (ATCC, catalog no. CRL-3276) and a previously published protocol ²²⁵. The supplement mix consisted of EGF (50 ng ml⁻¹; Peprotech), N2 supplement (Thermo

Fisher Scientific), human [Leu15]-gastrin I (10 nM; Millipore Sigma), N-acetyl cysteine (500 μ M; Millipore Sigma), nicotinamide (10 mM; Thermo Fisher Scientific), A83-01 (500 nM; Tocris), SB202190 (10 μ M; Selleckchem), prostaglandin E2 (10 nM; Tocris), Y-27632 (10 μ M; Selleckchem) and CHIR99021 (5 μ M; Tocris). Jejunal organoids were split every 7 to 9 days as previously described.²²⁶ Based on this established protocol, Matrigel plugs containing organoids were digested in 0.5 μ M ethylenediaminetetraacetic acid (EDTA; Invitrogen) and collected. After centrifugation at room temperature for 3 min at 300 \times g, supernatant was removed followed by incubation in trypsin (Sigma Aldrich) for 2 min at 37 °C. Trypsin was neutralized using Advanced DMEM/F12 supplemented with 20% FBS and 1% Pen/Strep followed by mechanical dissociation of organoids by vigorous pipetting (about 30 times) to make small organoid fragments. After centrifugation at room temperature for 3 min at 300 \times g, pellets were reconstituted in 50:50 mix of fresh Matrigel and expansion medium at 1:3 to 1:4 ratio and cast in 25- μ L droplets in 24-well plate. Matrigel droplets containing organoid fragments were then polymerized for 15 min at 37 °C before adding 500 μ L expansion media to each well. Expansion media was changed every 2 to 3 days and organoids were used between passage 5 - 25. Y-27632 was only used for the first 48 h after single-cell dissociation to prevent detachment-induced cell apoptosis.

4.4.4 Caco-2 Epithelial Tube Formation

Caco-2 cell line was acquired from the ATCC and maintained in Eagle's Minimum Essential Medium (EMEM, Millipore Sigma) supplemented with 20% FBS and 1% Pen/Strep. To generate tubular epithelium, Caco-2 cells were detached using a

trypsin/EDTA solution and resuspended at 17 million cells per mL of supplemented EMEM. After removal of the PDMS rod 3 μ L of cell suspension was introduced into the hollow tubes through the inlet ports and cells were allowed to fill the lumen structures by passive-pumping. The microdevice was rotated every 30 min over a 2-hour period using a previously described method⁶⁶ to line the hollow tube with epithelial cells. Non-adherent cells were washed off with culture medium and excess medium was added to the inlet/outlet ports. After completion of tube formation (~24-48h) the epithelial tubes were cultured in supplemented EMEM medium with reduced FBS to 10% for 5 - 7 days prior to co-culture with endothelial vessels.

4.4.5 Primary Intestinal Epithelial Tube Formation

Jejunal organoids were collected at day 7 to 9 after passaging and dissociated into small organoid fragments as described above. Pellets of organoid fragments were resuspended in expansion medium at a density of 5 million cells per mL. As previously described 3 μ L of organoid cell suspension was introduced into the hollow tubes through the inlet ports. Cells were allowed to settle on the bottom-half of the tubular structure for 24h at 37 °C in 5% CO₂ after expansion medium was added to the gel ports and the inlet/outlet ports during culture. After 24h non-adherent cells were gently washed with expansion medium. Fresh organoids fragments were prepared and seeded again into the tube. Expansion medium was added to the ports and the microdevice cultured for an additional 24h while flipped upside-down to facilitate adhesion of cells to the top-half of the hollow tubular structure. After completion of tube formation (~72h) the primary intestinal epithelium was cultured in differentiation medium (DM) for 5 - 7 days. For

differentiation, the culture medium was replaced with BM (80%v/v), L-WRN CM (10%v/v), supplement mix (without Y-27632 and reduced CHIR 99021 to 500nM), 1x Primocin (InvivoGen) and 10% heat-inactivated fetal bovine serum (FBS; Millipore Sigma). DM was changed twice daily. After 5 - 7 days of differentiation, human umbilical vein endothelial cells (HUVECs) (Lonza) were added to the adjacent hollow tube to generate co-cultures of epithelial and endothelial tubes.

4.4.6 Co-Culture of Epithelial Tubes with Endothelial Tubes

HUVECs were maintained in EGM-2 MV Bulletkit medium (Lonza) and used until passage 8. To generate co-culture of primary intestinal tubes with endothelial vessels, HUVECs were detached using a trypsin/EDTA solution and resuspended at 15 million cells per mL of modified DM. Modified DM was made by replacing BM in the DM formulation with EGM-2 MV Bulletkit medium. 3 μ L of endothelial cell suspension was introduced into the cell-free hollow tube next to the epithelial tube and device was rotated every 15min over a 2-hour period as previously described. Modified DM was added to the gel ports and epithelial inlet/outlet ports during this process to nourish the epithelial cells. After lining the tube with endothelial cells, nonadherent cells were gently washed with modified DM. The epithelial and endothelial tube co-cultures were maintained in modified DM for the remainder of the experiments unless otherwise stated. To support co-culture of HUVEC vessels with Caco-2 epithelial tubes, the supplemented EMEM medium with reduced FBS was mixed with EGM-2 MV at 50:50% v/v dilution and used as culture medium for the remainder of the experiments.

4.4.7 Co-Culture of Epithelial and Endothelial Tubes with NK Cells

NK-92 cell line was acquired from the American Type Culture Collection and maintained in X-VIVO 10 (Lonza) supplemented with 20% FBS and 0.02 mM folic acid (Millipore Sigma) dissolved in 1 N NaOH, 0.2 mM myo-inositol (Millipore Sigma), and IL-2 (100 U/ml; PeproTech). NK cells were collected and after centrifugation at room temperature for 3 min at 300×g, pellets were resuspended in modified DM supplemented with 0.02 mM folic acid, 0.2 mM myo-inositol, and IL-2 (100 U/ml). Resuspended cells were introduced into the endothelial vessel and co-culture for 24h in excess medium.

4.4.8 Neutrophil Isolation

All blood samples were drawn according to institutional review board-approved protocols per the Declaration of Helsinki at the University of Wisconsin–Madison. Neutrophils were purified from whole blood using the MACSxpress Neutrophil Isolation Kit per the manufacturer's instructions (Miltenyi Biotec) and residual red blood cells were lysed using MACSxpress Erythrocyte Depletion Kit (Miltenyi Biotec). Blood was drawn from a total of three nondiseased donors with informed consent obtained at the time of the blood draw according to requirements of the IRB. Prior to loading, the purified neutrophils were stained with calcein AM at 10 nM (Thermo Fisher) according to the manufacturer's instructions. Neutrophils were resuspended in 50:50% v/v EMEM and EGM-2MV culture medium for co-culture with Caco-2 epithelium or resuspended in modified DM for co-culture with primary intestinal epithelium.

4.4.9 Parasite Cell Culture and Infection

T. gondii parasites were harvested and passaged using previously established protocols²²⁷. Briefly, *T. gondii* ME49 tachyzoites were propagated in human foreskin fibroblast (HFF) monolayers grown in Dulbecco's modified Eagle medium (DMEM) containing 10% FBS and 1% Pen/Strep. Tachyzoites were harvested and pelleted by centrifugation at 2,200g for 10 min and resuspended in pre-warmed modified DM or 50:50% v/v EMEM and EGM-2MV culture medium prior to injection into the lumen of the epithelial tubes for infect studies.

4.4.10 Immunofluorescence Staining

For immunostaining, cells were fixed with 4% (v/v) paraformaldehyde (Alfa Aesar) for 20 min and permeabilized with 0.2% (v/v) Triton-X 100 (MP Biomedicals) for 10 min with three 1X PBS wash step between each solution. To reduce nonspecific background fluorescence from collagen, cells were incubated in 0.1 M glycine (Fisher Scientific, Pittsburgh, PA) for 30 min and washed with 1X PBS three times. Subsequently, cells were blocked with buffer solution (3% wt/v BSA and 0.1% v/v Tween 20 (Fisher Scientific)) overnight at 4 °C. Primary antibodies, **Table S2**, diluted in buffer solution were added to the microdevices and incubated at 4 °C for 2 days and washed with 1X PBS three times. Secondary antibodies, **Table S2**, were added to the buffer solution and incubated for 1 day at 4 °C. For cytoskeletal actin and nuclear staining, Alexa conjugated phalloidin (Thermo Fisher) and Hoechst 33342 (Thermo Fisher) at 1:100 were also added to the secondary antibody buffer solution. Lumens were then rinsed with 1X PBS three times over a two-day period.

4.4.11 Image Acquisition

Bright-field and fluorescent images were captured in a Nikon Ti Eclipse with a top stage incubator equipped with temperature and CO₂ control (set at 37°C and 5%, respectively). Neutrophil kinetic parameters including end-to-end displacement and migration speed were analyzed with Fiji (<https://imagej.net/Fiji>) using the track-mate module. Confocal images were acquired at University of Wisconsin-Madison Optical Imaging Core using a Leica SP8 microscope.

4.4.12 Optical Metabolic Imaging

A custom built inverted multiphoton microscope (Bruker Fluorescence Microscopy, Middleton, WI), was used to acquire fluorescence intensity and lifetime images. The equipment consists of Coherent laser. (Coherent, Chameleon Ultra II), an inverted microscope (Nikon, Eclipse Ti), GaAsP PMT (Hamamatsu, H7422PA-40) and a 40x water immersion (1.15NA, Nikon) objective. FAD fluorescence was isolated using an emission bandpass filter of 550/100 nm and excitation wavelength of 890 nm. NAD(P)H fluorescence was isolated using an emission bandpass filter of 440/80 nm and an excitation wavelength of 750 nm. The optical redox ratio was determined from the NAD(P)H and FAD lifetime data by integrating the photons detected at each pixel in the image to calculate the total intensity. For each pixel, the intensity of NAD(P)H was then divided by the intensity of FAD. Using Cell Profiler, an automated cell segmentation pipeline was created. This system identified pixels belonging to nuclear regions by using a customized threshold code. Cells were recognized by propagating out from the nuclei within the image. To refine the propagation and to prevent it from continuing into

background pixels, an Otsu Global threshold was used. The cell cytoplasm was defined as the cell borders minus the nucleus. Values for NAD(P)H intensity, FAD intensity, and the optical redox ratio (NAD(P)H/FAD intensity) were averaged for all pixels within each cell cytoplasm. At least 100 cells per sample were analyzed, and every experiment was repeated at least three times.

4.4.13 Cell Retrieval from Microdevice

To quantify gene expression related to proliferation, differentiation and a function of the intestinal epithelium primary intestinal epithelial cells were selectively retrieved from the intestinal tissue MPS consisting of epithelial and endothelial tubes. The upper half of the microdevice was removed to expose the collagen hydrogel. The hydrogel was then transferred to an Eppendorf tube containing 300 μ l of type I collagenase (6 mg/ml). The sample was incubated on ice for 2 min to degrade the hydrogel and release the cells. Two microliters of biotinylated anti-EpCAM (Thermo Fisher Scientific) was added, and the sample was incubated at 4°C for 15 min. Ten microliters of SeraMAGS beads coupled to streptavidin was added, and the sample was incubated for another 10 min at 4°C. The SeraMAGS beads, with the epithelial cells (EpCAM-positive), were isolated using a magnet and lysed for PCR analysis. To quantify gene expression related to protective immunity, neutrophils were selectively retrieved from the intestinal tissue MPS 6h after introduction into the endothelial vessel. Non-adherent neutrophils were first collected from the endothelial vessels through the pipette-accessible ports. To isolate neutrophils that have migrated into the ECM gel, a 2-mm-diameter biopsy punch (Fisher Scientific) was used to cut out the hydrogel next to the endothelial vessel. The hydrogel

punches were transferred to an Eppendorf tube and processed to separate EpCAM-positive epithelial cells, following the same protocol described above, leaving behind neutrophils in suspension. These neutrophils were mixed with neutrophils collected from the endothelial vessel and lysed for PCR analysis.

4.4.14 Reverse Transcription Quantitative Polymerase Chain Reaction

To study how primary intestinal epithelial cells and neutrophils adapted to the microenvironment within the intestinal tissue MPS, the expression of multiple genes related to different pathways was analyzed by RT-qPCR. Briefly, mRNA was isolated from cells using the Dynabeads mRNA DIRECT Purification Kit (Invitrogen). Isolated mRNA was quantified using a Qubit fluorometer (Thermo Fisher Scientific) and the Qubit RNA BR Assay Kit (Thermo Fisher Scientific). cDNA was produced using the High Capacity RNA-to-cDNA Kit (Applied Biosystem) and the cDNA was pre-amplified with SsoAdvanced PreAmp Supermix (Bio-Rad) using primers from Integrated DNA Technologies or Thermo Fisher Scientific, **Table S3-4**. cDNA was analyzed by RT-qPCR using iTaq Universal SYBR Green Supermix (Bio-Rad) or Roche Lightcycler master mix according to manufacturer's protocols in Roche's Lightcycler 480 II. Gene expression was normalized using the delta-delta Ct method. To quantify genomic DNA of *T.gondii*, infected epithelial tubes were digested as described above, and genomic DNA was extracted using TRIzol according to manufactures instructions. DNA was purified by phenol/chloroform extraction followed by ethanol precipitation. Genomic DNA was used as the template for preamplification and RT-PCR, as described above, using *T. gondii* primers (Table S2).

4.4.15 Multiplex Cytokine/Chemokine Assays and Analysis

To measure NK cell-mediated cytokines secretion, media were collected from intestinal tissue MPS with *T. gondii* infected epithelium in the presence and absence of NK cells. Media were collected after 24h in culture and cytokine/chemokine concentrations analyzed using the Inflammation 20-Plex Human ProcartaPlex™ panel (EPX200-12185-901, Thermo Fisher) following the manufacturer's guidelines. Data were collected on MAGPIX Luminex Xmap system (Luminex Corporation) using Luminex xPonent software. Concentration of each analyte was determined from a standard curve, generated by fitting a five-parameter logistic regression of median fluorescence on known concentrations of each analyte.

4.4.16 Statistical Analysis

Data were analyzed (Prism 9.0; GraphPad Software). The normal distribution assumption for statistical tests was confirmed by the Shapiro Wilk test. Statistical significance was assessed using Student's t tests when comparing two conditions/groups and when comparing more than two groups, significance was assessed using one-way analysis of variance (ANOVA) corrected using the Tukey's test. For nonparametric comparisons, a Mann-Whitney U test or a Kruskal-Wallis test was performed.

4.5 Acknowledgments

We thank Dr. Evie Carchman from the Department of Surgery and UWCCC Biobank at the UW-Madison for the supply of small intestinal tissue, Huttenlocher Lab from the

Department of Medical Microbiology and Immunology at the University of Wisconsin-Madison for facilitating blood draws from healthy donors. We also thank the UW Optical Imaging Core for the support on the 3D confocal imaging. National Institutes of Health grant F31CA247248 (MH) National Institutes of Health grant R01CA186134; National Institutes of Health grant R01AI144016; University of Wisconsin Carbone Cancer Center Support Grant NIH P30CA014520)

Chapter 5

Concluding Remarks and Future Directions

The work presented in this dissertation describes three microfluidic-based platforms that address gaps in our ability to discover and understand key new features of diseases associated with tubular organs. In Chapter 2 we described a simple method to generate arrays of tubular structures within a 3D ECM gel in a single process. By using liquid bridges and liquid barriers, we demonstrated our ability to create diffusion-based gradients and perform parallel, on-demand, and reconfigurable co-culture experimentation in the same device. This platform offers benefits including increased throughput of more complex culture systems without compromising time or task complexity and provides robust spatial and temporal control over multi-tissue interactions. The study presented in Chapter 3 used an organotypic vascular model or MPS to examine juxtacrine and paracrine signaling between breast cancer cells and the vasculature that alter the microenvironment to promote metastatic spread to distant organs. The platform used in this study enabled us to examine the relationship between molecular and functional responses of tumor cells and the vasculature during tumor cell extravasation in a more relevant culture microenvironment (i.e., tissue architecture and cell-ECM interactions). Specifically, this chapter highlighted cancer-vascular molecular signaling that can lead to changes in cellular function including vascular permeability, matrix remodeling and event of tumor cell extravasation during cancer breast cancer metastasis. Most important, this study used clinically active therapeutics to test effects

of these molecular signaling and explored the effects of targeting multiple pathways at once, demonstrating the potential for these models to be integrated into preclinical studies for drug development. Finally, in Chapter 4 a platform was described that models the infection environment of the human intestinal tissue during parasitic infection. Key attributes of the platform include integration of relevant tissue architecture (tubular intestinal epithelium and endothelium), microenvironmental components (differentiated intestinal epithelium, endothelial vasculature, innate immune cells, and ECM) and human primary cell sources (intestinal epithelial, endothelial, and immune cells) for more physiologically relevant modeling of the infection microenvironment. Using the platform, innate immune cell responses occurring at the gut-epithelium and vasculature during acute parasitic infection were examined. The platform enabled us to explore the role of human innate immune cells in parasite clearance and tissue dissemination in a robust manner. More importantly, this work demonstrated the potential of this platform in discovering immune-mediated targets to enhance parasite clearance and to be used for patient-specific modeling.

In the future, these platforms could be extended in the following ways for application in a diverse set of research areas.

5.1 Multi-Organ Interactions and Dynamic Reconditioning Experiments Using Microfluidic Array Platform

In Chapter 2, we demonstrated the ability to conduct parallel micro tissue culture then co-culture using a reconfigurable liquid barrier on the same chip. This concept can be

extended to perform more complex multi-tissue culture using cells from different organs, towards multi-organ interactions for drug and therapeutic studies. *In vivo*, tissues and organs in the human body are highly interconnected and often rely on biochemical signals and support from other organs to function normally. In the context of drug development, multi-organ interaction studies can help illuminate toxic effects of drugs on secondary tissue which contribute to unnecessary drug failure or withdrawal due to negative side effects at the clinical stage. As cancer metastasis involves multi-tissue and multi-organ interactions, future experiments using our microfluidic array platform could include the study of tumor cell reconditioning by stromal components from pre-metastatic niches (secondary sites), especially after extravasation. By leveraging our reconfigurable liquid barrier approach, it may be possible to decouple tumor intrinsic factors from stromal derived factors that influence modulation of microenvironment and tumor cell behavior at secondary metastatic sites and identify new therapeutic targets. Moreover, this platform could accelerate screening of potential therapeutic drugs targeting tumor-stroma interactions to limit metastatic progression.

5.2 Examine and Target Tumor-Stromal Signaling at Secondary Metastatic Sites

In Chapter 3, cancer-vascular interactions involved in breast cancer cell extravasation as well as its influence on functional responses of tumor cells and the vasculature was studied. A frequent site of metastasis for patients diagnosed with triple negative breast cancer, one of the most aggressive subtypes with poor prognosis, is the lung. Several stromal components at the metastatic site including resident-macrophages ²²⁸, fibroblasts, lung epithelium and stromal secreted ECM ²²⁹ have been implicated in

promoting extravasation and activating pro-survival signaling pathways. To increase the relevance of the model, incorporation of these stromal components could give more insight into other molecular targets that weren't found in the model with only vascular and tumor cell components. Future work can also include targeting these signaling events with drugs/antibodies. Since cellular metabolism is particularly sensitive to upstream molecular interventions, optical metabolic imaging (OMI) can be used for rapid cellular-level assessment of metabolic response to drug action. OMI is a non-invasive, high-resolution imaging approach that exploits the intrinsic fluorescence of the metabolic co-enzymes NADH and FAD for dynamic monitoring of cellular metabolism²³⁰. This imaging approach is label-free and can enable drug response to be dynamically quantified over a treatment time-course across cell types on a single-cell level²³¹. Because it is non-destructive and if coupled with other bioassays, it can better-inform downstream assessment of biological responses, saving time and cost, and enabling faster discovery of effective treatment options.

The following design is proposed for studying breast cancer cell extravasation into the lung microenvironment, **Figure 5.1**. Preliminary work using cell lines showed that lung stromal cells including fibroblasts (CCD-19Lu) and macrophages (RAW 264.7) can seamlessly be incorporated into the model to mimic breast cancer cell extravasation into the lung microenvironment. Interpretation of OMI of the various cell types showed differential metabolic response to co-culture based on redox ratios and fluorescent intensity lifetimes of metabolic cofactors within each cell type **Figure 5.1C**. This demonstrates the sensitivity of the OMI approach in detecting a range of metabolic

profiles and the compatibility of the organotypic model with OMI for monitoring metabolic changes (i.e., drug response) within the model.

The end goal would be to build a more relevant model that closely mimics the *in vivo* microenvironment and characterize and target key signaling events that may be contributing to increased extravasation and growth rates at the lung microenvironment. By using tools like OMI to measure the temporal dynamics of the overall changes in metabolic response across multiple cell types (e.g., cancer cells, macrophages, fibroblasts, endothelial and epithelial cells) in response to therapeutics over treatment course can be monitored. The combination of OMI with organotypic modeling will allow for accelerated discovery of novel drug combinations through improved modelling of the metastatic microenvironment and increase in the number of testable drug targets.

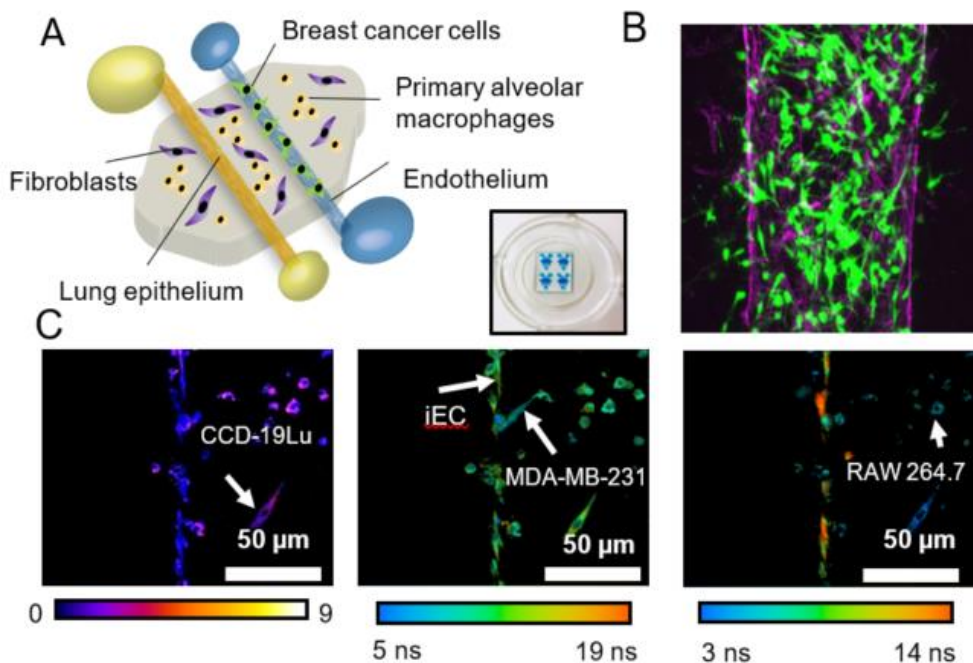


Figure 5.1 Breast Cancer Metastasis into the Lung Microenvironment. (A) Model scheme of breast cancer lung metastasis model: one endothelial vessel(left) with breast cancer cells within the lumen of the vessel and one epithelial tube (right), surrounded by fibroblasts and

macrophages embedded in ECM. (B) Confocal image of iPSC-EC endothelium with GFP-tagged breast cancer cells. (C) Representative redox ratio (left), NAD(P)D(middle) and FAD (right) mean lifetime images of RAW 264.7 macrophages, CCD-19Lu lung fibroblasts, iPSC-EC endothelium and MDA-MB-231 cells in co-culture.

5.3 Integrating Relevant Oxygen Levels for Improved Modeling of Intestinal

Tissue Microenvironment

In Chapter 4, a human intestinal tissue model was described and used to study how parasites interact with human innate immune cells in the intestinal tract and the role of immune cells in promoting tissue dissemination or eliciting protective immune response. Key microenvironmental components such as tissue architecture, cellular components and human cell sources were incorporated in the model to improve relevance. Another key factor of the infection microenvironment is the increase in cellular oxygen demands leading to hypoxic stress, which affect immune cell function, host-pathogen interaction, and pathogenesis. Future work could integrate the control of oxygen levels in our platform. We have previously developed a method to establish autonomously regulated oxygen microenvironments (AROMs) that facilitate growth of enteric anaerobes and mimic the oxygen supply-demand balance seen *in vivo*²³². The method uses a silicone oil overlay, which behaves as an adjustable gas diffusion barrier allowing the oxygen microenvironment to be set via the supply-demand balance of oxygen²³². This method can be integrated into the intestinal tissue model by adding an oil overlay to separate the model containing the cells from the ambient oxygen environment (i.e. ~21% oxygen). Compared to the existing externally defined oxygen control methods (which disrupt the natural supply-demand regulation), AROM will allow the cells in the model to self-regulate the oxygen microenvironment in response to the infection more naturally and dynamically. Incorporating

AROMs that mimic the oxygen supply-demand balance seen *in vivo* can help better recapitulate cellular stress response of immune cells during parasitic infection and can also enable the culture of anaerobic bacteria while providing adequate oxygen supply to the host cells to mimic the gastrointestinal infection microenvironment more closely.

The following experimental setup is proposed for controlling oxygen levels in the intestinal tissue modeling platform, **Figure 5.3**. Preliminary experimentation using Caco-2 epithelial tubes in our model revealed that with silicone oil overlay, reduced intracellular oxygen levels can be achieved compared to control systems.

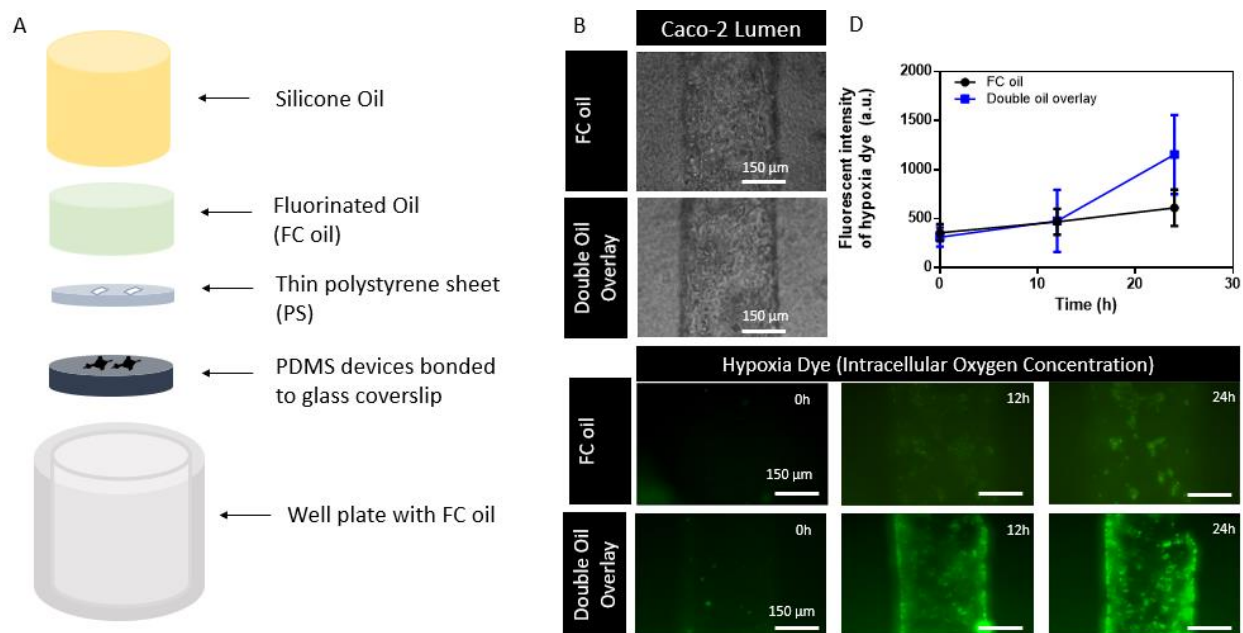


Figure 5.2 Controlling Oxygen Microenvironment of The Intestinal Tissue Model. (A) Model scheme showing the integration of AROM with the intestinal tissue model. The silicone oil overlay provides a diffusion barrier which allows the cells to regulate the oxygen environment via a supply-demand balance. Gas permeability through the oil overlay can be adjusted by selecting different oil properties (e.g., oil type, depth, viscosity). A thin polystyrene sheet, with small openings that align with areas covered by cells, is placed on top of the device to further limit oxygen diffusion through the PDMS layer to the cell-free areas of the device. Fluorinated oil

surrounds the device and is overlaid on top of the PS sheet to act as an inert immiscible barrier preventing swelling of PDMS by the silicone oil overlay. (B) Brightfield image showing Caco-2 cell-derived tubular epithelium overlaid with FC oil only (control) or double oil overlay (FC oil and silicone oil). (C) Immunofluorescence images showing intracellular oxygen concentrations probed by an intracellular hypoxia dye taken up cells in the tubular epithelium at 0h, 12h and 24h for FC oil or double oil overlay. Higher intensity indicates reduced oxygen. (D) Quantified fluorescence intensity shows reduced oxygen levels in epithelial cells with double oil overlay at 24h compared to control systems without silicone oil overlay.

The goal would be to develop a human intestinal tissue model that can predict clinical outcomes when human tissue is exposed to parasites. Such models will allow the screening of therapeutics and samples from vaccinated patients, as well as potential diagnostic tests for unexplained or poorly understood responses to therapeutics.

Overall, the microfluidic-based platforms presented in this dissertation facilitate robust and improved modeling of multi-tissue interactions involving tubular structures and help to provide mechanistic insight into the role of microenvironmental components that promote disease progression in cancer metastasis and parasitic infection. Although the platforms presented in this dissertation are designed to target different biological questions, the primary goal is to enable more relevant studies and facilitate exploration of the complex parameter space in human diseases.

Appendix

Appendix A: Additional Tables and Graphs from Chapter 3

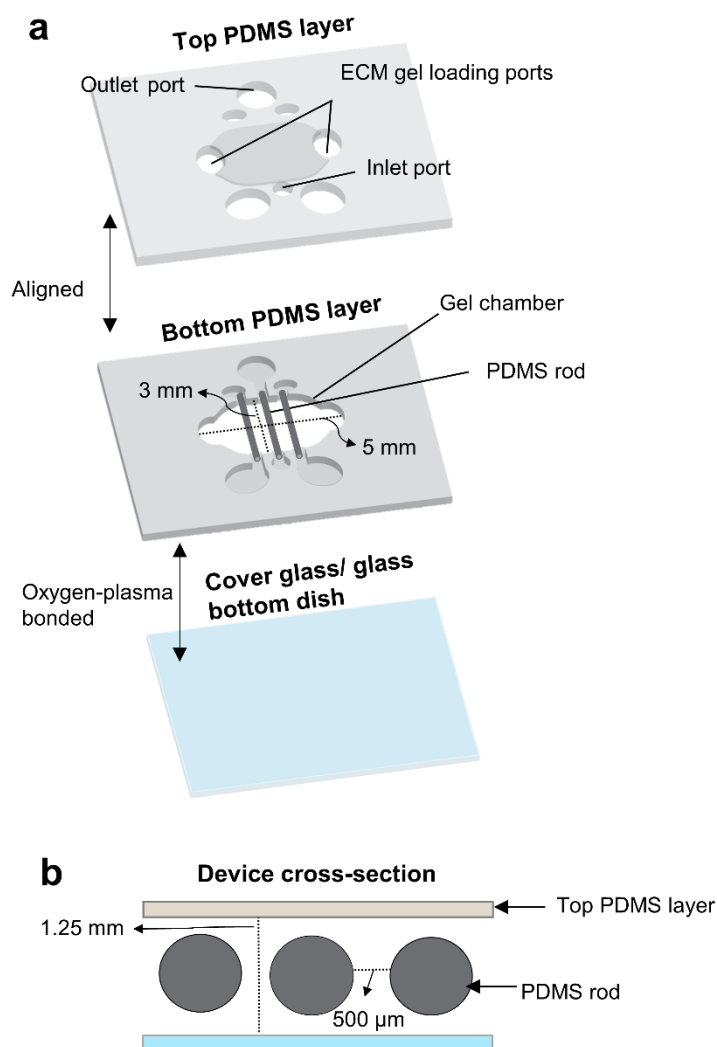


Figure A.1 3D organotypic breast cancer extravasation model design and dimensions. (A) Schematic isometric slice-view of the BCC extravasation model. Two PDMS layers with patterned features are aligned and bonded to a microscope cover glass / glass bottom dish. Gel chamber dimensions are 3 mm (length) and 5 mm (width) (B) Device cross-section along ECM gel loading ports. The gel chamber height is 1.25 mm from the top PDMS layer to the glass-bottom dish. PDMS rods are 500 μ m apart.

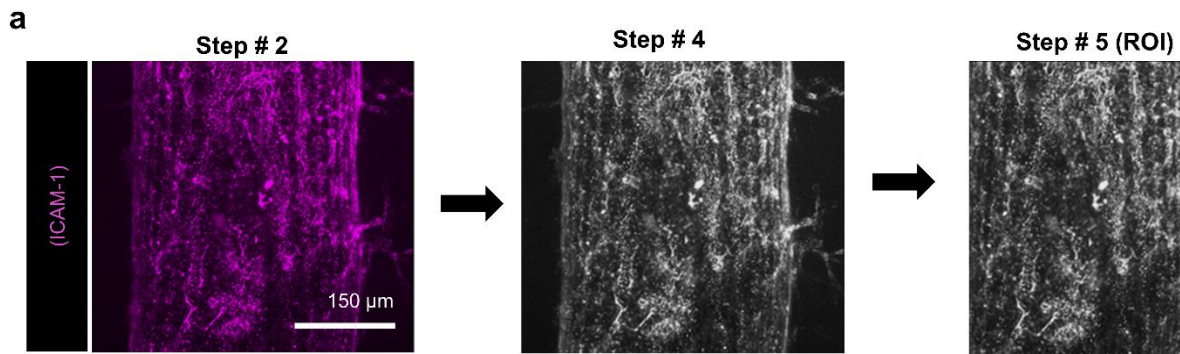


Figure A.2 ICAM-1 expression analysis of iPSC-EC vessels in monoculture and in co-culture with MDA-MB-231 cells. (A) Confocal projection of iPSC-EC vessels stained for ICAM-1 expression and image processing sequence.

Quantification of ICAM-1 and COL IV expression

Acquire confocal image as a 3D stack

1. Import 3D stack image on ImageJ
2. Image → Stack → Z-project (image 2D projection)
3. Analyze → Set measurements → Select measurement parameters and include Area and Mean Intensity.
4. Image → Type → 16-bit
5. Select rectangular ROI within the vasculature → Analyze → Tools → ROI Manager → Add to manager (this saves the ROI dimensions to be in analysis of subsequent images).
6. Image → Duplicate (this separates the ROI from image)
7. Analyze → Measure (this displays parameters selected in step 3, record mean intensities)
8. Repeat steps #1 through #7 to quantify mean intensities of ICAM-1 and COL IV expression in vessels of monoculture and co-culture conditions.

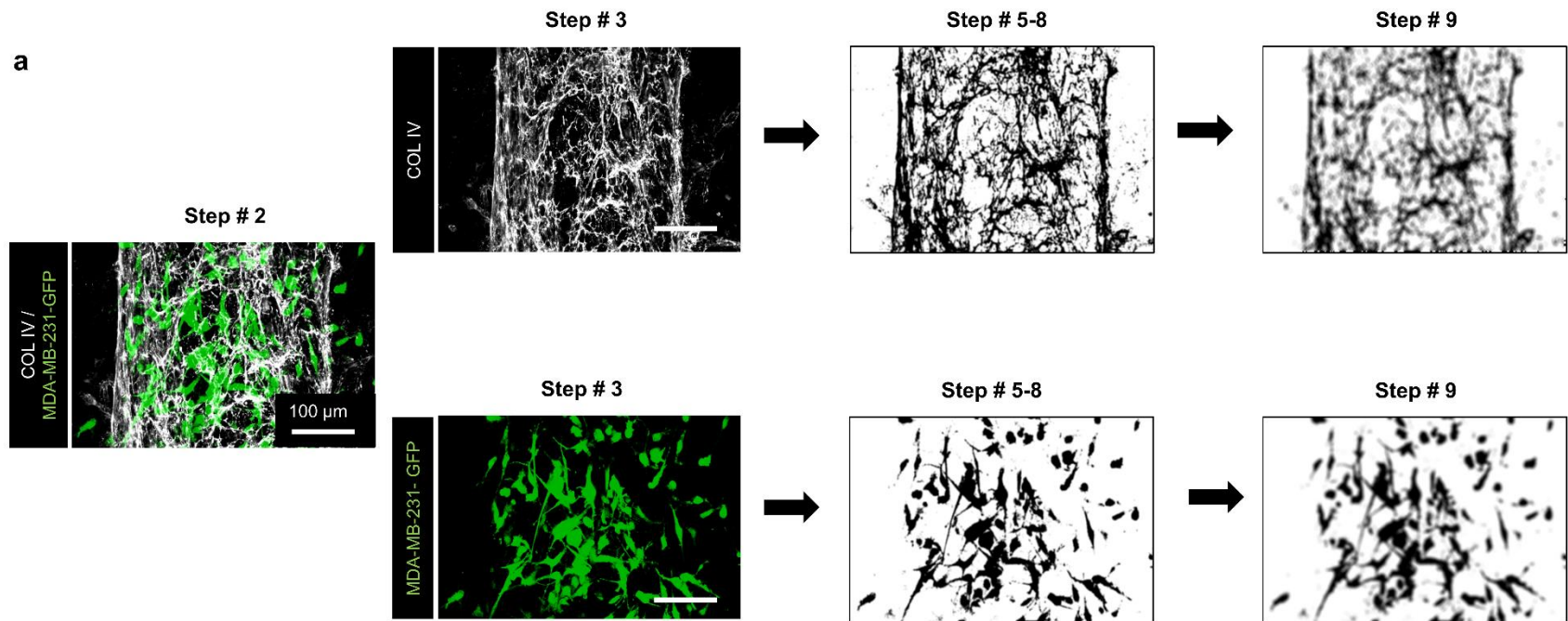


Figure A.3 Intensity profile analysis of COL IV distribution across iPSC-EC lumens under monoculture and direct-contact co-culture with MDA-MB-231 cells. (A) Image processing sequence of iPSC-EC vessels stained for COL IV and MDA-MB-231 cells.

Quantification of COL IV expression profile across iPSC-EC vessels

Acquire confocal image as a 3D stack

1. Import 3D stack image on ImageJ
2. Image → Stack → Z-project (image 2D projection)
3. Image → Color → Split Channels (separate Col IV channel from GFP-labelled MDA-MB-231 cells)
4. Analyze → Set measurements → Select measurement parameters and include Area and Mean Intensity.
5. Process → Binary → Make binary (Binarize your 2D projection)
6. Image → Type → 16-bit
7. Select rectangular ROI that captures the vasculature and surrounding matrix → Analyze → Tools → ROI Manager → Add to manager (this saves the ROI dimensions to be in analysis of subsequent images).
8. Image → Duplicate (this separates the ROI from image)
9. Process → Filters → Mean
10. Analyze → Plot profile (this displays intensity across the ROI selected)
11. Repeat steps #1 through #9 to quantify mean intensities of Col IV deposition in monoculture and co-culture conditions.
12. Repeat steps #1 through #9 to quantify mean intensities of GFP-labelled MDA-MB-231 cells in co-culture condition.

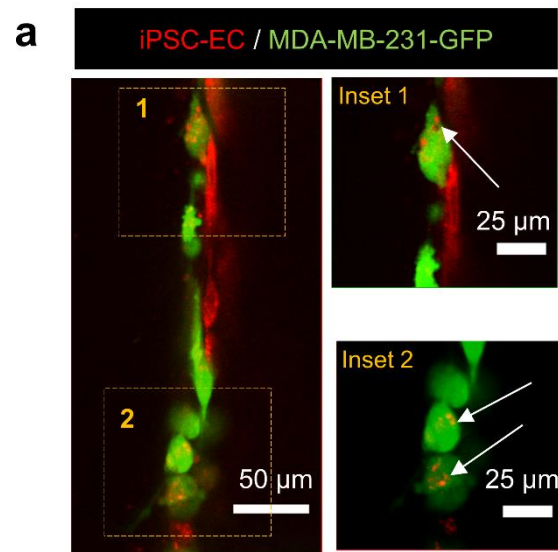


Figure A.4 Membrane transference between iPSC-EC vessel and MDA-MB-231 cells. (A) iPSC-EC membrane components stained in red within GFP-tagged MDA-MB-231 cells, indicated by white arrows.

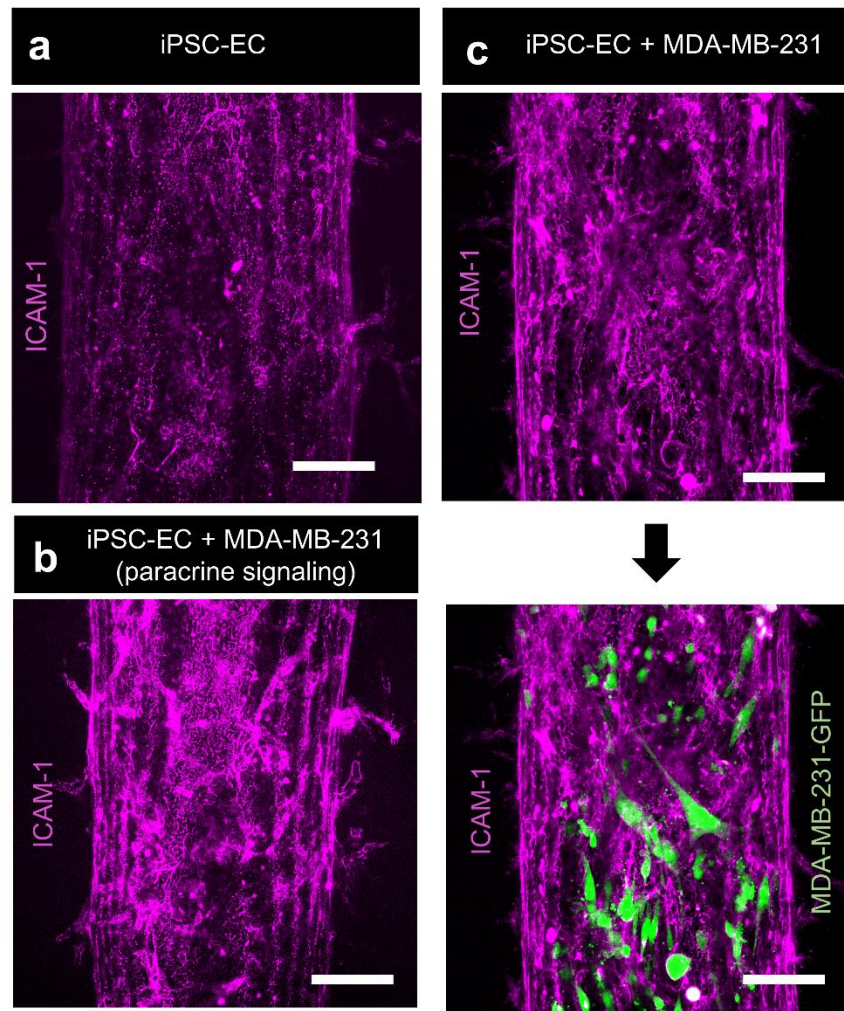


Figure A. 5 Differential ICAM-1 expression on iPSC-EC vessels in monoculture and in co-culture with MDA-MB-231 cells. Confocal projections of ICAM-1 expression on iPSC-EC vessel in monoculture (A), in co-culture with MDA-MB-231 cells via paracrine signaling mode (B), and in direct-contact interaction mode (C), scale bars indicate 100 μm.

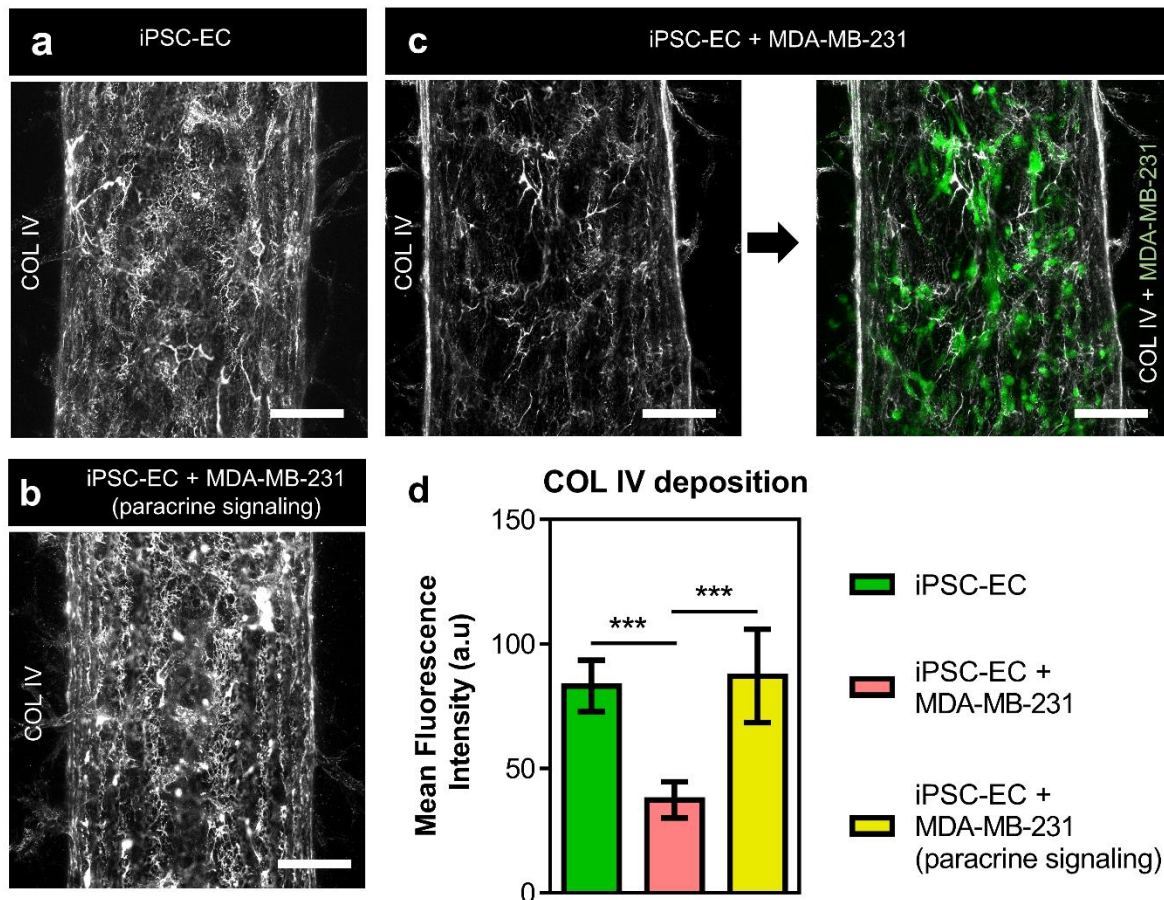


Figure A.6 Differential COL IV deposition by iPSC-EC vessels in monoculture and in co-culture with MDA-MB-231 cells. Confocal projections of COL IV expression on iPSC-EC vessel in monoculture (A), in co-culture with MDA-MB-231 via paracrine signaling mode (B), and following extravasation (C), scale bars indicate 100 μ m. (D) Mean fluorescence intensity analysis comparing COL IV deposition by iPSC-EC vessels in monoculture and in co-culture with MDA-MB-231 cells. Plot: mean fluorescence intensity + SD, statistical analysis: ordinary one-way ANOVA with Tukey's multiple comparisons test, *** $p \leq 0.001$. Data represents average of at least 6 different regions of interests (ROIs) across 4 different systems.

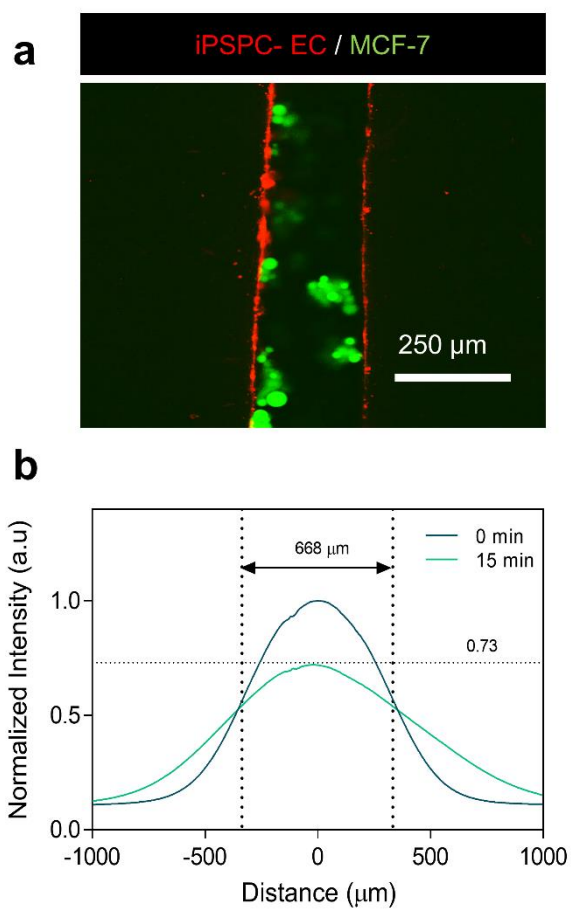


Figure A.7 Impact of MCF-7 culture on iPSC-EC vascular permeability. (A) Fluorescent images of MCF-7 cells cultured within an iPSC-EC vessel. (B) Normalized intensity profiles of 70 kDa dextran diffusion across iPSC-EC vessels, with a peak intensity drop to 73% and a profile width of 668 μm .

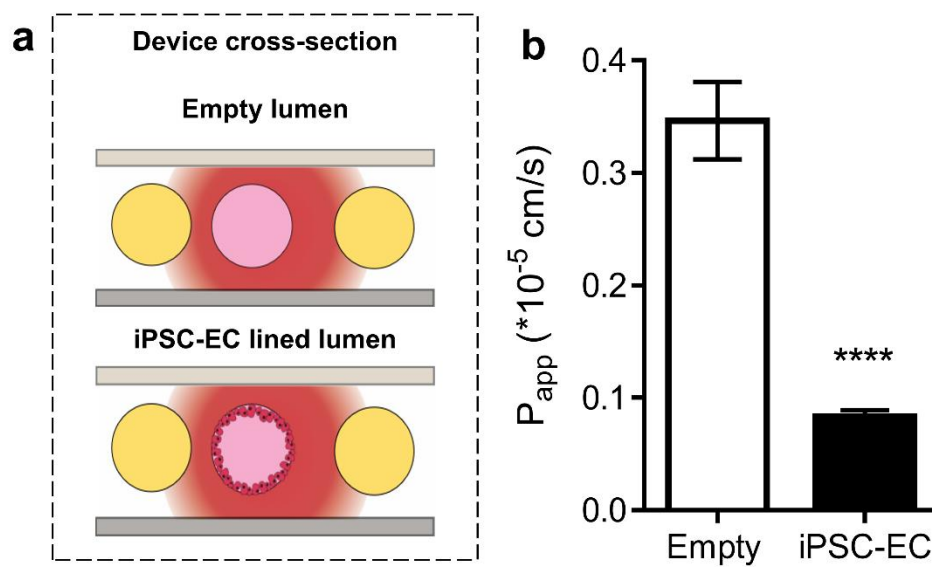


Figure A.8 Permeability of iPSC-EC vessel compared to a control lumen with no endothelial cells. (A) Schematic representation of device cross-section during permeability assessment. (B) Permeability analysis of iPSC-EC lined lumen compared to a lumen without endothelial cells. Plot: mean permeability + SD, statistical analysis: Student-test, **** $p \leq 0.0001$ (n=4).

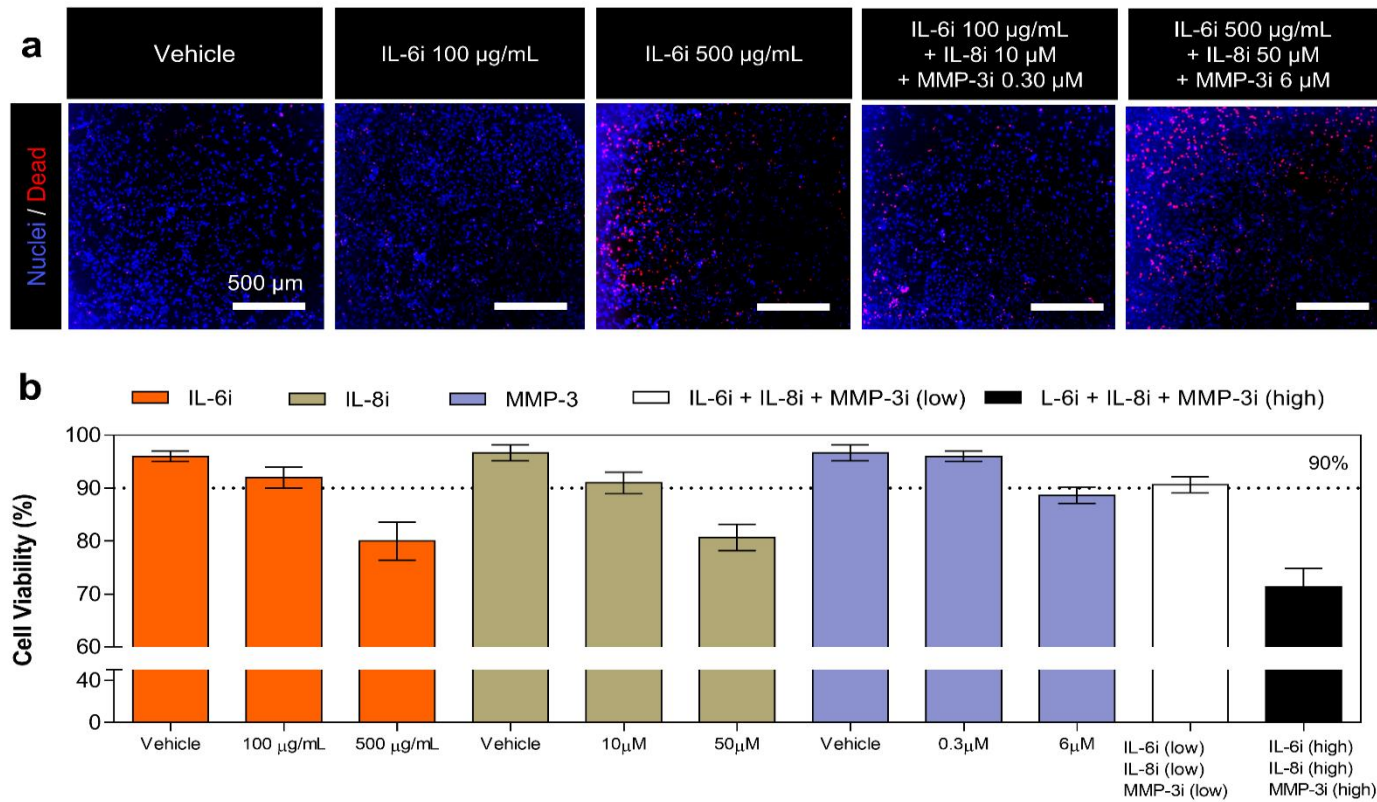


Figure A.9 Viability assessment of iPSC-ECs incubated with different concentrations of inhibitors in a well plate for 48 h. (A) Nuclei and dead cell staining of iPSC-ECs treated with vehicle, tocilizumab (anti-IL-6R mAb) and combined treatment with reparixin (IL8R1/CXCR1 or IL8R2/CXCR2 inhibitor), and MMP-3 inhibitor at low and high dose. **(B)** Quantified cell viability of iPSC-ECs treated with tocilizumab, reparixin and UK-356618 independently and in combination. 90% viability was observed at low dosage for independent and combined treatment.

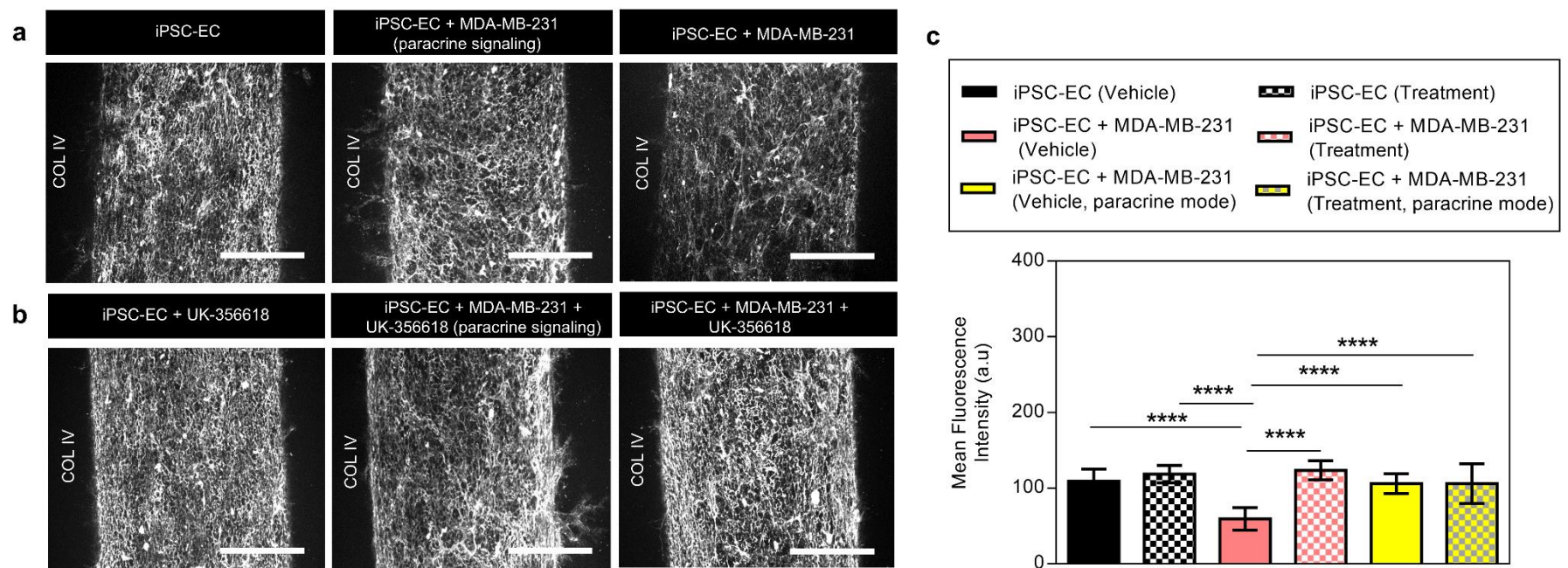


Figure A.10 Effect of MMP inhibition (UK-356618, an MMP-3 inhibitor) on COL IV expression on iPSC-EC vessels within the BCC extravasation model. Confocal projections COL IV deposition by iPSC-EC vessels in vehicle treated (A) and UK-356618 treated (B) monoculture conditions, and co-culture conditions with MDA-MB-231 cells, scale bars indicate 150 μ m. (C) Mean fluorescence intensity analysis comparing COL IV expression on vehicle controls and UK-356618 treated systems. Plot: mean fluorescence intensity + SD, statistical analysis: ordinary one-way ANOVA with Tukey's multiple comparisons test, **** $p \leq 0.0001$. Data represents average of at least 6 different regions of interests (ROIs) across 4 different systems.

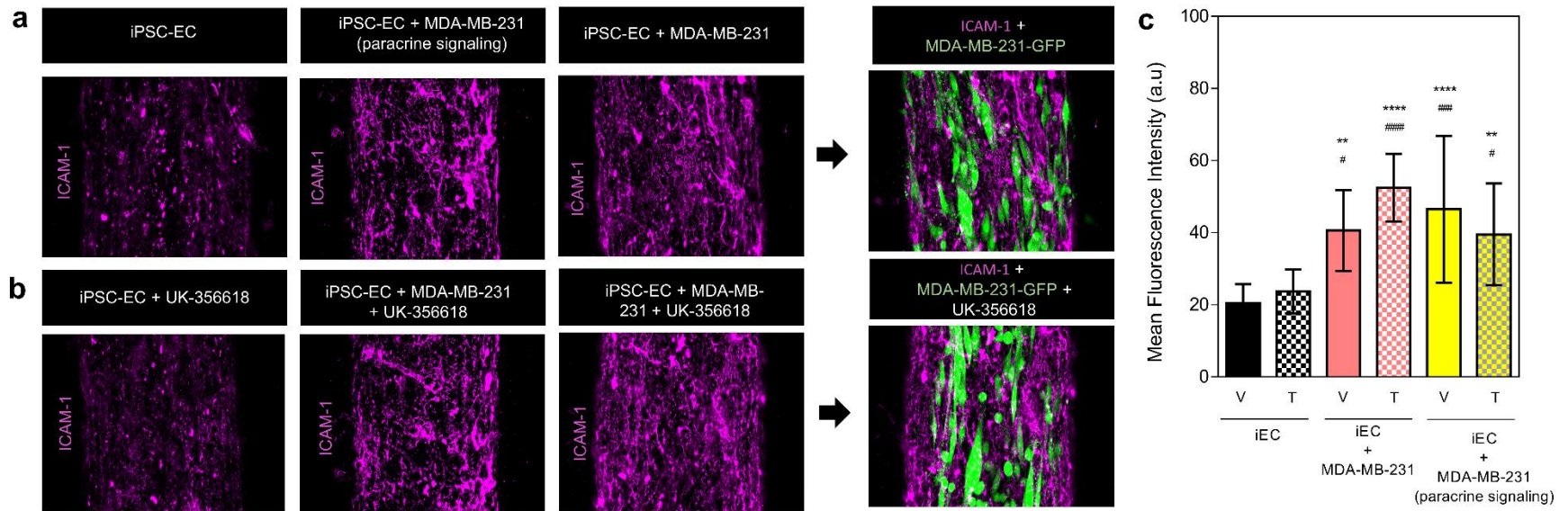


Figure A.11 Effect of MMP inhibition (UK-356618, an MMP-3 inhibitor) on ICAM-1 expression in iPSC-EC vessels within the BCC extravasation model. Confocal projections showing ICAM-1 expression on iPSC-EC vessels in vehicle treated (A) and UK-356618 treated (B) monoculture conditions, and co-culture conditions with MDA-MB-231 cells, scale bars indicate 150 μ m. (C) Mean fluorescence intensity analysis comparing ICAM-1 expression on vehicle treated and UK-356618 treated systems. Plot: mean fluorescence intensity + SD, statistical analysis: ordinary one-way ANOVA with Tukey's multiple comparisons test. ** $p \leq 0.01$ and **** $p \leq 0.0001$ denotes relative to vehicle control of iPSC-EC vessels in monoculture. ### $p \leq 0.01$, #### $p \leq 0.001$ and ##### $p \leq 0.0001$ denotes relative to treated condition of iPSC-EC vasculatures in monoculture. Data represents average of at least 6 different regions of interests (ROIs) across 4 different systems.

Table A.1 Primary and secondary antibodies used for immunofluorescent staining.

Primary antibody	Company code	Dilution	Secondary antibody	Dilution
CD31	Abcam (AB9498)	1:20	^a Alexa Fluor 568 anti-mouse	1:100
VE-cadherin	Abcam (AB33168)	1:50	^b Alexa Fluor 647 anti- rabbit	1:100
Collagen IV	Abcam (AB6586)	1:50	Alexa Fluor 568 anti-rabbit	1:100
ICAM-1	R&D Systems (BBA3)	1:100	Alexa Fluor 647 anti-mouse	1:100

^{a,b} Goat source

CD31 and VE-cadherin were co-stained

Appendix B: Additional Tables and Graphs from Chapter 4

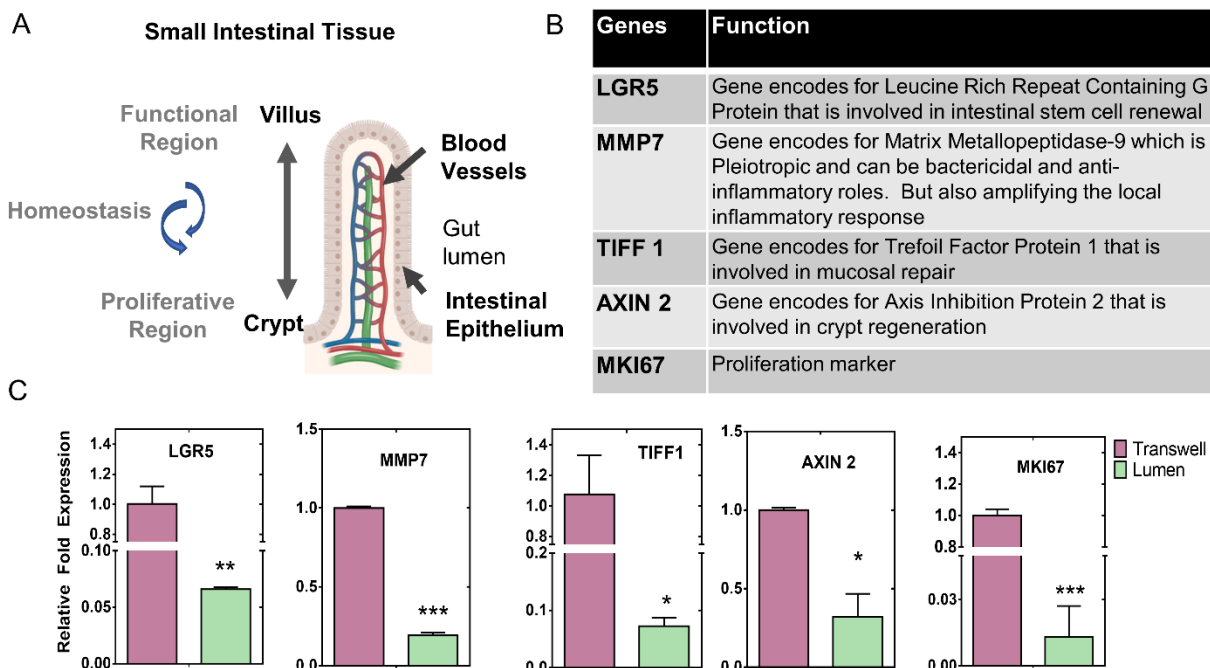


Figure B.1 Upregulated genes in primary intestinal epithelium cultured and differentiated in the human intestinal tissue MPS relative to standard culture methods. (A) Schematic representation showing the crypt-villus axis of the intestinal epithelium and the spatial distribution of proliferative and functional region. (B) Markers associated with proliferation and differentiation, or functional epithelium of the intestinal tissue. (C) Differential gene expression of the intestinal epithelium in the intestinal tissue MPS versus in transwell culture. Bar graph showing gene expression of downregulated genes, which include leucine-rich-repeat-containing G-protein-coupled receptor 5 (LGR5) for intestinal stem cells; Matrix Metalloproteinase-7 (MMP7) bactericidal and anti-inflammatory effects; Trefoil Factor 1 (TIFF1) for mucosal repair; Axis Inhibition Protein 2 (AXIN2) for crypt regeneration and proliferation marker (MKI67) for stem cells. Values are presented as mean \pm SD from 4 independent experiments involving tubular or monolayer epithelium generated from human intestinal organoids where significance is expressed as *** $p \leq 0.001$, ** $p \leq 0.01$ and * $p \leq 0.05$).

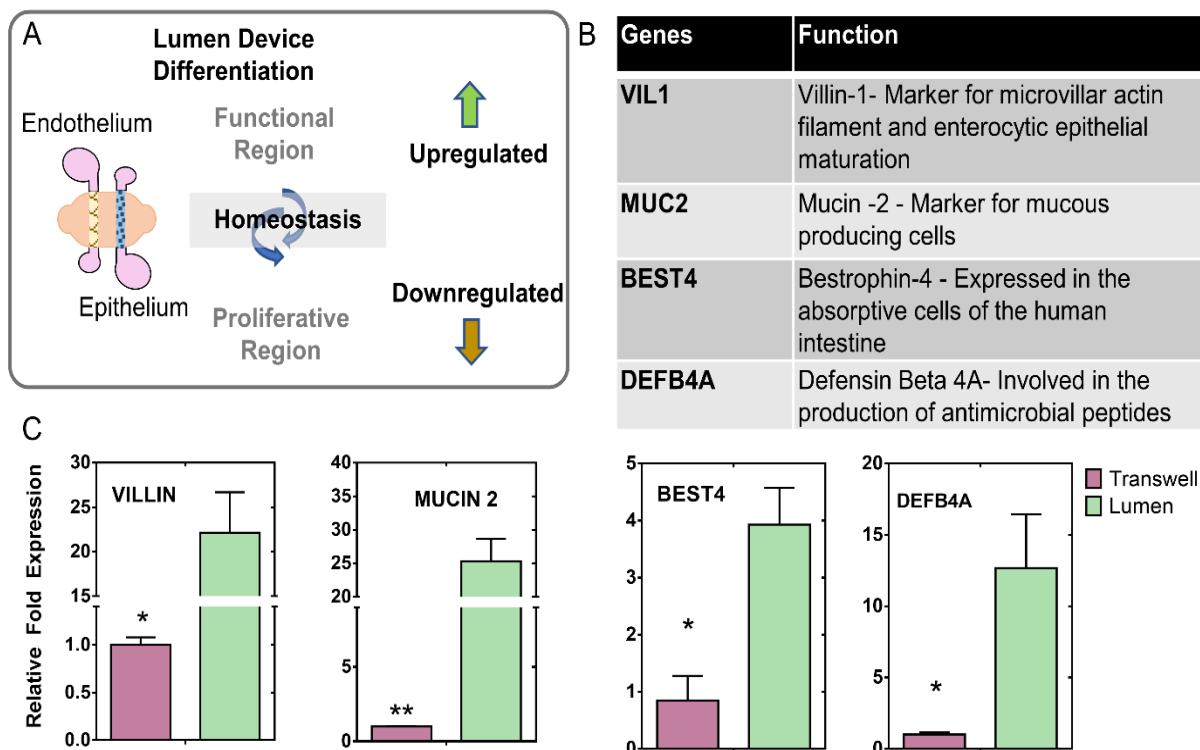


Figure B.2 Downregulated genes in primary intestinal epithelium cultured and differentiated in the human intestinal tissue MPS relative to standard culture methods. (A) Schematic representation showing upregulation and downregulation of genes in the epithelial tubes formed in the intestinal tissue MPS and their association with the proliferative and functional region of the intestinal epithelium. (B) Markers associated with proliferation and differentiation, or functional intestinal epithelium in the intestinal tissue. (C) Differential gene expression of the intestinal epithelium in the intestinal tissue model versus in transwell culture. Bar graph showing gene expression of upregulated genes, which include villin-1 (VIL1) for microvilli formation; mucin 2 (MUC2) for goblet cells; Bestrophin-4 (BEST4) for absorptive cells and β -defensin-4 (DEFB4) for antimicrobial peptides. Values are presented as mean \pm SD from 4 independent experiments involving tubular or monolayer epithelium generated from human intestinal organoids where significance is expressed as $**p \leq 0.01$ and $*p \leq 0.05$).

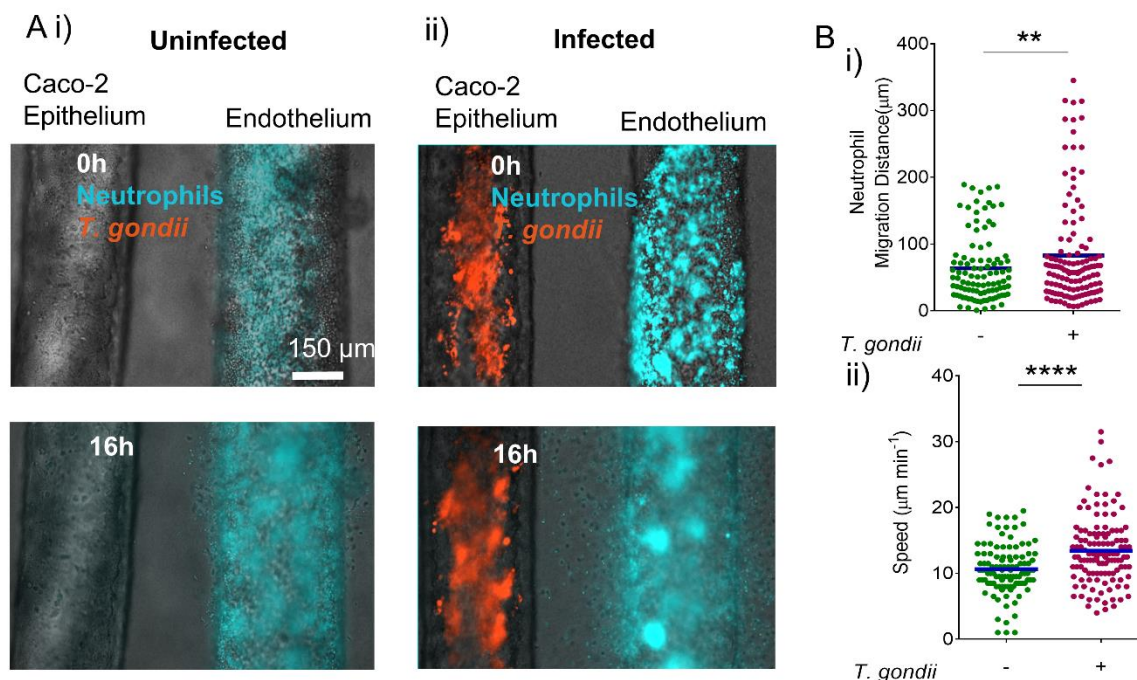


Figure B.3 Dynamic analysis of neutrophils extravasation and trafficking towards *T.gondii* infected epithelium. (A) Combined brightfield and immunofluorescence images showing the interface between the gut epithelium and endothelium in the intestinal tissue MPS. Neutrophils were introduced into the endothelial vessel and monitored for their extravasation and migration behavior over a 16-h period (i). Caco-2 epithelial tubes were infected with m-cherry tagged ME49 *T. gondii* for 48h before introducing neutrophils into the endothelial vessel (ii). Neutrophils were seen to extravasate and migrate towards the infected epithelium. (B) Grouped scatter plot showing migration distance (i), as measured by end-to-end displacement following extravasation of neutrophils, and the average speed towards a *T.gondii*-infected epithelium. Each dot represents the migration distance and speed of a single neutrophil from the endothelial vessel boundary, significance is expressed as **** $p \leq 0.0001$ and ** $p \leq 0.01$.

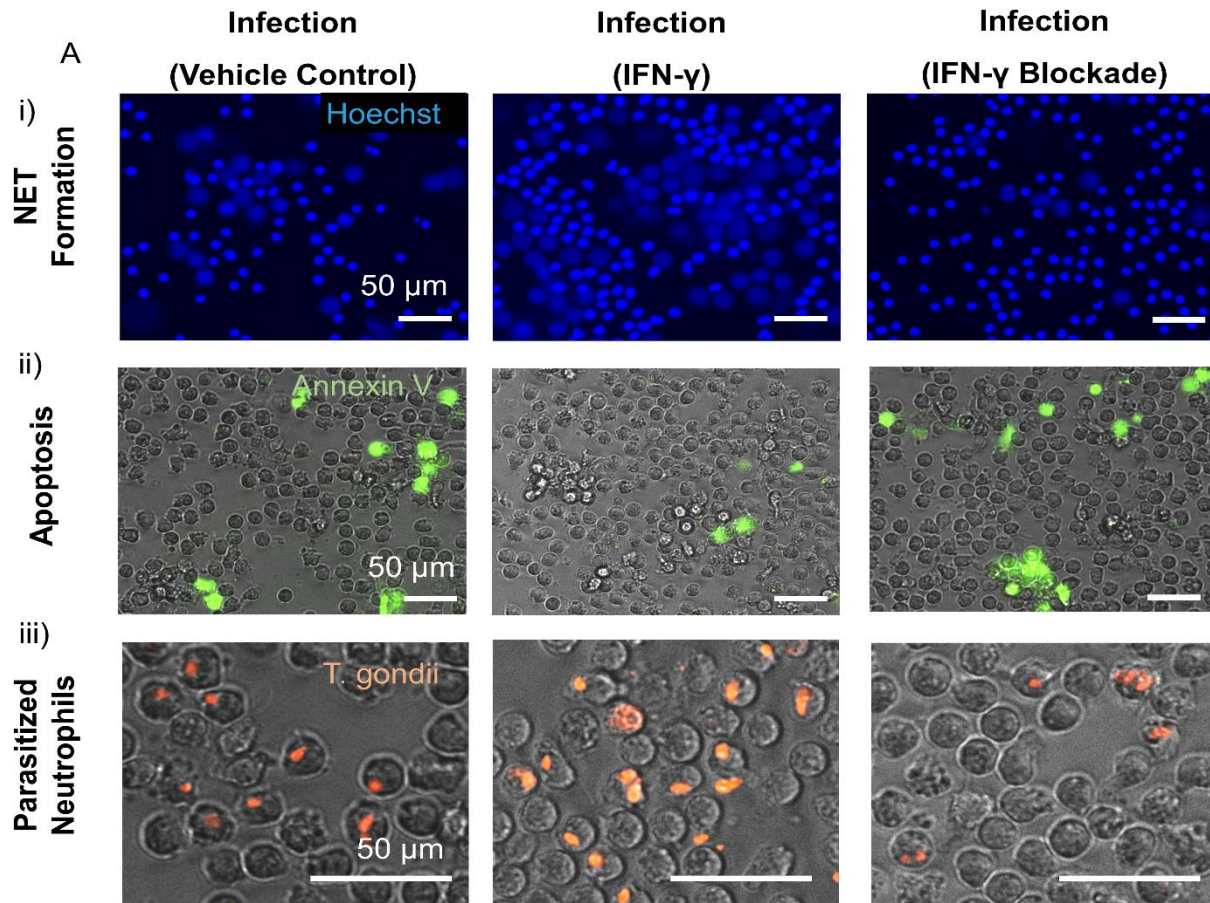


Figure B.4 Influence of IFN- γ stimulation and inhibition on neutrophil function at the site of *T. gondii* infected epithelium. (A) Representative fluorescence images showing NET formation, apoptosis and parasitization of neutrophils from interacting with *T.gondii*-infected epithelium in response to IFN- γ stimulation and inhibition. Caco-2 epithelial tubes were infected with m-cherry tagged ME49 *T. gondii* for 72h before introducing neutrophils into the lumen of the tube. Neutrophils were co-cultured with the infected epithelium for 6 h prior to collection in well-plate and imaging. Fluorescences image showing neutrophils stained with Hoechst 33342 for DNA, decondensed nuclei indicating NET formation (i). Combined brightfield and fluorescence image showing neutrophils stained with Apopxin Green (abcam) as indicator of cells undergoing apoptosis, (ii). Combined brightfield and fluorescence image showing parasitized neutrophils where direct interaction with *T. gondii* parasite is observed (iii).

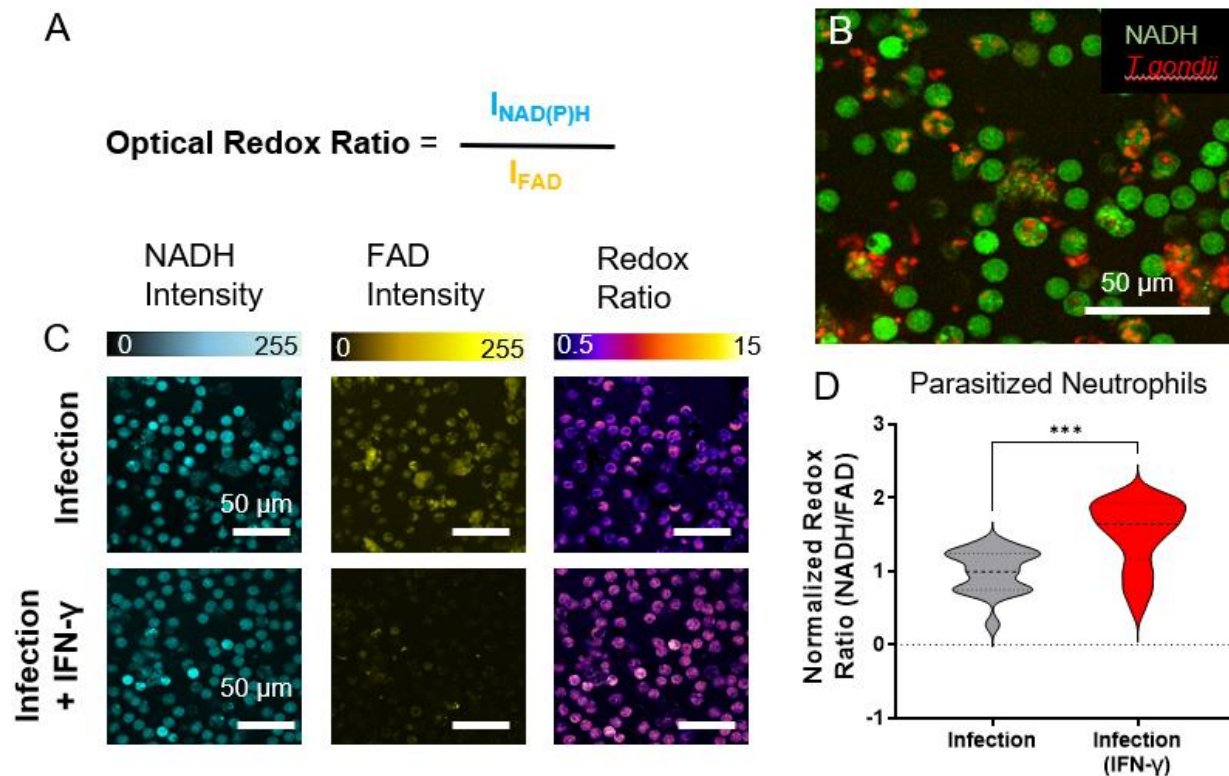
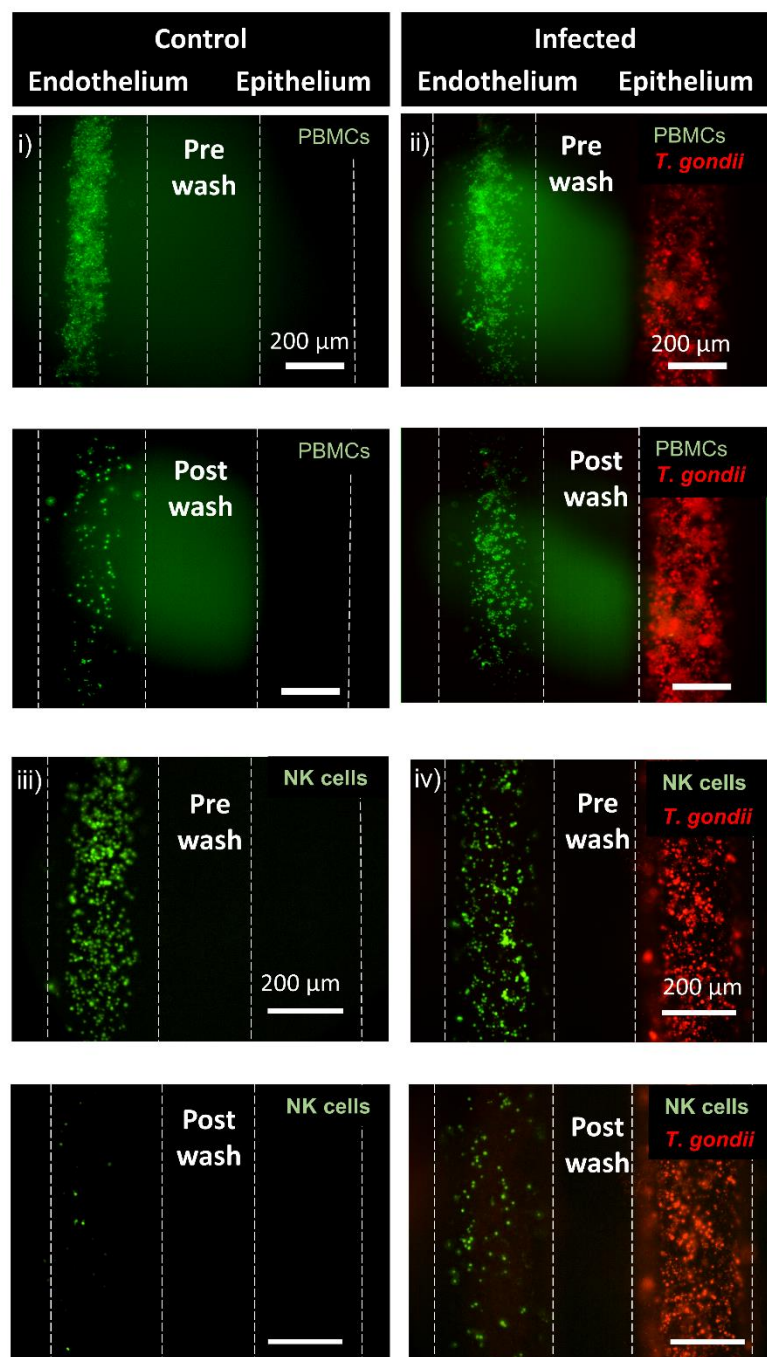


Figure B.5 Optical redox ratio assessment in IFN- γ primed neutrophils during *T. gondii* infection. (A) The optical redox ratio, defined as the autofluorescence intensity of NAD(P)H divided by that of FAD, quantifies the oxidation-reduction state of the cell. Optical metabolic imaging was used to visualize intracellular NAD(P)H and FAD fluorescence intensities of neutrophils in infected systems where the neutrophils were directly introduced into the epithelium to increased instances of direct-contact interaction with *T. gondii* in the lumen of the infected epithelium. (B) Representative images showing autofluorescence intensity of NAD(P)H (green) in neutrophils from in a *T.gondii* (red) -infected epithelium in the intestinal tissue MPS. A number of parasitized neutrophils can be observed. (C) Representative images showing NAD(P)H intensity, FAD intensity and the redox ratio in neutrophils from intestinal tissue MPSs without and with IFN- γ stimulation. (D) Violin plots showing the analysis of neutrophil redox ratio in parasitized cells based on NAD(P)H and FAD intensity (asterisk denotes P value of ≤ 0.05 , n=66-78).

A



B

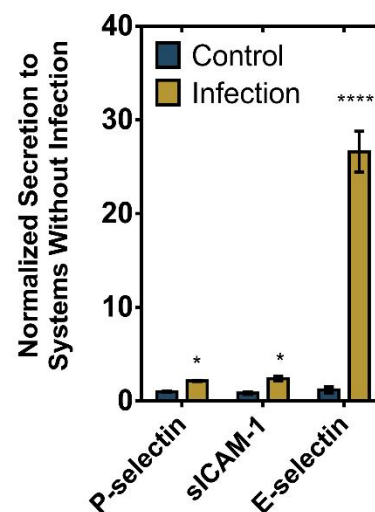


Figure B.6 Effects of epithelial infection by *T. gondii* on immune cell adhesion to endothelium. (A) PBMCs were added to the endothelium 48 hpi with ME49 *T. gondii* and washed away after 2h to evaluate endothelial adhesion of immune cells. Fluorescence image showing differences in primary PBMC adhesion events (pre wash and post wash) to the endothelial vessel in response to control (i) and *T.gondii*-infected (ii), Caco-2 epithelium. Similarly, NK cell adhesion was also examined. Fluorescence image showing differences in NK 92 cell adhesion events (pre wash and post wash) to the endothelial vessel in response to control (iii) and *T.gondii*-infected (iv), Caco-2 epithelium. (B) Increased levels of soluble

adhesion molecules, sP-selectin, sICAM-1, and sE-selectin were also found in the culture media of infected systems. Cytokine concentrations measured in media collected from the intestinal tissue MPS consisting of endothelial vessel and primary intestinal epithelial tubes infected with *T. gondii* normalized to control, uninfected systems. In all cytokine measurement experiments nine devices were prepared on two different days for each paired conditions (infected vs. control, and infection in the absence vs. presence of NK cells), media from three devices were pooled to make one replicate. Significance is expressed as **** $p \leq 0.0001$ and * $p \leq 0.05$).

Table B.1 Top 10 most relevant GO terms (Biological Processes) associated with genes analyzed in neutrophils with their corresponding FDR-adjusted P value

Biological Processes^a	FDR-adjusted P
Cytokine Production	9.84E-23
Positive Regulation Of Cytokine Production	6.21E-22
Regulation Of Leukocyte Mediated Immunity	4.13E-21
Leukocyte Differentiation	4.17E-21
Positive Regulation Of Immune Effector Process	4.40E-21
Response To Cytokine	6.05E-21
Defense Response	1.01E-20
Immune Effector Process	1.84E-20
Adaptive Immune Response	8.99E-20
Regulation Of Immune Effector Process	8.99E-20

^a Based on the GSEA molecular signatures database

Table B.2 Primary and secondary antibodies used for immunofluorescent staining

Primary antibody	Company code	Dilution	Secondary antibody	Dilution
CD31	Abcam AB28364	1:20	^a Alexa Fluor 488 anti-rabbit (Thermo Fisher Scientific, A-11008)	1:100
MUC2	Santa Cruz Biotechnology, sc-515032	1:50	^a Alexa Fluor 488 anti-mouse (Thermo Fisher Scientific, A-11001)	1:100
Villin	Novus Biologicals, NBP2-53201	1:100	^a Alexa Fluor 647 anti-mouse (Thermo Fisher Scientific, A-21235)	1:100
ZO-1	Thermo Fisher Scientific, 61-7300	1:25	^a Alexa Fluor 568 anti-rabbit (Thermo Fisher Scientific, A-11011)	1:100
E-cadherin	BD Biosciences, 610182	1:25	^a Alexa Fluor 488 anti-mouse (Thermo Fisher Scientific, A-11001)	1:100
FABP1	Sigma Aldrich, HPA028275	1:25	^a Alexa Fluor 568 anti-rabbit (Thermo Fisher Scientific, A-11011)	1:100

^a Goat source

Table B.3 Primer set sources for gene expression analysis of primary intestinal epithelium culture in intestinal tissue MPS and in transwells

Gene		Source
Genes associated with proliferation and differentiation, or functional intestinal epithelial cells.	MKI67	Thermo Fisher Scientific, Hs04260396_g1
	Axis inhibition protein 2 (Axin2)	Thermo Fisher Scientific, Hs00610344_m1
	Trefoil factor 1 (TFF1)	Thermo Fisher Scientific, Hs00907239_m1
	Sucrase-isomaltase (SI)	Thermo Fisher Scientific, Hs00356112_m1
	Villin	Thermo Fisher Scientific, Hs01031739_m1
	Mucin 2 (MUC2)	Thermo Fisher Scientific, Hs03005103_g1
	Hypoxia-inducible factor (HIF-1 α)	Thermo Fisher Scientific, Hs00153153_m1
	Leucine-rich-repeat-containing G-protein-coupled receptor 5 (LGR5)	Thermo Fisher Scientific, Hs00969422_m1
	Matrix Metalloproteinase-7 (MMP7)	Thermo Fisher Scientific, Hs01042796_m1
	Lysozyme (LYZ)	Thermo Fisher Scientific, Hs00426232_m1
	Tight junction protein-1 (TJP1)	Thermo Fisher Scientific, Hs01551861_m1
	β -defensin-1 (DEFB1)	Thermo Fisher Scientific, Hs00174765_m1
	β -defensin-4-alpha (DEFB4)	Thermo Fisher Scientific, Hs00823638_m1
	Bestrophin-4 (BEST4)	Thermo Fisher Scientific, Hs00396114_m1
Housekeeping (Reference genes)	GAPDH	Thermo Fisher Scientific, Hs01922876_m1
	HPRT	Thermo Fisher Scientific, Hs02800695_m1
	RPLP0	Thermo Fisher Scientific, Hs99999902_m1

Table B.4 Primer sequences for neutrophil gene expression analysis

Gene	Source	
Genes associated protective immunity.	Interleukin – 10 (IL10)	Integrated DNA Technologies, Hs.PT.58.15400284
	MYD88 innate immune signal transduction adaptor	Integrated DNA Technologies, Hs.PT.58.40601199.gs
	Tumor necrosis factor (TNF)	Integrated DNA Technologies, Hs.PT.58.45380900
	Interleukin – 1beta (IL1B)	Integrated DNA Technologies, Hs.PT.58.1518186
	Interleukin – 6 (IL6)	Integrated DNA Technologies, Hs.PT.58.40226675
	Interleukin – 1alpha (IL1A)	Integrated DNA Technologies, Hs.PT.58.40913627
	Nitric oxide synthase 2 (NOS2)	Integrated DNA Technologies, Hs.PT.58.45668131
	Interleukin – 12A (IL12A)	Integrated DNA Technologies, Hs.PT.58.1687020
	NLR family pyrin domain containing 3 (NLRP3)	Integrated DNA Technologies, Hs.PT.58.39497108
	Interferon gamma (IFNG)	Integrated DNA Technologies, Hs.PT.58.24522521
	Toll-like receptor-2 (TLR2)	Integrated DNA Technologies, Hs.PT.58.26767404
	Toll-like receptor-4 (TLR4)	Integrated DNA Technologies, Hs.PT.58.38700156.g
	Transforming growth factor beta 1 (TGFB1)	Integrated DNA Technologies, Hs.PT.58.39813975
Interleukin – 4 receptor (IL4R)	Integrated DNA Technologies, Hs.PT.58.23069040	

<i>T.gondii</i> genes	Interleukin – 2 (IL2)	Integrated DNA Technologies, Hs.PT.58.1142676
	Interferon alpha 1 (IFNA1)	Integrated DNA Technologies, Hs.PT.58.46311748.g
	Interferon beta 1 (IFNB1)	Integrated DNA Technologies, Hs.PT.58.39481063.g
	Housekeeping gene: alpha-tubulin (TUB1A)	Integrated DNA Technologies, Forward: 5' – GACGACGCCTTCAACACCTTCTTT– 3' Reverse: 5' – AGTTGTTTCGCAGCATCCTCTTTCC– 3'
	SAG1	Integrated DNA Technologies, Forward: 5' – TGCCAGCGGGTACTACAAG– 3' Reverse: 5' – TGCCGTGTCGAGACTAGCAG– 3'
Housekeeping for mammalian cells (Reference genes)	GAPDH	Integrated DNA Technologies, Hs.PT.39a.22214836
	HPRT	Integrated DNA Technologies, Hs.PT.39a.22214821
	RPLP0	Integrated DNA Technologies, Hs.PT.39a.22214824

Bibliography

1. Waring, M. J. *et al.* An analysis of the attrition of drug candidates from four major pharmaceutical companies. *Nat. Rev. Drug Discov.* **14**, 475–486 (2015).
2. Boedicker, J. Q., Vincent, M. E. & Ismagilov, R. F. Microfluidic Confinement of Single Cells of Bacteria in Small Volumes Initiates High-Density Behavior of Quorum Sensing and Growth and Reveals Its Variability. *Angewandte Chemie* vol. 121 6022–6025 (2009).
3. Low, L. A., Mummery, C., Berridge, B. R., Austin, C. P. & Tagle, D. A. Organs-on-chips: into the next decade. *Nat. Rev. Drug Discov.* **20**, 345–361 (2020).
4. Buonomo, O. C. *et al.* New insights into the metastatic behavior after breast cancer surgery, according to well-established clinicopathological variables and molecular subtypes. *PLoS One* **12**, e0184680 (2017).
5. Shen, F. *Targeting CX3CR1 with Novel Antagonists for Breast Cancer Metastasis.* (2016).
6. Langley, R. R. & Fidler, I. J. The seed and soil hypothesis revisited--the role of tumor-stroma interactions in metastasis to different organs. *Int. J. Cancer* **128**, 2527–2535 (2011).
7. Fidler, I. J., Kim, S.-J. & Langley, R. R. The role of the organ microenvironment in the biology and therapy of cancer metastasis. *Journal of Cellular Biochemistry* vol. 101 927–936 (2007).
8. Strilic, B. & Offermanns, S. Intravascular Survival and Extravasation of Tumor Cells. *Cancer Cell* **32**, 282–293 (2017).
9. Lu, W., Bucana, C. D. & Schroit, A. J. Pathogenesis and vascular integrity of breast cancer brain metastasis. *Int. J. Cancer* **120**, 1023–1026 (2007).
10. Reymond, N., d'Água, B. B. & Ridley, A. J. Crossing the endothelial barrier during metastasis. *Nat. Rev. Cancer* **13**, (2013).
11. Gómez-Cuadrado, L., Tracey, N., Ma, R., Qian, B. & Brunton, V. G. Mouse models of metastasis: progress and prospects. *Dis. Model. Mech.* **10**, 1061–1074 (2017).
12. Jin, X. & Mu, P. Targeting Breast Cancer Metastasis. *Breast Cancer: Basic and Clinical Research* vol. 9s1 BCBCR.S25460 (2015).
13. Polyak, K. Breast cancer: origins and evolution. *Journal of Clinical Investigation* vol. 117 3155–3163 (2007).
14. Mokhtari, R. B. *et al.* Combination therapy in combating cancer. *Oncotarget* vol. 8 38022–38043 (2017).
15. Ma, Y.-H. V., Middleton, K., You, L. & Sun, Y. A review of microfluidic approaches for investigating cancer extravasation during metastasis. *Microsystems & Nanoengineering* vol. 4 (2018).
16. Bersini, S., Jeon, J. S., Moretti, M. & Kamm, R. D. In vitro models of the metastatic cascade: from local invasion to extravasation. *Drug Discov. Today* **19**, 735–742 (2014).
17. Shin, M. K., Kim, S. K. & Jung, H. Integration of intra- and extravasation in one cell-based microfluidic chip for the study of cancer metastasis. *Lab on a Chip* vol. 11 3880 (2011).
18. Zhang, Q., Liu, T. & Qin, J. A microfluidic-based device for study of transendothelial invasion of tumor aggregates in realtime. *Lab on a Chip* vol. 12 2837 (2012).
19. Chen, M. B. *et al.* On-chip human microvasculature assay for visualization and quantification of tumor cell extravasation dynamics. *Nat. Protoc.* **12**, 865–880 (2017).
20. Martorelli Di Genova, B., Wilson, S. K., Dubey, J. P. & Knoll, L. J. Intestinal delta-6-desaturase activity determines host range for *Toxoplasma* sexual reproduction. *PLoS Biol.* **17**, e3000364 (2019).
21. Mestas, J. & Hughes, C. C. W. Of mice and not men: differences between mouse and human immunology. *J. Immunol.* **172**, 2731–2738 (2004).
22. Liu, L. *et al.* Global, regional, and national causes of child mortality: an updated systematic analysis for 2010 with time trends since 2000. *Lancet* **379**, 2151–2161 (2012).

23. Toxoplasmosis. *Lancet* **363**, 1965–1976 (2004).
24. Dubey, J. P., Miller, N. L. & Frenkel, J. K. THE TOXOPLASMA GONDII OOCYST FROM CAT FECES. *Journal of Experimental Medicine* vol. 132 636–662 (1970).
25. Genova, B. M. D., Di Genova, B. M. & Knoll, L. J. Comparisons of the Sexual Cycles for the Coccidian Parasites Eimeria and Toxoplasma. *Frontiers in Cellular and Infection Microbiology* vol. 10 (2020).
26. Gentile, M. E. & King, I. L. Blood and guts: The intestinal vasculature during health and helminth infection. *PLoS Pathog.* **14**, e1007045 (2018).
27. Mills, M. & Estes, M. K. Physiologically relevant human tissue models for infectious diseases. *Drug Discov. Today* **21**, 1540–1552 (2016).
28. Saxena, K. *et al.* Human Intestinal Enteroids: a New Model To Study Human Rotavirus Infection, Host Restriction, and Pathophysiology. *J. Virol.* **90**, 43–56 (2016).
29. Barrila, J. *et al.* Modeling Host-Pathogen Interactions in the Context of the Microenvironment: Three-Dimensional Cell Culture Comes of Age. *Infection and Immunity* vol. 86 (2018).
30. Danielson, J. J., Perez, N., Romano, J. D. & Coppens, I. Modelling Toxoplasma gondii infection in a 3D cell culture system In Vitro: Comparison with infection in 2D cell monolayers. *PLOS ONE* vol. 13 e0208558 (2018).
31. Bielecka, M. K. *et al.* A Bioengineered Three-Dimensional Cell Culture Platform Integrated with Microfluidics To Address Antimicrobial Resistance in Tuberculosis. *MBio* **8**, (2017).
32. Persat, A. Bacterial mechanotransduction. *Current Opinion in Microbiology* vol. 36 1–6 (2017).
33. Gruenheid, S. & Brett Finlay, B. Microbial pathogenesis and cytoskeletal function. *Nature* vol. 422 775–781 (2003).
34. Dingemans, J. *et al.* Effect of Shear Stress on Pseudomonas aeruginosa Isolated from the Cystic Fibrosis Lung. *MBio* **7**, (2016).
35. Harker, K. S., Jivan, E., McWhorter, F. Y., Liu, W. F. & Lodoen, M. B. Shear forces enhance Toxoplasma gondii tachyzoite motility on vascular endothelium. *MBio* **5**, e01111–13 (2014).
36. Tatara, A., Albert, N. & Kontoyiannis, D. P. Fungal Mechanobiology: High Shear Forces Increase Rhizopus Virulence. *Open Forum Infectious Diseases* vol. 4 S116–S116 (2017).
37. Rodesney, C. A. *et al.* Mechanosensing of shear by Pseudomonas aeruginosa leads to increased levels of the cyclic-di-GMP signal initiating biofilm development. *Proceedings of the National Academy of Sciences* vol. 114 5906–5911 (2017).
38. Rosenzweig, J. A. *et al.* Spaceflight and modeled microgravity effects on microbial growth and virulence. *Appl. Microbiol. Biotechnol.* **85**, 885–891 (2010).
39. Thomas, W. E., Trintchina, E., Forero, M., Vogel, V. & Sokurenko, E. V. Bacterial adhesion to target cells enhanced by shear force. *Cell* **109**, 913–923 (2002).
40. de Castro, P. A. *et al.* Aspergillus fumigatus calcium-responsive transcription factors regulate cell wall architecture promoting stress tolerance, virulence and caspofungin resistance. *PLoS Genet.* **15**, e1008551 (2019).
41. Rios, A. C. & Clevers, H. Imaging organoids: a bright future ahead. *Nat. Methods* **15**, 24–26 (2018).
42. Barkal, L. J. *et al.* Microbial volatile communication in human organotypic lung models. *Nat. Commun.* **8**, 1770 (2017).
43. Deinhardt-Emmer, S. *et al.* Co-infection with Staphylococcus aureus after primary influenza virus infection leads to damage of the endothelium in a human alveolus-on-a-chip model. *Biofabrication* vol. 12 025012 (2020).
44. Bramley, J. C. *et al.* A Three-Dimensional Cell Culture System To Model RNA Virus Infections at the Blood-Brain Barrier. *mSphere* **2**, (2017).
45. Shah, P. *et al.* A microfluidics-based in vitro model of the gastrointestinal human–microbe

- interface. *Nature Communications* vol. 7 (2016).
46. Blutt, S. E., Crawford, S. E., Ramani, S., Zou, W. Y. & Estes, M. K. Engineered Human Gastrointestinal Cultures to Study the Microbiome and Infectious Diseases. *Cellular and Molecular Gastroenterology and Hepatology* vol. 5 241–251 (2018).
 47. Gural, N., Mancio-Silva, L., He, J. & Bhatia, S. N. Engineered Livers for Infectious Diseases. *Cell Mol Gastroenterol Hepatol* **5**, 131–144 (2018).
 48. Kasendra, M. *et al.* Development of a primary human Small Intestine-on-a-Chip using biopsy-derived organoids. *Sci. Rep.* **8**, 2871 (2018).
 49. Jalili-Firoozinezhad, S. *et al.* A complex human gut microbiome cultured in an anaerobic intestine-on-a-chip. *Nat Biomed Eng* **3**, 520–531 (2019).
 50. Huh, D. *et al.* Reconstituting organ-level lung functions on a chip. *Science* **328**, 1662–1668 (2010).
 51. Benam, K. H. *et al.* Small airway-on-a-chip enables analysis of human lung inflammation and drug responses in vitro. *Nat. Methods* **13**, 151–157 (2016).
 52. White, R. E. High-Throughput Screening in Drug Metabolism and Pharmacokinetic Support of Drug Discovery. *Annual Review of Pharmacology and Toxicology* vol. 40 133–157 (2000).
 53. Lee, M.-Y., Park, C. B., Dordick, J. S. & Clark, D. S. Metabolizing enzyme toxicology assay chip (MetaChip) for high-throughput microscale toxicity analyses. *Proc. Natl. Acad. Sci. U. S. A.* **102**, 983–987 (2005).
 54. Brouzes, E. *et al.* Droplet microfluidic technology for single-cell high-throughput screening. *Proceedings of the National Academy of Sciences* vol. 106 14195–14200 (2009).
 55. Rohde, C. B., Zeng, F., Gonzalez-Rubio, R., Angel, M. & Yanik, M. F. Microfluidic system for on-chip high-throughput whole-animal sorting and screening at subcellular resolution. *Proc. Natl. Acad. Sci. U. S. A.* **104**, 13891–13895 (2007).
 56. Mohr, J. C., de Pablo, J. J. & Palecek, S. P. 3-D microwell culture of human embryonic stem cells. *Biomaterials* **27**, 6032–6042 (2006).
 57. El-Ali, J., Sorger, P. K. & Jensen, K. F. Cells on chips. *Nature* vol. 442 403–411 (2006).
 58. Dittrich, P. S. & Manz, A. Lab-on-a-chip: microfluidics in drug discovery. *Nat. Rev. Drug Discov.* **5**, 210–218 (2006).
 59. Kovarik, M. L. *et al.* Micro total analysis systems for cell biology and biochemical assays. *Anal. Chem.* **84**, 516–540 (2012).
 60. Roth, A. & MPS-WS Berlin 2019. Human microphysiological systems for drug development. *Science* **373**, 1304–1306 (2021).
 61. Shuler, M. L. Organ-, body- and disease-on-a-chip systems. *Lab on a Chip* vol. 17 2345–2346 (2017).
 62. Kim, J. *et al.* Three-Dimensional Human Liver-Chip Emulating Premetastatic Niche Formation by Breast Cancer-Derived Extracellular Vesicles. *ACS Nano* **14**, 14971–14988 (2020).
 63. Lee, J., Kim, S.-E., Moon, D. & Doh, J. A multilayered blood vessel/tumor tissue chip to investigate T cell infiltration into solid tumor tissues. *Lab on a Chip* vol. 21 2142–2152 (2021).
 64. Maurer, M. *et al.* A three-dimensional immunocompetent intestine-on-chip model as in vitro platform for functional and microbial interaction studies. *Biomaterials* **220**, 119396 (2019).
 65. Bischel, L. L., Lee, S.-H. & Beebe, D. J. A practical method for patterning lumens through ECM hydrogels via viscous finger patterning. *J. Lab. Autom.* **17**, 96–103 (2012).
 66. Jiménez-Torres, J. A., Peery, S. L., Sung, K. E. & Beebe, D. J. LumeNEXT: A practical method to pattern luminal structures in ECM gels. *Adv. Healthc. Mater.* **5**, 198–204 (2016).
 67. Bischel, L. L. *et al.* The importance of being a lumen. *The FASEB Journal* vol. 28 4583–4590 (2014).
 68. Berthier, E., Young, E. W. K. & Beebe, D. Engineers are from PDMS-land, Biologists are

- from Polystyrenia. *Lab Chip* **12**, 1224–1237 (2012).
69. Wan, A. M. D., Moore, T. A. & Young, E. W. K. Solvent Bonding for Fabrication of PMMA and COP Microfluidic Devices. *J. Vis. Exp.* (2017) doi:10.3791/55175.
 70. Xia, Y. & Whitesides, G. M. SOFT LITHOGRAPHY. *Annual Review of Materials Science* vol. 28 153–184 (1998).
 71. Jeon, N. L. *et al.* Generation of Solution and Surface Gradients Using Microfluidic Systems. *Langmuir* vol. 16 8311–8316 (2000).
 72. Cheng, S.-Y. *et al.* A hydrogel-based microfluidic device for the studies of directed cell migration. *Lab Chip* **7**, 763–769 (2007).
 73. Cimetta, E. *et al.* Microfluidic device generating stable concentration gradients for long term cell culture: application to Wnt3a regulation of β -catenin signaling. *Lab Chip* **10**, 3277–3283 (2010).
 74. Morel, M., Galas, J.-C., Dahan, M. & Studer, V. Concentration landscape generators for shear free dynamic chemical stimulation. *Lab Chip* **12**, 1340–1346 (2012).
 75. Abhyankar, V. V., Lokuta, M. A., Huttenlocher, A. & Beebe, D. J. Characterization of a membrane-based gradient generator for use in cell-signaling studies. *Lab Chip* **6**, 389–393 (2006).
 76. Moraes, C., Mehta, G., Leshner-Perez, S. C. & Takayama, S. Organs-on-a-Chip: A Focus on Compartmentalized Microdevices. *Annals of Biomedical Engineering* vol. 40 1211–1227 (2012).
 77. Mukhopadhyay, R. When PDMS isn't the best. *Analytical Chemistry* vol. 79 3248–3253 (2007).
 78. van Meer, B. J. *et al.* Small molecule absorption by PDMS in the context of drug response bioassays. *Biochemical and Biophysical Research Communications* vol. 482 323–328 (2017).
 79. Vulto, P. *et al.* Phaseguides: a paradigm shift in microfluidic priming and emptying. *Lab on a Chip* vol. 11 1596 (2011).
 80. Humayun, M. *et al.* Elucidating cancer-vascular paracrine signaling using a human organotypic breast cancer cell extravasation model. *Biomaterials* **270**, 120640 (2021).
 81. CDCBreastCancer. Breast Cancer Statistics. <https://www.cdc.gov/cancer/breast/statistics/index.htm> (2021).
 82. Belkacemi, Y., Hanna, N. E., Besnard, C., Majdoul, S. & Gligorov, J. Local and Regional Breast Cancer Recurrences: Salvage Therapy Options in the New Era of Molecular Subtypes. *Front. Oncol.* **8**, 112 (2018).
 83. Strell, C. & Entschladen, F. Extravasation of leukocytes in comparison to tumor cells. *Cell Commun. Signal.* **6**, 10 (2008).
 84. Katt, M. E., Wong, A. D. & Searson, P. C. Dissemination from a Solid Tumor: Examining the Multiple Parallel Pathways. *Trends Cancer Res.* **4**, 20–37 (2018).
 85. Strilic, B. & Offermanns, S. Intravascular Survival and Extravasation of Tumor Cells. *Cancer Cell* vol. 32 282–293 (2017).
 86. Virumbrales-Muñoz, M. *et al.* Microfluidic lumen-based systems for advancing tubular organ modeling. *Chem. Soc. Rev.* **49**, 6402–6442 (2020).
 87. Zhang, B., Korolj, A., Lai, B. F. L. & Radisic, M. Advances in organ-on-a-chip engineering. *Nature Reviews Materials* vol. 3 257–278 (2018).
 88. Peela, N. *et al.* Advanced biomaterials and microengineering technologies to recapitulate the stepwise process of cancer metastasis. *Biomaterials* **133**, 176–207 (2017).
 89. Mondadori, C. *et al.* Advanced Microfluidic Models of Cancer and Immune Cell Extravasation: A Systematic Review of the Literature. *Front Bioeng Biotechnol* **8**, 907 (2020).
 90. Sontheimer-Phelps, A., Hassell, B. A. & Ingber, D. E. Modelling cancer in microfluidic human organs-on-chips. *Nat. Rev. Cancer* **19**, 65–81 (2019).

91. Lin, Z. *et al.* Recent Advances in Microfluidic Platforms Applied in Cancer Metastasis: Circulating Tumor Cells' (CTCs) Isolation and Tumor-On-A-Chip. *Small* **16**, e1903899 (2020).
92. Coughlin, M. F. & Kamm, R. D. The Use of Microfluidic Platforms to Probe the Mechanism of Cancer Cell Extravasation. *Adv. Healthc. Mater.* **9**, e1901410 (2020).
93. Nagaraju, S., Truong, D., Mouneimne, G. & Nikkhah, M. Microfluidic Tumor-Vascular Model to Study Breast Cancer Cell Invasion and Intravasation. *Adv. Healthc. Mater.* **7**, e1701257 (2018).
94. Jeon, J. S. *et al.* Human 3D vascularized organotypic microfluidic assays to study breast cancer cell extravasation. *Proc. Natl. Acad. Sci. U. S. A.* **112**, 214–219 (2015).
95. Bersini, S. *et al.* A microfluidic 3D in vitro model for specificity of breast cancer metastasis to bone. *Biomaterials* vol. 35 2454–2461 (2014).
96. Mei, X. *et al.* Microfluidic platform for studying osteocyte mechanoregulation of breast cancer bone metastasis. *Integr. Biol.* **11**, 119–129 (2019).
97. Boussommier-Calleja, A. *et al.* The effects of monocytes on tumor cell extravasation in a 3D vascularized microfluidic model. *Biomaterials* vol. 198 180–193 (2019).
98. Chen, M. B. *et al.* Inflamed neutrophils sequestered at entrapped tumor cells via chemotactic confinement promote tumor cell extravasation. *Proc. Natl. Acad. Sci. U. S. A.* **115**, 7022–7027 (2018).
99. Ayuso, J. M., Gong, M. M., Skala, M. C., Harari, P. M. & Beebe, D. J. Human Tumor-Lymphatic Microfluidic Model Reveals Differential Conditioning of Lymphatic Vessels by Breast Cancer Cells. *Adv. Healthc. Mater.* **9**, e1900925 (2020).
100. Lugo-Cintrón, K. M. *et al.* Matrix density drives 3D organotypic lymphatic vessel activation in a microfluidic model of the breast tumor microenvironment. *Lab on a Chip* vol. 20 1586–1600 (2020).
101. Ingram, P. N., Hind, L. E., Jimenez-Torres, J. A., Huttenlocher, A. & Beebe, D. J. An Accessible Organotypic Microvessel Model Using iPSC-Derived Endothelium. *Adv. Healthc. Mater.* **7**, (2018).
102. Rodrigues, S. F. & Granger, D. N. Blood cells and endothelial barrier function. *Tissue Barriers* **3**, e978720 (2015).
103. Sökeland, G. & Schumacher, U. The functional role of integrins during intra- and extravasation within the metastatic cascade. *Mol. Cancer* **18**, 12 (2019).
104. Guo, P. *et al.* ICAM-1 as a molecular target for triple negative breast cancer. *Proc. Natl. Acad. Sci. U. S. A.* **111**, 14710–14715 (2014).
105. LeBleu, V. S., Macdonald, B. & Kalluri, R. Structure and function of basement membranes. *Exp. Biol. Med.* **232**, 1121–1129 (2007).
106. Rowe, R. G. & Weiss, S. J. Breaching the basement membrane: who, when and how? *Trends Cell Biol.* **18**, 560–574 (2008).
107. Spuul, P. *et al.* VEGF-A/Notch-Induced Podosomes Proteolyse Basement Membrane Collagen-IV during Retinal Sprouting Angiogenesis. *Cell Rep.* **17**, 484–500 (2016).
108. Lehmann, B. D. *et al.* Identification of human triple-negative breast cancer subtypes and preclinical models for selection of targeted therapies. *Journal of Clinical Investigation* vol. 121 2750–2767 (2011).
109. Gong, M. M. *et al.* Human organotypic lymphatic vessel model elucidates microenvironment-dependent signaling and barrier function. *Biomaterials* **214**, 119225 (2019).
110. Jin, K., Pandey, N. B. & Popel, A. S. Simultaneous blockade of IL-6 and CCL5 signaling for synergistic inhibition of triple-negative breast cancer growth and metastasis. *Breast Cancer Res.* **20**, 54 (2018).
111. Jayatilaka, H. *et al.* Synergistic IL-6 and IL-8 paracrine signalling pathway infers a strategy to inhibit tumour cell migration. *Nat. Commun.* **8**, 15584 (2017).

112. Jiang, Y. N. *et al.* Interleukin 6 triggered ataxia-telangiectasia mutated activation facilitates lung cancer metastasis via MMP-3/MMP-13 up-regulation. *Oncotarget* **6**, 40719–40733 (2015).
113. Belair, D. G. *et al.* Human vascular tissue models formed from human induced pluripotent stem cell derived endothelial cells. *Stem Cell Rev Rep* **11**, 511–525 (2015).
114. Rosa, S. *et al.* Functional characterization of iPSC-derived arterial- and venous-like endothelial cells. *Sci. Rep.* **9**, 3826 (2019).
115. Gassmann, P., Kang, M.-L., Mees, S. T. & Haier, J. In vivo tumor cell adhesion in the pulmonary microvasculature is exclusively mediated by tumor cell - endothelial cell interaction. *BMC Cancer* vol. 10 (2010).
116. Ueda, T., Shimada, E. & Urakawa, T. Serum levels of cytokines in patients with colorectal cancer: possible involvement of interleukin-6 and interleukin-8 in hematogenous metastasis. *J. Gastroenterol.* **29**, 423–429 (1994).
117. Kozłowski, L., Zakrzewska, I., Tokajuk, P. & Wojtukiewicz, M. Z. Concentration of interleukin-6 (IL-6), interleukin-8 (IL-8) and interleukin-10 (IL-10) in blood serum of breast cancer patients. *Rocz. Akad. Med. Białymst.* **48**, 82–84 (2003).
118. Hotary, K., Li, X.-Y., Allen, E., Stevens, S. L. & Weiss, S. J. A cancer cell metalloprotease triad regulates the basement membrane transmigration program. *Genes Dev.* **20**, 2673–2686 (2006).
119. Bejarano, P. A., Noelken, M. E., Suzuki, K., Hudson, B. G. & Nagase, H. Degradation of basement membranes by human matrix metalloproteinase 3 (stromelysin). *Biochemical Journal* vol. 256 413–419 (1988).
120. Gurkan, O. U. *et al.* Interleukin-6 mediates pulmonary vascular permeability in a two-hit model of ventilator-associated lung injury. *Experimental Lung Research* vol. 37 575–584 (2011).
121. Catar, R. *et al.* IL-6 Trans-Signaling Links Inflammation with Angiogenesis in the Peritoneal Membrane. *J. Am. Soc. Nephrol.* **28**, 1188–1199 (2017).
122. Escribano, J. *et al.* Balance of mechanical forces drives endothelial gap formation and may facilitate cancer and immune-cell extravasation. *PLoS Comput. Biol.* **15**, e1006395 (2019).
123. Kummar, S. *et al.* Utilizing targeted cancer therapeutic agents in combination: novel approaches and urgent requirements. *Nat. Rev. Drug Discov.* **9**, 843–856 (2010).
124. Schott, A. F. *et al.* Phase Ib Pilot Study to Evaluate Reparixin in Combination with Weekly Paclitaxel in Patients with HER-2-Negative Metastatic Breast Cancer. *Clin. Cancer Res.* **23**, 5358–5365 (2017).
125. Trastuzumab, Pertuzumab, Tocilizumab in Treating Participants with Metastatic or Unresectable HER2 Positive Breast Cancer. <https://www.cancer.gov/about-cancer/treatment/clinical-trials/search/v?id=NCI-2017-02497> (2016).
126. Kumar, S., Das, A., Barai, A. & Sen, S. MMP Secretion Rate and Inter-invadopodia Spacing Collectively Govern Cancer Invasiveness. *Biophys. J.* **114**, 650–662 (2018).
127. Patra, G. *et al.* Vaccines against protozoan parasites of veterinary importance: A review. *J Entomol Zool Stud* **5**, 1016–1021 (2017).
128. Bigna, J. J. *et al.* Global, regional, and country seroprevalence of *Toxoplasma gondii* in pregnant women: a systematic review, modelling and meta-analysis. *Sci. Rep.* **10**, 12102 (2020).
129. CDC - Toxoplasmosis. <https://www.cdc.gov/parasites/toxoplasmosis/> (2021).
130. Scalise, A. A., Kakogiannos, N., Zanardi, F., Iannelli, F. & Giannotta, M. The blood–brain and gut–vascular barriers: from the perspective of claudins. *Tissue Barriers* 1926190 (2021).
131. Buzoni-Gatel, D., Schulthess, J., Menard, L. C. & Kasper, L. H. Mucosal defences against orally acquired protozoan parasites, emphasis on *Toxoplasma gondii* infections. *Cell. Microbiol.* **8**, 535–544 (2006).

132. Pifer, R. & Yarovinsky, F. Innate responses to *Toxoplasma gondii* in mice and humans. *Trends Parasitol.* **27**, 388–393 (2011).
133. Ernst, W. Humanized mice in infectious diseases. *Comp. Immunol. Microbiol. Infect. Dis.* **49**, 29–38 (2016).
134. Shultz, L. D., Brehm, M. A., Garcia-Martinez, J. V. & Greiner, D. L. Humanized mice for immune system investigation: progress, promise and challenges. *Nat. Rev. Immunol.* **12**, 786–798 (2012).
135. Maharjan, S., Cecen, B. & Zhang, Y. S. 3D Immunocompetent Organ-on-a-Chip Models. *Small Methods* **4**, (2020).
136. Bein, A. *et al.* Microfluidic Organ-on-a-Chip Models of Human Intestine. *Cell Mol Gastroenterol Hepatol* **5**, 659–668 (2018).
137. Vunjak-Novakovic, G., Ronaldson-Bouchard, K. & Radisic, M. Organs-on-a-chip models for biological research. *Cell* **184**, 4597–4611 (2021).
138. Si, L. *et al.* A human-airway-on-a-chip for the rapid identification of candidate antiviral therapeutics and prophylactics. *Nat Biomed Eng* **5**, 815–829 (2021).
139. Zhang, M. *et al.* Biomimetic Human Disease Model of SARS-CoV-2 Induced Lung Injury and Immune Responses on Organ Chip System. *Adv. Sci.* 2002928 (2020).
140. Kim, J. *et al.* Fungal brain infection modelled in a human-neurovascular-unit-on-a-chip with a functional blood-brain barrier. *Nat Biomed Eng* **5**, 830–846 (2021).
141. Sharma, K. *et al.* Dynamic persistence of UPEC intracellular bacterial communities in a human bladder-chip model of urinary tract infection. *Elife* **10**, (2021).
142. Ortega-Prieto, A. M. *et al.* ‘liver-on-a-chip’ cultures of primary hepatocytes and Kupffer cells for hepatitis B virus infection. *J. Vis. Exp.* (2019) doi:10.3791/58333.
143. Villenave, R. *et al.* Human Gut-On-A-Chip Supports Polarized Infection of Coxsackie B1 Virus In Vitro. *PLoS One* **12**, e0169412 (2017).
144. Guo, Y. *et al.* SARS-CoV-2 induced intestinal responses with a biomimetic human gut-on-chip. *Sci Bull (Beijing)* **66**, 783–793 (2021).
145. Chen, Y., Zhou, W., Roh, T., Estes, M. K. & Kaplan, D. L. In vitro enteroid-derived three-dimensional tissue model of human small intestinal epithelium with innate immune responses. *PLoS One* **12**, e0187880 (2017).
146. Ambrosini, Y. M., Shin, W., Min, S. & Kim, H. J. Microphysiological Engineering of Immune Responses in Intestinal Inflammation. *Immune Netw.* **20**, e13 (2020).
147. Nikolaev, M. *et al.* Homeostatic mini-intestines through scaffold-guided organoid morphogenesis. *Nature* **585**, 574–578 (2020).
148. Brassard, J. A., Nikolaev, M., Hübscher, T., Hofer, M. & Lutolf, M. P. Recapitulating macro-scale tissue self-organization through organoid bioprinting. *Nat. Mater.* **20**, 22–29 (2021).
149. Ivanova, D. L., Mundhenke, T. M. & Gigley, J. P. The IL-12- and IL-23-Dependent NK Cell Response Is Essential for Protective Immunity against Secondary *Toxoplasma gondii* Infection. *J. Immunol.* **203**, 2944–2958 (2019).
150. Sturge, C. R. *et al.* TLR-independent neutrophil-derived IFN- γ is important for host resistance to intracellular pathogens. *Proc. Natl. Acad. Sci. U. S. A.* **110**, 10711–10716 (2013).
151. Gregg, B. *et al.* Replication and distribution of *Toxoplasma gondii* in the small intestine after oral infection with tissue cysts. *Infect. Immun.* **81**, 1635–1643 (2013).
152. Clevers, H. The intestinal crypt, a prototype stem cell compartment. *Cell* **154**, 274–284 (2013).
153. Barragan, A., Brossier, F. & David Sibley, L. Transepithelial migration of *Toxoplasma gondii* involves an interaction of intercellular adhesion molecule 1 (ICAM-1) with the parasite adhesin MIC2. *Cellular Microbiology* vol. 7 561–568 (2005).
154. Jones, E. J., Korcsmaros, T. & Carding, S. R. Mechanisms and pathways of *Toxoplasma gondii* transepithelial migration. *Tissue Barriers* **5**, e1273865 (2017).

155. Pittman, K. J. & Knoll, L. J. Long-Term Relationships: the Complicated Interplay between the Host and the Developmental Stages of *Toxoplasma gondii* during Acute and Chronic Infections. *Microbiol. Mol. Biol. Rev.* **79**, 387–401 (2015).
156. Lambert, H., Dellacasa-Lindberg, I. & Barragan, A. Migratory responses of leukocytes infected with *Toxoplasma gondii*. *Microbes Infect.* **13**, 96–102 (2011).
157. Bliss, S. K., Butcher, B. A. & Denkers, E. Y. Rapid recruitment of neutrophils containing prestored IL-12 during microbial infection. *J. Immunol.* **165**, 4515–4521 (2000).
158. Coombes, J. L. *et al.* Motile invaded neutrophils in the small intestine of *Toxoplasma gondii*-infected mice reveal a potential mechanism for parasite spread. *Proc. Natl. Acad. Sci. U. S. A.* **110**, E1913–22 (2013).
159. Sasai, M. & Yamamoto, M. Innate, adaptive, and cell-autonomous immunity against *Toxoplasma gondii* infection. *Exp. Mol. Med.* **51**, 1–10 (2019).
160. Gigley, J. P. The Diverse Role of NK Cells in Immunity to *Toxoplasma gondii* Infection. *PLoS Pathog.* **12**, e1005396 (2016).
161. Trietsch, S. J. *et al.* Membrane-free culture and real-time barrier integrity assessment of perfused intestinal epithelium tubes. *Nat. Commun.* **8**, 262 (2017).
162. Kerr, S. C. *et al.* A bioengineered organotypic prostate model for the study of tumor microenvironment-induced immune cell activation. *Integr. Biol.* **12**, 250–262 (2020).
163. Hind, L. E., Ingram, P. N., Beebe, D. J. & Huttenlocher, A. Interaction with an endothelial lumen increases neutrophil lifetime and motility in response to *P. aeruginosa*. *Blood* **132**, 1818–1828 (2018).
164. Sato, T. *et al.* Long-term expansion of epithelial organoids from human colon, adenoma, adenocarcinoma, and Barrett's epithelium. *Gastroenterology* **141**, 1762–1772 (2011).
165. Fujii, M. *et al.* Human Intestinal Organoids Maintain Self-Renewal Capacity and Cellular Diversity in Niche-Inspired Culture Condition. *Cell Stem Cell* **23**, 787–793.e6 (2018).
166. Spence, J. R. *et al.* Directed differentiation of human pluripotent stem cells into intestinal tissue in vitro. *Nature* **470**, 105–109 (2011).
167. Xing, T. *et al.* Tight Junction Protein Claudin-7 Is Essential for Intestinal Epithelial Stem Cell Self-Renewal and Differentiation. *Cell Mol Gastroenterol Hepatol* **9**, 641–659 (2020).
168. Bondow, B. J., Faber, M. L., Wojta, K. J., Walker, E. M. & Battle, M. A. E-cadherin is required for intestinal morphogenesis in the mouse. *Dev. Biol.* **371**, 1–12 (2012).
169. Antfolk, M. & Jensen, K. B. A bioengineering perspective on modelling the intestinal epithelial physiology in vitro. *Nat. Commun.* **11**, 6244 (2020).
170. Gjorevski, N. *et al.* Designer matrices for intestinal stem cell and organoid culture. *Nature* **539**, 560–564 (2016).
171. Yui, S. *et al.* Functional engraftment of colon epithelium expanded in vitro from a single adult Lgr5 stem cell. *Nature Medicine* vol. 18 618–623 (2012).
172. Sato, T. *et al.* Single Lgr5 stem cells build crypt-villus structures in vitro without a mesenchymal niche. *Nature* **459**, 262–265 (2009).
173. Wang, Y. *et al.* Bioengineered Systems and Designer Matrices That Recapitulate the Intestinal Stem Cell Niche. *Cell Mol Gastroenterol Hepatol* **5**, 440–453.e1 (2018).
174. Luu, L. *et al.* Proteomic Profiling of Enteroid Cultures Skewed toward Development of Specific Epithelial Lineages. *Proteomics* **18**, e1800132 (2018).
175. Knoll, L. J., Tomita, T. & Weiss, L. M. Chapter 15 - Bradyzoite Development. in *Toxoplasma Gondii (Second Edition)* (eds. Weiss, L. M. & Kim, K.) 521–549 (Academic Press, 2014).
176. Kinnebrew, M. A. & Pamer, E. G. Innate immune signaling in defense against intestinal microbes. *Immunol. Rev.* **245**, 113–131 (2012).
177. Suzuki, Y., Orellana, M. A., Schreiber, R. D. & Remington, J. S. Interferon-gamma: the major mediator of resistance against *Toxoplasma gondii*. *Science* **240**, 516–518 (1988).
178. Suzuki, Y., Conley, F. K. & Remington, J. S. Importance of endogenous IFN-gamma for prevention of toxoplasmic encephalitis in mice. *J. Immunol.* **143**, 2045–2050 (1989).

179. Schariton-Kersten, T. M. *et al.* In the absence of endogenous IFN-gamma, mice develop unimpaired IL-12 responses to *Toxoplasma gondii* while failing to control acute infection. *J. Immunol.* **157**, 4045–4054 (1996).
180. Sturge, C. R. & Yarovinsky, F. Complex immune cell interplay in the gamma interferon response during *Toxoplasma gondii* infection. *Infect. Immun.* **82**, 3090–3097 (2014).
181. Boehm, U., Klamp, T., Groot, M. & Howard, J. C. CELLULAR RESPONSES TO INTERFERON- γ . *Annu. Rev. Immunol.* **15**, 749–795 (1997).
182. Bogdan, C., Röllinghoff, M. & Diefenbach, A. The role of nitric oxide in innate immunity. *Immunol. Rev.* **173**, 17–26 (2000).
183. Wang, F. *et al.* Interferon Gamma Induces Reversible Metabolic Reprogramming of M1 Macrophages to Sustain Cell Viability and Pro-Inflammatory Activity. *EBioMedicine* **30**, 303–316 (2018).
184. Mayer-Scholl, A., Averhoff, P. & Zychlinsky, A. How do neutrophils and pathogens interact? *Curr. Opin. Microbiol.* **7**, 62–66 (2004).
185. Appelberg, R. Neutrophils and intracellular pathogens: beyond phagocytosis and killing. *Trends Microbiol.* **15**, 87–92 (2007).
186. Zhao, W., Fogg, D. K. & Kaplan, M. J. A novel image-based quantitative method for the characterization of NETosis. *J. Immunol. Methods* **423**, 104–110 (2015).
187. Skala, M. C. *et al.* In vivo multiphoton microscopy of NADH and FAD redox states, fluorescence lifetimes, and cellular morphology in precancerous epithelia. *Proc. Natl. Acad. Sci. U. S. A.* **104**, 19494–19499 (2007).
188. Datta, R., Gillette, A., Stefely, M. & Skala, M. C. Recent innovations in fluorescence lifetime imaging microscopy for biology and medicine. *J. Biomed. Opt.* **26**, (2021).
189. Weiss, G. & Schaible, U. E. Macrophage defense mechanisms against intracellular bacteria. *Immunol. Rev.* **264**, 182–203 (2015).
190. Courret, N. *et al.* CD11c- and CD11b-expressing mouse leukocytes transport single *Toxoplasma gondii* tachyzoites to the brain. *Blood* **107**, 309–316 (2006).
191. Lachenmaier, S. M., Deli, M. A., Meissner, M. & Liesenfeld, O. Intracellular transport of *Toxoplasma gondii* through the blood–brain barrier. *J. Neuroimmunol.* **232**, 119–130 (2011).
192. Turvey, S. E. & Broide, D. H. Innate immunity. *J. Allergy Clin. Immunol.* **125**, S24–32 (2010).
193. Casciotti, L., Ely, K. H., Williams, M. E. & Khan, I. A. CD8+ T-Cell Immunity against *Toxoplasma gondii* Can Be Induced but Not Maintained in Mice Lacking Conventional CD4+ T Cells. *Infect. Immun.* **70**, 434 (2002).
194. Fatehullah, A., Tan, S. H. & Barker, N. Organoids as an in vitro model of human development and disease. *Nat. Cell Biol.* **18**, 246–254 (2016).
195. Clevers, H. Modeling Development and Disease with Organoids. *Cell* **165**, 1586–1597 (2016).
196. Rossi, G., Manfrin, A. & Lutolf, M. P. Progress and potential in organoid research. *Nat. Rev. Genet.* **19**, 671–687 (2018).
197. Luu, L. *et al.* An Open-Format Enteroid Culture System for Interrogation of Interactions Between *Toxoplasma gondii* and the Intestinal Epithelium. *Front. Cell. Infect. Microbiol.* **9**, 300 (2019).
198. Jabaji, Z. *et al.* Use of collagen gel as an alternative extracellular matrix for the in vitro and in vivo growth of murine small intestinal epithelium. *Tissue Eng. Part C Methods* **19**, 961–969 (2013).
199. Wang, Y. *et al.* Self-renewing Monolayer of Primary Colonic or Rectal Epithelial Cells. *Cell Mol Gastroenterol Hepatol* **4**, 165–182.e7 (2017).
200. Altay, G. *et al.* Self-organized intestinal epithelial monolayers in crypt and villus-like domains show effective barrier function. *Sci. Rep.* **9**, 1–14 (2019).

201. Barker, N. Adult intestinal stem cells: critical drivers of epithelial homeostasis and regeneration. *Nat. Rev. Mol. Cell Biol.* **15**, 19–33 (2013).
202. Denkers, E. Y., Schneider, A. G., Cohen, S. B. & Butcher, B. A. Phagocyte responses to protozoan infection and how *Toxoplasma gondii* meets the challenge. *PLoS Pathog.* **8**, e1002794 (2012).
203. Hou, B., Benson, A., Kuzmich, L., DeFranco, A. L. & Yarovinsky, F. Critical coordination of innate immune defense against *Toxoplasma gondii* by dendritic cells responding via their Toll-like receptors. *Proc. Natl. Acad. Sci. U. S. A.* **108**, 278–283 (2011).
204. Bliss, S. K., Gavrilescu, L. C., Alcaraz, A. & Denkers, E. Y. Neutrophil depletion during *Toxoplasma gondii* infection leads to impaired immunity and lethal systemic pathology. *Infect. Immun.* **69**, 4898–4905 (2001).
205. Varikuti, S. *et al.* Host-Directed Drug Therapies for Neglected Tropical Diseases Caused by Protozoan Parasites. *Front. Microbiol.* **9**, 2655 (2018).
206. Marshall, J. S., Warrington, R., Watson, W. & Kim, H. L. An introduction to immunology and immunopathology. *Allergy Asthma Clin. Immunol.* **14**, 49 (2018).
207. Lee, A. J. & Ashkar, A. A. The Dual Nature of Type I and Type II Interferons. *Front. Immunol.* **9**, 2061 (2018).
208. Mennechet, F. J. D. *et al.* Lamina propria CD4+ T lymphocytes synergize with murine intestinal epithelial cells to enhance proinflammatory response against an intracellular pathogen. *J. Immunol.* **168**, 2988–2996 (2002).
209. Robben, P. M., LaRegina, M., Kuziel, W. A. & Sibley, L. D. Recruitment of Gr-1+ monocytes is essential for control of acute toxoplasmosis. *J. Exp. Med.* **201**, 1761–1769 (2005).
210. Villeret, B. *et al.* Blockade of IL-1R signaling diminishes Paneth cell depletion and *Toxoplasma gondii* induced ileitis in mice. *Am. J. Clin. Exp. Immunol.* **2**, 107–116 (2013).
211. Melchor, S. J. *et al.* IL-1R Regulates Disease Tolerance and Cachexia in *Toxoplasma gondii* Infection. *J. Immunol.* **204**, 3329–3338 (2020).
212. Channon, J. Y., Miselis, K. A., Minns, L. A., Dutta, C. & Kasper, L. H. *Toxoplasma gondii* induces granulocyte colony-stimulating factor and granulocyte-macrophage colony-stimulating factor secretion by human fibroblasts: implications for neutrophil apoptosis. *Infect. Immun.* **70**, 6048–6057 (2002).
213. Jebbari, H., Roberts, C. W., Ferguson, D. J., Bluethmann, H. & Alexander, J. A protective role for IL-6 during early infection with *Toxoplasma gondii*. *Parasite Immunol.* **20**, 231–239 (1998).
214. Rostami Nejad, M. *et al.* The evaluation of interleukin-8 chemokine in chronic and acute *Toxoplasma gondii* infection. *Gastroenterol Hepatol Bed Bench* **4**, 34–37 (2011).
215. Yap, G. S. & Sher, A. Effector cells of both nonhemopoietic and hemopoietic origin are required for interferon (IFN)- γ -and tumor necrosis factor (TNF)- α -dependent host resistance to the intracellular pathogen, *Toxoplasma gondii*. *J. Exp. Med.* **189**, 1083–1092 (1999).
216. Perona-Wright, G., Mohrs, K., Szaba, F. M., Kummer, L. W. & Madan, R. CL 695 Karp, LL Johnson, ST Smiley, and M. (2009).
217. Kwaa, A. K. R., Talana, C. A. G. & Blankson, J. N. Interferon Alpha Enhances NK Cell Function and the Suppressive Capacity of HIV-Specific CD8+ T Cells. *J. Virol.* **93**, (2019).
218. Kelly, M. N. *et al.* Interleukin-17/Interleukin-17 Receptor-Mediated Signaling Is Important for Generation of an Optimal Polymorphonuclear Response against *Toxoplasma gondii* Infection. *Infection and Immunity* vol. 73 617–621 (2005).
219. Moretta, A., Marcenaro, E., Parolini, S., Ferlazzo, G. & Moretta, L. NK cells at the interface between innate and adaptive immunity. *Cell Death Differ.* **15**, 226–233 (2008).
220. Khan, I. A. *et al.* IP-10 is critical for effector T cell trafficking and host survival in *Toxoplasma gondii* infection. *Immunity* **12**, 483–494 (2000).
221. Spellberg, B. & Edwards, J. E., Jr. Type 1/Type 2 immunity in infectious diseases. *Clin.*

- Infect. Dis.* **32**, 76–102 (2001).
222. Kiniwa, T. *et al.* NK cells activated by Interleukin-4 in cooperation with Interleukin-15 exhibit distinctive characteristics. *Proc. Natl. Acad. Sci. U. S. A.* **113**, 10139–10144 (2016).
223. Ivanova, D. L. *et al.* NK Cells Negatively Regulate CD8 T Cells to Promote Immune Exhaustion and Chronic *Toxoplasma gondii* Infection. *Front. Cell. Infect. Microbiol.* **10**, 313 (2020).
224. Mahe, M. M., Sundaram, N., Watson, C. L., Shroyer, N. F. & Helmrath, M. A. Establishment of human epithelial enteroids and colonoids from whole tissue and biopsy. *J. Vis. Exp.* (2015) doi:10.3791/52483.
225. VanDussen, K. L., Sonnek, N. M. & Stappenbeck, T. S. L-WRN conditioned medium for gastrointestinal epithelial stem cell culture shows replicable batch-to-batch activity levels across multiple research teams. *Stem Cell Res.* **37**, 101430 (2019).
226. VanDussen, K. L. *et al.* Development of an enhanced human gastrointestinal epithelial culture system to facilitate patient-based assays. *Gut* **64**, 911–920 (2015).
227. Khan, A. & Grigg, M. E. *Toxoplasma gondii*: Laboratory Maintenance and Growth. *Curr. Protoc. Microbiol.* **44**, 20C.1.1–20C.1.17 (2017).
228. Mukaida, N., Nosaka, T., Nakamoto, Y. & Baba, T. Lung Macrophages: Multifunctional Regulator Cells for Metastatic Cells. *Int. J. Mol. Sci.* **20**, (2018).
229. Sosa, M. S., Bragado, P. & Aguirre-Ghiso, J. A. Mechanisms of disseminated cancer cell dormancy: an awakening field. *Nat. Rev. Cancer* **14**, 611–622 (2014).
230. Walsh, A. J. *et al.* Optical metabolic imaging identifies glycolytic levels, subtypes, and early-treatment response in breast cancer. *Cancer Res.* **73**, 6164–6174 (2013).
231. Walsh, A. J. *et al.* Quantitative optical imaging of primary tumor organoid metabolism predicts drug response in breast cancer. *Cancer Res.* **74**, 5184–5194 (2014).
232. Li, C. *et al.* Under-Oil Autonomously Regulated Oxygen Microenvironments: A Goldilocks Principle-Based Approach For Microscale Cell Culture. doi:10.1101/2020.12.16.423117.